Validation of novel pointing concepts for LISA

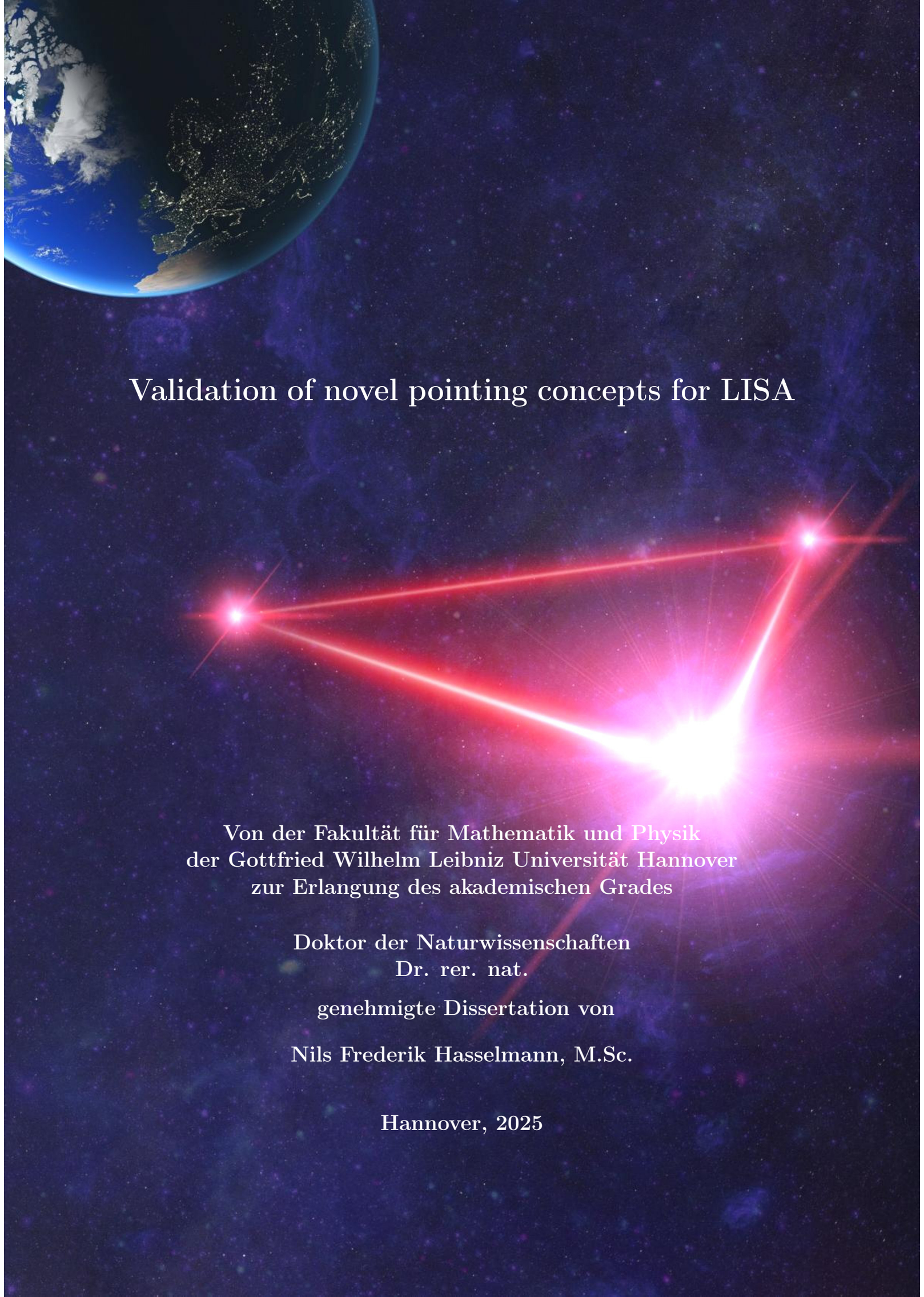

Von der Fakultät für Mathematik und Physik
der Gottfried Wilhelm Leibniz Universität Hannover
zur Erlangung des akademischen Grades

Doktor der Naturwissenschaften
Dr. rer. nat.

genehmigte Dissertation von

Nils Frederik Hasselmann, M.Sc.

Hannover, 2025

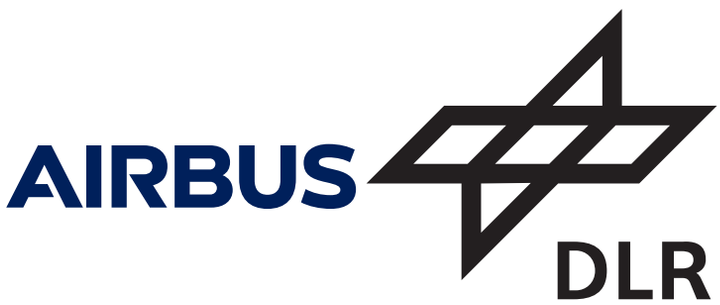

Referent: Prof. Dr. Gerhard Heinzel

Korreferent: Prof. Dr. Claus Braxmaier

Korreferent: Prof. Dr. John Conklin

Tag und Ort der Promotion: 12.02.2025, Hannover

Front cover image: LISA constellation artistic impression

Back cover image: Messier 74 combined VIS (Hubble) and IR image (JWST, MIRI), raw images credit: ESA and MIRI consortium

Erklärung der Selbstständigkeit

Hiermit versichere ich, dass ich die vorliegende genehmigte Dissertation von selbstständig und ohne fremde Hilfe verfasst habe. Die Arbeit hat in gleicher oder ähnlicher Form noch keinem anderen Prüfungsamt vorgelegen.

Hannover, den 28.2.2025

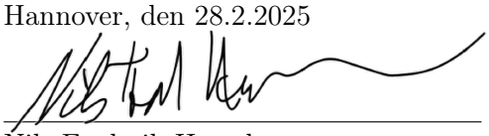

Nils Frederik Hasselmann

Acknowledgements

Supervision First and foremost, I would like to thank Prof. Dr. Gerhard Heinzel (Max Planck Institute for Gravitational Physics (AEI)) for agreeing to be my doctoral supervisor on the side of the Centre for Quantum Engineering and Space-Time Research (QUEST) Leibniz Research School (Leibniz University Hannover). I appreciate your taking the time to visit me in the Laboratory for Enabling Technologies (LET) at Airbus whenever meetings at the Friedrichshafen site brought you all the distance to Lake Constance from Hannover. Sadly, due to COVID-19, business travel was very restricted, so I could barely visit the AEI. Initially, Prof. Dr. Karsten Danzmann was selected as the second examiner, the apparent choice regarding the thesis topic. Sadly, an accident and a change in the studying regulations prevented Prof. Danzman from maintaining the status of an examiner, as only one examiner is allowed to be a member of the AEI. I thank Prof. Dr. Claus Braxmaier (head of DLR QT, Ulm, and professor at the University of ULM), who also supervised another PhD Candidate at the LET, Alexander Schultze, and is familiar with the lab, the LISA mission, the In-Field Pointing setup as well as its objectives and results obtained with it to agreeing to be the second examiner. Furthermore, I thank Prof. Dr. John W. Conklin (Director of the Precision Space Systems Laboratory, Department of Mechanical and Aerospace Engineering, University of Florida) for agreeing to accept the role as third supervisor of this thesis, thus helping me out on short notice, which is much appreciated. Special thanks go to Dr. Alexander Sell for acting as a mentor and supervisor during my time as a PhD student at Airbus Defence and Space GmbH. Alexander was always available for an in-depth discussion and became an invaluable source of information on even the most obscure topics. Furthermore, he knew how to provide funding for entertainment through little on-the-side research projects. Those were a bit time-consuming but presented an excellent way to have a break and regain motivation to work on the main project and insights into various topics outside the main project's direct scope. I also would like to thank Dennis Weise for always encouraging me and spreading motivation by being psyched about the latest results.

Financial support I would like to acknowledge funding by the German BMWK via DLR grant 50OQ1302 and funding by the Advanced Projects Germany department (now ESA Science and Earth Observation: Future Projects and Proposals), part of Airbus Defence and Space GmbH, Germany, in the form of internal R&D funds.

Third party contributions I thank Oliver Mandel for the helpful discussions, which were sometimes lengthy, and for providing code for the simulations regarding the effects of an active aperture clipping the RX beam. A paper on the active aperture concept is being prepared, which Oliver will also contribute to. Philipp E., Moritz, and Bart: Thanks for proofreading manuscripts, discussing many topics outside of work, and setting up telescopes together for star parties that let us relax or have a beer in busy times. I thank Philipp B. for laser cutting the aperture RX clips, which required several iterations of parameter optimization to obtain cuts with smooth edges. Our intern Maxim, thank you for recording the measurements for optimizing the bimorph piezo drive with respect to its linearity. Furthermore, I thank our intern, Jonathan, for integrating the hardware safety feature for the seismic noise compensation scheme on the IFP setup and testing the lifting pads procured long ago as actuators instead of the pneumatic dampeners. Jonathan also measured NTC thermistor noise and programmed some evaluation scripts. The results will be featured in at least one publication (see appendix). Additionally, Jonathan designed the pre-tensioning tool for the launch lock, which Alex and I developed, and is currently performing the pretensioning. Environmental testing and another publication on the concept, the design process of the launch lock and the outcome of these tests will be completed soon. Finally, I would like to thank everyone who contributed in some way but is not mentioned above.

Kurzzusammenfassung

Der Nachweis tieffrequenter Gravitationswellen mittels bodengestützter interferometrischer Detektoren ist aufgrund seismischer Aktivität heute und auch in näherer Zukunft nicht möglich. Gravitationswellenobservatorien im Weltall sind nicht durch diese Rauschquelle limitiert und können eine erheblich größere Basislänge nutzen, dies bringt jedoch eigene Herausforderungen mit sich: Orbitale Dynamiken bewirken Schwankungen der Apexwinkel der Konstellation aus drei Satelliten. Diese sind ausgestattet mit Testmassen, zwischen denen Abstandsvariationen vermessen werden. Damit Messungen der Abstandsvariationen erfolgen können und damit der Nachweis von Gravitationswellen kontinuierlich und rauscharm durchgeführt werden kann, ist eine Nachführung der Feldwinkel erforderlich. Ohne diese degradiert zunächst der Interferometerkontrast (bereits nach grob 1 ks) und schließlich geht das Signal verloren. Im Rahmen dieser Arbeit werden Aspekte zweier fortgeschrittener Feldwinkelnachführungskonzepte, genannt In-Field- und Siderostat-Pointing, experimentell untersucht, um deren Machbarkeit zu zeigen: Diese basieren auf der Nutzung fixer Teleskopeinheiten und der Aktuation von ein bis zwei Spiegeln pro Satellit, wodurch sich zahlreiche Vorteile aber auch einige Nachteile ergeben (z.B. sind eine Reduktion von Eigengravitationseffekten und die Vermeidung eines bewegten Kabelbaumes gegen zusätzliche Projektionseffekte abzuwägen). Damit werden Alternativen zu der Basisarchitektur Telescope Pointing aufgezeigt, welche auf der Nachführung von ein bis zwei Teleskopen inklusive derer Testmassen und optischen Banken basiert. Da hierbei relativ große Massen bewegt werden, ist eine Demonstration der geforderten Winkelrauscharmut bisher nicht erfolgt und wird sich auch zukünftig aufgrund der Erdschwere am Boden als herausfordernd erweisen. Die durchgeführten Untersuchungen, bei denen oft hochpräzise heterodyninterferometrische Messungen von Pfadlängen und Winkeln zum Einsatz kommen, zeigen die prinzipielle Realisierbarkeit der alternativen Nutzlastarchitekturen und erlauben die Demonstration kritischer Funktionen wie z.B. die Feldwinkelnachführung einer Richtstrecke. Zusätzlich werden mehrere Verbesserungsmöglichkeiten in der Opto-Mechanik dieser (und aller) Nutzlastarchitekturen aufgezeigt.

Schlüsselworter: Alternatives Nutzlastkonzept, LISA, Winkel-zu-Pfadlänngenkopplung

Abstract

Detecting low-frequency gravitational waves using ground-based interferometric detectors is impossible today and in the near future due to seismic activity. Space-based gravitational wave detectors are not limited by this noise source and permit much longer arm-lengths. However, going to space also comes with challenges: Orbital dynamics result in fluctuations of the apex angles of the near equilateral formation consisting of three satellites containing test masses, between which the distance fluctuations are measured to detect gravitational waves. A line-of-sight pointing is thus required to continuously detect gravitational waves with minimal excess noise. Without active pointing, the interferometric contrast would degrade (after only roughly 1 ks), and the signal would finally be lost entirely. Within the frame of this work, aspects of two advanced pointing concepts, In-Field and Siderostat Pointing, will be investigated experimentally to show their feasibility. These concepts are based on fixed telescope modules and one to two actuated mirrors per spacecraft, yielding many benefits while presenting some unique challenges (e.g., reduced self-gravity effects and no need for a flexible harness vs. additional projection effects). In doing so, alternatives for the baseline pointing concept dubbed 'Telescope pointing' are pointed out. In Telescope pointing, one to two telescopes, including their gravitational reference sensors and optical benches, are actuated during active pointing per spacecraft. This concept's angular noise performance has yet to be shown, which is an especially challenging feat on-ground under representative conditions due to the large actuated masses and the cable harness connecting moving parts to the satellite. The investigations presented herein typically employ ultra-precise optical metrology, namely heterodyne interferometry, to measure optical pathlengths and angles. This allows probing key performance parameters and testing functionalities (such as coupling of angle to pathlength, angular stability, and compensation of coupling of angular to pathlength noise). The studies find that the alternative payload architectures are, in principle, realizable and demonstrate critical core functions such as active pointing. Additionally, possible improvements in the design of not only those but all pointing schemes are detailed.

Keywords: Alternative payload concept, LISA, tilt-to-pathlength coupling

Contents

1 Introduction **1**
- 1.1 Low-frequency gravitational wave detection 1
- 1.2 Overview of line-of-sight pointing concepts 2
- 1.3 Performance validation of line-of-sight pointing concepts 5

2 Theory **9**
- 2.1 Piston at active mirrors 10
- 2.2 Mitigation of tilt-to-length coupling using pupil imaging 12
- 2.3 Tilt-to-length coupling in a Korsch type off-axis telescope 14
- 2.4 Semi-analytical model of the setup 18
- 2.5 Definitions of the interferometric phase 25

3 Validation of the In-Field pointing concept **29**
- 3.1 Objectives 30
- 3.2 In-Field pointing setup 30
  - 3.2.1 Optical design 34
- 3.3 Completion of the integration and alignment 37
  - 3.3.1 In-Field pointing mechanism 37
  - 3.3.2 Refractive 5x stage 39
  - 3.3.3 Refractive 1x relay stage 41
  - 3.3.4 Quadrant photodetector 42
  - 3.3.5 Spacecraft simulator 43
- 3.4 Compensation of linear tilt-to-length effects by active apertures 44
- 3.5 Key tilt-to-length coupling measurements 47
  - 3.5.1 Far-field tilt-to-length coupling 48
  - 3.5.2 End-to-end system tilt-to-length coupling 50
- 3.6 Environmental noise contributions 53
  - 3.6.1 Thermal noise 53
  - 3.6.2 Seismic noise 56
- 3.7 Optical noise performance 58
  - 3.7.1 Path length noise 59
  - 3.7.2 Angular noise 62
- 3.8 End-to-end demonstration of active pointing 64
- 3.9 Periodic nonlinearities of bimorph actuators 67

3.9.1 Background 67
3.9.2 Principle of the optimization procedure 68
3.9.3 Results 70
3.9.4 Changing the direction of travel 74
3.10 Summary of results 76

4 Design and validation of the Siderostat pointing mechanism 81
4.1 Objectives and the prototype mechanism 82
4.2 Design and dimensioning of the Siderostat-Pointing mechnanism 83
4.2.1 Linear stage 83
4.2.2 Rotational stage 85
4.3 Experimental setups 87
4.3.1 Tribological tests 87
4.3.2 Path length stability measurements 88
4.3.3 Angular noise measurements 89
4.4 Hinge natural frequency and actuation forces 89
4.5 Tribological testing of low friction solid film coatings 89
4.6 Hysteresis and bistable behavior 91
4.7 Creep of the linear stage 94
4.8 Noise performance 94
4.9 Summary of results 96

5 Conclusion and outlook 99
5.1 Lessons learned and way forward 100

A Additional information 103
A.1 Noise sources in heterodyne interferometry 103
A.2 AAM simulation parameters 104

B Publications based on the above 107

C Launch lock development 109

D Optimization of temperature sensors 119

E Active thermal control for LISA 127

CV and list of publications 143

Acronyms

AAM	Active Aperture Mechanism
ADS	Airbus Defence and Space
AIT	Alignment Integration and Testing
AOM	Acoustic Optic Modulator
ASD	Amplitude Spectral Density
BAM	Beam Alignment Mechanism
BE	Beam Expander
CTE	Coefficient of Thermal Expansion
DFACS	Drag-Free Attitude Control System
DLC	Diamond-like Carbon
DWS	Differential Wavefront Sensing
EDM	Electric Discharge Machining
FEM	Finite Element Modeling
FIOS	Fiber Injector Optical Subassembly
FLL	Frequency-Lock-Loop
FOV	Field-of-View
GRS	Gravitational Reference Sensor
HWP	Half-Wave Plate
IFO	Interferometer
IFP	In-Field Pointing
IFPM	In-Field Pointing Mechanism
LIGO	Laser Interferometer Gravitational-Wave Observatory
LISA	Laser Interferometer Space Antenna

LMB	LISA Measurement Band
LO	Local Oscillator
LOS	Line-of-Sight
LPF	LISA Pathfinder
LTP	LISA Technology Package
MLI	Multi-Layer-Insulation
MOSA	Moving Optical Sub-Assembly
NTC	Negative Temperature Coefficient
OAT	Off-Axis Telescope
OB	Optical Bench
OGSE	Optical Ground Support Equipment
OPD	Optical Pathlength Difference
PAAM	Point-Ahead Angle Mechanism
PBS	Polarizing Beam Splitter
PLL	Phase-Locked-Loop
QPD	Quadrant Photodetector
QWP	Quarter-Wave Plate
RIN	Relative Intensity Noise
RX	receive (direction)
S/C	Spacecraft
SCS	Spacecraft Simulator
SHS	Shack-Hartman Sensor
SNR	Signal-to-Noise-Ratio
SP	Siderostat Pointing
SPM	Siderostat Pointing Mechanism
TNO	Netherlands Organization for Applied Scientific Research
TP	Telescope Pointing
TTL	Tilt-to-Length (coupling)
TX	transmission (direction)
WFE	Wavefront Error

Chapter 1

Introduction

1.1 Low-frequency gravitational wave detection

The Laser Interferometer Space Antenna (LISA) sets out to observe gravitational waves in the low-frequency band from 0.1 mHz to 1 Hz (dubbed LISA Measurement Band (LMB)), allowing observation at redshifts up to 20, looking back in time to epochs even before the cosmic re-ionization. This allows the scientific community to investigate eight science objectives of great importance and complements data from ground-based detectors such as the advanced Laser Interferometer Gravitational-Wave Observatory (LIGO). [1] Besides learning about the formation of the first massive black holes and further testing of general relativity in the hope of finding deviations not explained by current theories and thus possibly new physics, measurements of the Hubble parameter can be performed. Those may resolve the disparity in the results obtained by standard candles and cosmic microwave background radiation. While ground-based detectors can be upgraded and maintained at lower costs, the low-frequency band is, so far, inaccessible due to seismic noise and will remain so in the foreseeable future. [2, 3] Seismic activity itself is not easily prevented or avoided. Circumventing seismic activity by operating a gravitational wave observatory in space is a feasible solution. The drastically different environment and location of a space-borne detector require a very different design, posing new challenges, such as radiation hardening, the effect of solar winds, micrometeoroids, etc.. [4, 5]

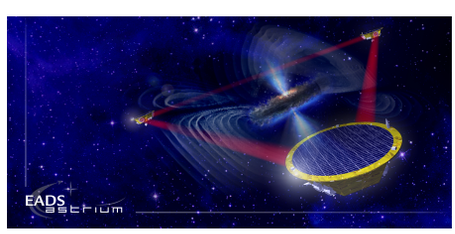

Figure 1.1: Artistic depiction of the LISA constellation and an event to be detected (Courtesy: ADS).

For LISA, a formation of three Spacecraft (S/C) in nearly equilateral configuration (see Fig.1.2) with a separation of 2.5 Gm in earth trailing, helio-centric orbit was proposed: The measurement of distance fluctuations between test masses contained within these S/C allows for space-time strain measurements. Orbital dynamics cause the apex angles of the formation to vary by roughly $\pm 1°$ over the mission duration. An active pointing of the Line-of-Sight (LOS) is thus required to maintain the links between the S/C at the shot-noise level needed for detection. To this end, several different pointing concepts have been conceived for LISA, around which the payload design is centered: Telescope Pointing (TP), which is based on the original science proposal from 1998 [4]; In-Field Pointing (IFP), which was proposed and developed as part of the LISA mission formulation study in 2006 [6], and Siderostat Pointing (SP), a concept that was detailed in 2016 [7] because potential system advantages no longer were canceled by the malus of additional large diameter optics in a LISA-constellation of reduced arm lengths. [8] Details regarding the different architectures, including their drawbacks and advantages, have been discussed in the literature. [1, 7–12]

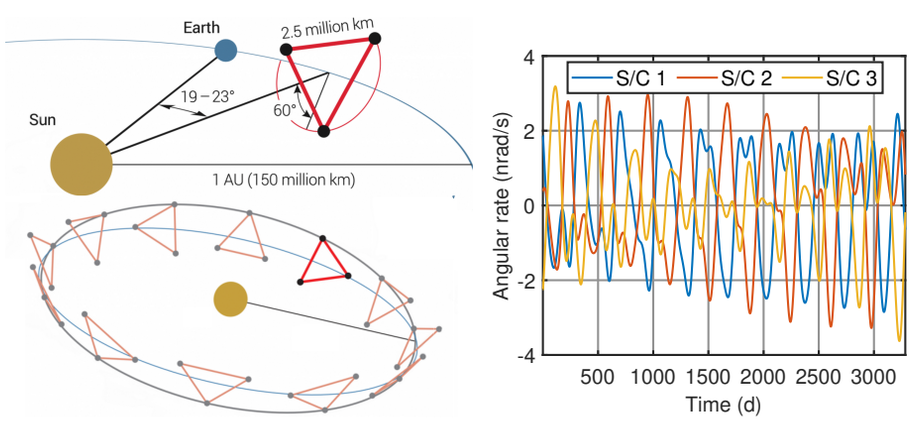

(a) (b)

Figure 1.2: a) Depiction of a typical earth trailing helio-centric orbit for the LISA constellation (Image: LISA mission consortium) and apex angle change rates for a possible simulated orbit (Data: Airbus Defence and Space).

1.2 Overview of LOS pointing concepts

Telescope Pointing In TP (see Fig.1.3a), the angular actuation of the complete - and intrinsically rigid - optical/inertial sensor head assembly is performed independently for each arm. This requires the actuation of large masses as well as backlink fiber phase referencing between adjacent Interferometer (IFO) arms, implies two complete inertial sensor assemblies

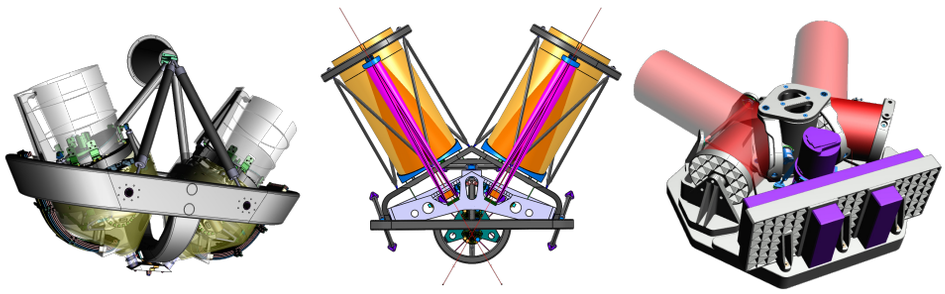

(a) (b) (c)

Figure 1.3: Example LISA payload accommodations for three pointing concepts: a) Telescope pointing: One test mass and one Optical Bench (OB) are attached to each telescope, and the entire assemblies are actuated; b) IFP: Only a small mirror in an intermediate pupil plane of the telescope is tilted actively, while telescopes and test mass(es) are situated on one fix OB; c) SP: The first mirror encountered by the incoming light acts as a folding mirror and is rotated and shifted along a linear axis in a step-stare mode to keep TTL minimal (Images: Courtesy ADS).

(Gravitational Reference Sensor (GRS)), and active suspension of four to five degrees of freedom per test mass (excluding the line of sight and the out-of-plane axis for one of the masses). While the impact of the massive flexing harnesses connected to the aforementioned Moving Optical Sub-Assembly (MOSA) and self-gravity effects of the moving parts on system performance are under investigation, telescope pointing makes use of the heritage of the GRS from the precursor-mission LISA Pathfinder and was chosen as the baseline architecture for LISA. Measuring the angular jitter and its coupling to apparent path length fluctuations (tilt-to-length coupling, TTL), one of the critical noise contributions in LISA, is challenging on-ground for TP, as the performance needs to be achieved while using gravity-offloading of the large mechanism in a representative thermal noise environment under vacuum conditions. [13][1]

In-Field Pointing In IFP (Fig.1.3b), a small mirror within an intermediate pupil plane of each of the two off-axis Korsch telescopes performs the angular actuation (also referred to as "pointing"). [10] Effects of self-gravity are negligible, as only small masses are actuated. The design also allows rigid (free space) phase referencing on a single OB with a single active GRS operated with three suspension-free positional degrees of freedom in the Drag-Free Attitude Control System (DFACS). This comes at the cost

[1] If the angular dependency of the Optical Pathlength Difference (OPD) $O_{PD}(\phi, \eta)$ is linearized around a set of nominal pointing angles (ϕ_0, η_0), an angular jitter $(\delta\phi, \delta\eta)$ will consequently cause an apparent interferometric path length jitter $\delta O_{PD} = \nabla_{\phi,\eta} O_{PD}|_{(\phi_0,\eta_0)} \cdot (\delta\phi, \delta\eta)^T$.

of additional TTL contributions due to the more complex telescope: In addition to a low Wavefront Error (WFE) over a narrow Field-of-View (FOV), similar performance must be provided over a wide FOV of up to 1° with a low field curvature, and a further alignment step of the mechanism relative to the pupil is required. However, on-ground testing of the actuation and calibration of TTL effects is possible and is demonstrated here. [14, 15] Another advantage of the IFP concept is that no flexible moving harness is required, eliminating problems ranging from stick-slip induced torque noise over gravity balancing (harness plastic deformation under launch loads or slippage during operation) and adding a massive heat bridge to high actuator force requirements (driving the size of the actuators used and the design thereof). As the IFP concept requires a second optical interface to the GRS head for low noise optical readout of a second axis, which is not present in the heritage design, it is currently considered a backup instrument architecture. [1] Still, lessons learned from investigating this payload scheme concerning the alignment of optics, TTL coupling, thermal measurements, actuator technologies, etc., can be transferred to the baseline.

Siderostat Pointing In SP (Fig.1.3c), the plane pointing mirrors are external to the telescopes, which (and the following optical assemblies) stay completely rigid (except for the Point-Ahead Angle Mechanism (PAAM) common to all architectures). [16] The SP mirrors are continuously rotated and translated stepwise. [8] Their moderate mass (compared to a MOSA) mostly eliminates the effects of self-gravity. The SP mirrors serve conventional narrow-field telescopes rigidly attached to a single OB with fixed phase reference. A single active GRS (suspension-free in positional degrees of freedom) is possible and baselined, but cold GRS redundancy without performance degradation can also be implemented. However, additional accommodation space is required for the mechanism optics, resulting in larger support structures, especially for options with full redundancy (see Fig.1.4a,1.4b).

As the pointing mirrors are not located in the pupil planes, projection effects lead to an increasing TTL coupling over time and require repositioning of the siderostat mirrors in one translational axis (about once per week, depending on the detailed design) in addition to compensating the pointing itself. [8] The actuation of the siderostat mirror thus provides the subsequent optical system with stationary beam paths while at the same time keeping the distance of the pupil-center LOS to the center of the test mass within the required limits. Figure 1.4 shows two ways of achieving GRS redundancy: translation or rotation of the two siderostat mirrors. Compared to the IFP architecture, Siderostat Pointing has the advantage of simpler telescope optics and full cold GRS redundancy without performance degradation. At the same time, higher system mass, acceleration noise due to residual self-gravity effects during pointing, and the need for two

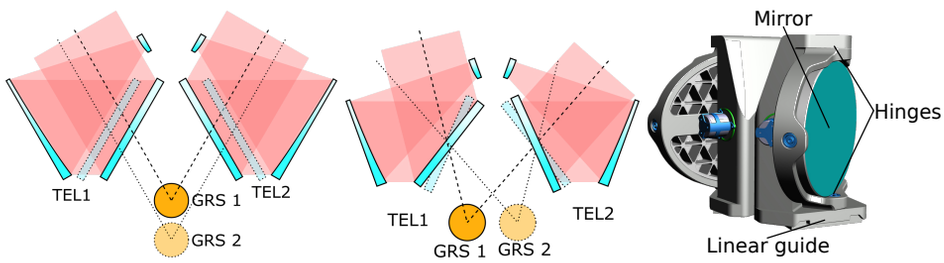

(a) (b) (c)

Figure 1.4: a) Lateral movement of the field-center of the LOS via an extended range of the linear degree of freedom of the mechanism enables accommodation of a cold-redundant GRS-head; shown are the two telescopes TEL1/2 and the inertial sensors GRS1/2. b) Alternative redundancy concept based on an extended angular range of the rotational axis, providing additional options for compact accommodation. c) SPM concept with Zerodur linear stages and hinges on the top and bottom of the mirror cage (Images: Courtsey ADS).

actuated axes are drawbacks. With smaller telescope diameters, the SP payload concept becomes more competitive regarding the payload mass. These facts and the opportunity to design and test a pointing mechanism based on previous prototypes developed for IFP made further investigations and realization of a demonstrator mechanism interesting. Developing ultra-stable mechanisms capable of performing motions in more than one degree of freedom also proves valuable in other applications, like lithography scanners used in wafer processing. In the second part of this thesis, the design of a mechanism capable of tilting a mirror around one axis and translating the mirror along another axis is detailed. The mechanism is a scaled-down version developed as a technology demonstrator in the frame of the SP payload scheme (see Fig.1.4c).

1.3 Performance validation of pointing concepts

The end-to-end validation of the optical metrology of a LISA payload using the IFP architecture, including the OB, pointing mechanism, and the telescope, is pursued in the first half of this thesis. Interferometric measurements of the optical path lengths, angles, and wavefront error measurements are employed to determine coupling factors (TTL, thermal expansion,...). Typical levels of excess apparent path length noise can be estimated using the coupling factors and characterization measurements of driving noise sources. To this end, a breadboard is completed that features the thermoelastic properties and thermal shielding necessary to obtain the levels of stability required for characterization measurements,

a quasi-monolithic heterodyne IFO with most of its components being OH catalysis bonded to a Zerodur baseplate, a scaled-down but representative telescope (off-axis Korsch three-mirror anastigmat with all-Zerodur transfer function using three aspheric mirrors followed by a refractive ocular) as well as two precision pointing mechanisms: One in the role of the IFP pointing mechanism and the other one for reenacting part of the constellation dynamics of the laser link by not only back-reflecting the laser light emitted by the telescope but also introducing beam tilt. The investigation of performance-critical aspects of IFP makes up Chapter 3 of this thesis.

In Chapter 4, a mechanism group prototype representative for the one performing the line-of-sight pointing in the SP payload architecture is dimensioned, assembled, and experimentally investigated with respect to thermal noise emission of the active components (actuators and encoders) as well as angular noise performance and creep of the linear stage. In addition, the mechanism group prototype implements several changes in design choices compared to the IFPM to address -or at least better understand- the observed effects of hysteresis and bistabilities in the IFPM. The prototype features a diamond-like carbon coated Zerodur linear guide with structured gliding surfaces to obtain an all-Zerodur transfer function for minimizing thermo elastics-driven contributions to apparent path length noise, limit creep, and mitigate the cold-welding risk. The rotational stage is made from a single piece of grade 5 titanium. It can be mounted to the Zerodur linear stage so that an isostaticity of the pointing mirror surface is maintained under changes in temperature. Optical metrology and optimized resistive sensors for thermal diagnostics are employed to verify that the mechanism group functions as desired.

Chapter 2

Theory

In this chapter, theory relevant to the understanding of the data shown is presented: Geometrical coupling of TTL effects at active mirrors, as well as aspects of TTL coupling in an off-axis telescope (of the Korsch type), are discussed. Furthermore, a semianalytical model describing the change in optical path length in dependence on the optical angle of the center ray of the IFP test setup is detailed. If the reader is unfamiliar with the IFP experiment setup and its objectives, it is highly recommended to skip this chapter for now and read chapter 3, up to section 3.3, first. Otherwise, context may be missing. Definitions of the interferometric phase for generic IFOs using Quadrant Photodetectors (QPDs) for phase readout will be introduced. Their impact on the measurement and the scheme for compensation of linear TTL will be investigated in section 3.4. A short overview of potential noise sources in heterodyne interferometry will be presented in Appendix A. While brevity is preferred over exhaustive discussion of material that can be expected to be familiar to a reader of a document this specific, numerous sources from the literature detailing the effects discussed will also be provided throughout the following chapters.

2.1 Piston at active mirrors

The TTL effects introduced by a pointing mirror, including its static contributions (alignment offsets) as well as dynamic ones (hinge center shift, dependent on the tilt of the pointing mirror), are also referred to as piston at active mirrors when the OPD is described instead of its derivative. In the following, relevant geometric effects are detailed.

While shifts of the (ideal) substrate of a planar pointing mirror parallel to its surface do not affect the piston generated by the mirror, any shift ($\vec{AR}$) of the mirror's center of rotation with respect to the location the ray impinges on (named A here) may contribute. [17] The rotational angle α is set such that for a given change in angle of incidence equal to 2α, the reflected beam is still parallel (while laterally displaced) to the reflected ray at the nominal incidence angle ('zero ray' @ φ_0). This corresponds to an active pointing scenario, where the mirror is actuated in tilt such that the output beam tilt is kept (near) static. For now, a perfect alignment of the mirror in its holder is assumed, such that the mirror is not tilted and the hinge center location(s) part of the plane defined by the mirror surface. From Fig.2.1, it follows that the OPD is given by the sum of the distances between points A and B and between points B and C (where A marks the intersection with the reference, B the location the beam impinges on, and C the intersection of the reflected beam with the reference plane).

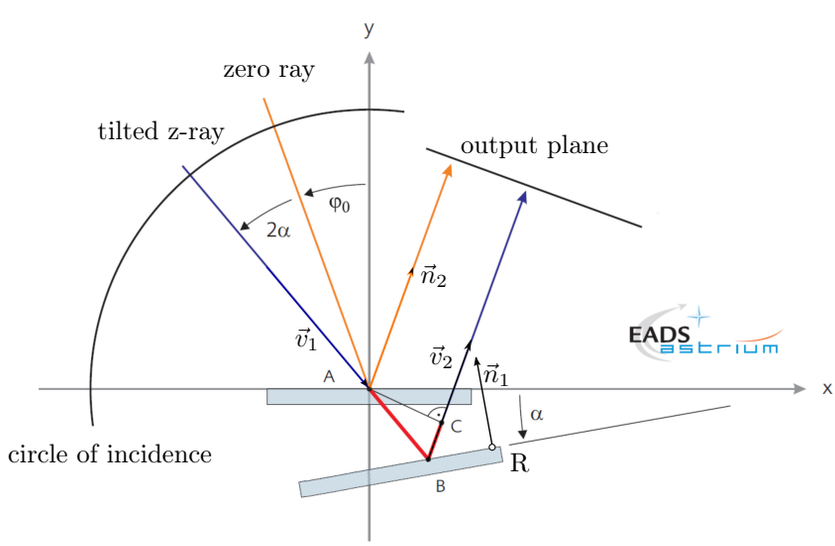

Figure 2.1: Schematic piston and beam displacement for an active mirror pointing device. Adapted from Ref. [18].

For the reflection of a ray off a surface defined locally by its surface normal $\vec{n}_i$ as well as a support/position vector $\vec{R}_i$ for the i-th reflection, new

directional vector $\vec{v}_{i+1}$ and the intersection point X_{i+1} of the incident ray, respective the supporting vector of the reflected ray are given by:

$$\vec{v}_{i+1} = \vec{n}_i - 2(\vec{v}_i \cdot \vec{n}_i)\vec{n}_i \tag{2.1}$$

$$\vec{n}_i \cdot (\vec{X}_{i+1} - \vec{R}_i) = 0 \tag{2.2}$$

with $\vec{X}_{i+1} = a_i\vec{v}_i + \vec{X}_i$ where $\vec{X}_1$ is a position vector that maps the origin to point A, which is identical to the coordinate origin here. From A onward, a phase difference is collected in case of the pivot being located at a position not identical to the origin and $\alpha \neq 0$ for the scenario shown. Solving for a_i such that equation 2.1 is true with a_i being a real number yields the distance (and direction) traveled to the next intersect in case the directional vectors are normalized to unity length. It follows that

$$\begin{aligned} O_{PD}(\varphi) &= |AB| + |BC| \\ &= |a_1\vec{v}_1| + \left|\vec{v}_2 \frac{\vec{n}_2 \cdot a_1\vec{v}_1}{\vec{n}_2 \cdot \vec{v}_2}\right| \qquad \text{with} \qquad a_1 = \frac{\vec{n}_1 \cdot \vec{R}_1}{\vec{n}_1 \cdot \vec{v}_1} \\ &= (\Delta x \sin(\alpha) - \Delta y \cos(\alpha)) \cdot 2 \cdot \cos(\varphi_0 + \alpha) \end{aligned} \tag{2.3}$$

for the scenario in Figure 2.1 with

$$\vec{n}_1 = \begin{pmatrix} \sin\alpha \\ -\cos\alpha \\ 0 \end{pmatrix}, \vec{n}_2 = \vec{v}_2 = \begin{pmatrix} \sin\varphi_0 \\ \cos\varphi_0 \\ 0 \end{pmatrix}, \vec{v}_1 = \begin{pmatrix} \sin(\varphi_0 + 2\alpha) \\ -\cos(\varphi_0 + 2\alpha) \\ 0 \end{pmatrix}$$

$$\vec{X}_1 = \vec{A} = \vec{R}_2 = \begin{pmatrix} 0 \\ 0 \\ 0 \end{pmatrix}, \qquad \vec{X}_2 = a_1\vec{v}_1, \qquad \vec{R}_1 = \vec{R} = \begin{pmatrix} \Delta x \\ \Delta y \\ 0 \end{pmatrix}$$

The total motion of the rotational axis/ mechanical pivot situated at R is described by:

$$\begin{pmatrix} \Delta x \\ \Delta y \end{pmatrix} = \begin{pmatrix} x_0 + \Delta x_h \\ y_0 + \Delta y_h \end{pmatrix} \tag{2.4}$$

where (x_0, y_0), defined at $\alpha = 0$, is a static misalignment of the rotational axis due to the imperfect placement in the setup, and $(\Delta x_h(\alpha), \Delta y_h(\alpha))$ is the parasitic motion of the hinge in the reference frame as defined above. In the case of the IFPM, for example, this coordinate system is rotated with respect to the coordinate system of the optical bench, which serves as a reference system for the optical (interferometric) measurements (also see Fig.2.6). Therefore, coordinate transformations have to be performed such that misalignments are correctly transferred to the reference frame defined by the coordinate system used above.

2.2 Mitigation of TTL using pupil imaging

In Figure 2.2, a typical scenario for an interferometric measurement is shown, where the phase is detected by tracking the beat of a reference beam (local oscillator (LO)) and a measurement beam (signal). The measurement beam is tilted by an angle Θ about a pivot point at a longitudinal distance Δz from the detector (a segmented quadrant photodetector (QPD). Additionally, a lateral shift x of the detector, defining the pupil of the setup, causes linear TTL. The variable Δx describes a lever arm due to beam wandering caused by the longitudinal offset that depends linearly on the tilt introduced (for small tilts). The optical pathlength difference between signal and local oscillator $\delta(\Theta, x)$ is given by:

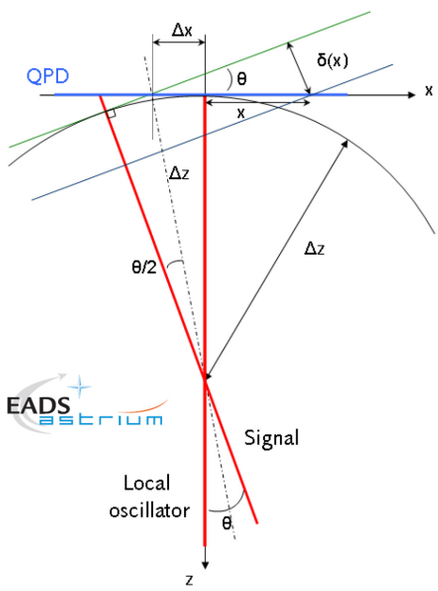

Figure 2.2: Sketch of a typical scenario where the detector is at an offset to the pivot in a pupil plane (Image: Courtesy ADS).

$$\begin{aligned}\delta(\Theta, x) &= x \cdot \sin(\Theta) + \Delta z(1 - \cos(\Theta)) \\ &= (x + \Delta x) \cdot \sin(\Theta) \\ &= \left(x + \Delta z \tan\left(\frac{\Theta}{2}\right)\right) \cdot \sin(\Theta) \\ &\approx x \cdot \Theta + \Delta z \cdot \frac{\Theta^2}{2},\end{aligned}$$

where one can perform first-order Taylor approximations for small angles Θ to further simplify the result. To mitigate second-order TTL from a (large) longitudinal offset and undesired effects due to the beam laterally moving in the detector plane (such as the beam leaving the detector area), the plane the pivot is situated in, which by design should be an (intermediate) pupil plane, is imaged onto the detector. [19, 20] In TTL measurements probing the OPD around small field angles, which are part of the completion of the integration and alignment of the pupil imaging in chapter 3, the OPD will assume the shape of a parabola, where a non-zero shift of the extrema indicates a lateral pupil offset and the steepness of the slope indicates a longitudinal offset, that is reduced with each relay stage that is added.

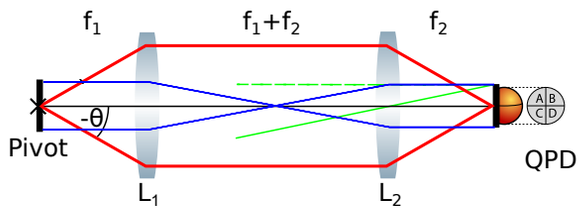

Figure 2.3: Typical example of an imaging system using two lenses: The pivot point/ axis is imaged onto the detector plane. In the case depicted, the relay distance is twice the sum of the focal lengths of the individual lenses. The z-axis points along the optical axis of the setup from left to right, and the x-axis is orthogonal to this, pointing in the radial direction.

This can, for example, be achieved by using a refractive relay optic constituted of two thin lenses with focal lengths f_1 and f_2 as shown in Figure 2.3 (curved mirrors could also be used, but tend to by more sensitive to misalignments).

For the scenario described above, using ray transfer matrices, one obtains the following relation for a distance to the optical axis x on the input side of the relay beam expander towards the beam pivot and $\tilde{x}$ in the detector plane as well as for the tilt of the ray (angle to optical axis) Θ on the input side towards the intermediate pupil the pivot point is situated and the angle $\tilde{\Theta}$ for the tilt of the ray with respect to the optical axis in the detector plane:

$$\begin{aligned}\begin{pmatrix}\tilde{x}\\ \tilde{\Theta}\end{pmatrix} &= \begin{pmatrix}1 & f_2\\ 0 & 1\end{pmatrix}\begin{pmatrix}1 & 0\\ -\frac{1}{f_2} & 1\end{pmatrix}\begin{pmatrix}1 & f_1+f_2\\ 0 & 1\end{pmatrix}\begin{pmatrix}1 & 0\\ -\frac{1}{f_1} & 1\end{pmatrix}\begin{pmatrix}1 & f_1\\ 0 & 1\end{pmatrix}\begin{pmatrix}x\\ \Theta\end{pmatrix}\\ &= \begin{pmatrix}-\frac{f_2}{f_1}x\\ -\frac{f_1}{f_2}\Theta\end{pmatrix} \Rightarrow x\cdot\Theta = \tilde{x}\cdot\tilde{\Theta}\end{aligned} \tag{2.5}$$

$$q(z) = \frac{A\cdot q_0 + B}{C\cdot q_0 + D} \Rightarrow q\left(2\cdot(f_1+f_2)\right) = \frac{-\frac{f_2}{f_1}\cdot q_0}{-\frac{f_1}{f_2}} = M^2\cdot q_0 \tag{2.6}$$

Here, one can immediately notice that the lateral beam position is invariant under changes in angle in paraxial approximation and for thin lenses. Also, the phase difference measured due to lateral offsets is invariant, as multiplying the scaled lever-arm with the inversely scaled angle cancels out the magnification M=$\frac{f_2}{f_1}$. The same is true for TTL originating in longitudinal offsets that are magnified by a factor M^2, whereas the angle is scaled inversely with the magnification, such that $\Delta z\cdot M^2\cdot(\Theta/M)^2$ is invariant as well. However, non-geometric TTL may be present if, due to the imaging, the wavefronts of reference and measurement beams are no longer matched well (as the curvature is altered for non-unity magnification, even if the wavefront is not distorted otherwise). In the following setups, this

won't be an issue. In LISA, those effects contribute significantly and must also be considered. Due to the invariance of TTL coupling under imaging, imaging systems allow the highly effective mitigation of second order TTL; as without them, additional beam wandering would result. Consequently, the effects of spatially inhomogeneous detectors are reduced as well. Avoiding lateral offsets, on the other hand, requires adjustments to the alignment of the detector, the ray pivot location, the relay pupil imaging optics, or, preferably, ideal placement of the optics and ray pivot as well as the capability to introduce beam tilt without any parasitic motion caused by non-linear hinge deformation. The above does not require imaging of the pupil onto the detector plane, but that of the plane the pivot is situated in, which the beam is rotated around. However, if the aperture stop of the system coincides with that plane, the effects of clipping (such as diffraction) resulting in (non-geometrical) TTL can be mostly ignored. In Fig.2.3, the photodetectors are the defining aperture stops, same as in the setup for performance validation of the IFP concept presented later on (for the IFP telescope is also an afocal one; green lines used for construction of the exit pupil are intersecting at the location of the exit pupil).

2.3 TTL of a Korsch type off-axis telescope

A Korsch-type telescope design features a low Petzval field curvature, wide FOV, and low aberrations at the cost of tight alignment tolerances. [21, 22] It can be tuned to be near anastigmatic. [23]

The recently implemented James Webb Space Telescope (JWST), is an example for a famous Korsch-type telescope.

In addition to being optimized for minimal wavefront distortion and a wide FOV with minimal field curvature towards higher field angles, the IFP telescope comes as an off-axis version of the Korsch design, reducing stray light to a minimum and avoiding (central) clipping by the second curved mirror, which adversely impacts differential wavefront sensing as well as phase measurements. [24] While stray light is not critical to the experiments the IFP setup is intended for, in LISA very low levels of stray light are essential, as they degrade the performance of the phase read-out, even when using balanced detection schemes, and could furthermore result in a saturation of the detectors. As using an off-axis telescope can thus be considered mandatory, this more challenging to manufacture and expensive option to integrate compared to a standard design was chosen for the IFP performance validation breadboard to make the feasibility study more representative and raise its credibility level. As mentioned before, the IFP telescope was optimized for a minimal WFE. This ensures a minimal angular gradient in the phase of the wavefront at a given distance far away (the location of the distant S/C). However, it should be noted that certain aberrations contribute less to far-field TTL resulting from such gradients,

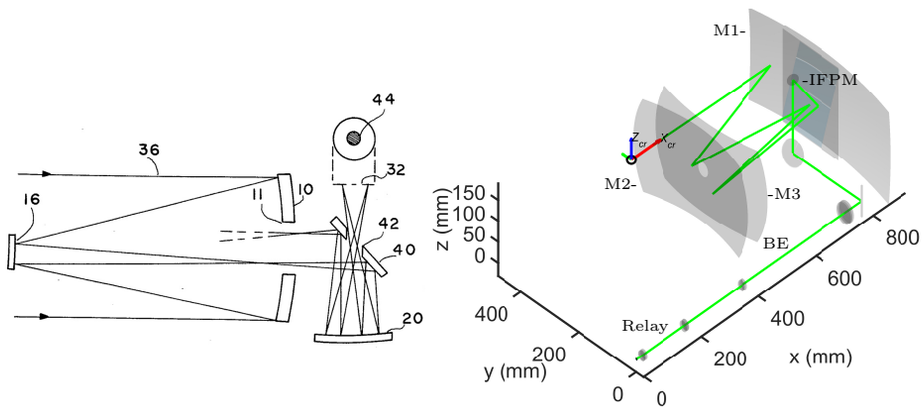

(a) (b)

Figure 2.4: a) The original Korsch telescope design is a three-mirror on-axis anastigmat (Figure taken from US4101195 [21]). b) In the IFP breadboard, a folded off-axis Korsch followed by two refractive stages is used. The figure was created using code based on the Matlab toolbox Optometrica.

such that higher contributions of those to the WFE may be acceptable. [25] This could be accounted for in the optics design, which should not aim at a high imaging quality as in classical telescope design but rather minimize TTL coupling. Such a design, however, would require specifying relaxed requirements for certain contributions of the WFE, thus driving manufacturing costs due to additional validation steps being required. Therefore, such consideration would only be beneficial if manufacturing does not allow keeping certain aberrations small, which do not contribute to far-field TTL.

The OPD dependency of the chief ray tilt of an off-axis telescope may feature certain symmetries depending on how the central ray incident to the telescope is scanned. In the IFP telescope, a rotation of the central ray in the constellation plane (see Fig.2.6a, corresponds to a rotation of the green chief ray about the pivot point encircled in black around the axis y_{cr}) yields a near purely even symmetry in plots of OPD versus in-plane angle. The resulting symmetry for angular scans along the off-axis angle (out-of-plane, this axis of rotation is identical to z_{cr} in 2.6a) is not as obvious. However, mostly uneven contributions are to be expected. By performing a ray tracing analysis using a heavily customized raytracer based on Matlab toolbox Optimetrika, the expectations regarding the telescope's response in terms of OPD when varying the angle of the chief ray incident are confirmed: The black curve in Figure 2.5a shows that the OPD vs. the central ray angle in the external pupil for scans of the in-plane angle is given by a combination of even polynomials in case of the IFP telescope. It is this degree of freedom that is nominally acted upon by the pointing mechanism during active pointing

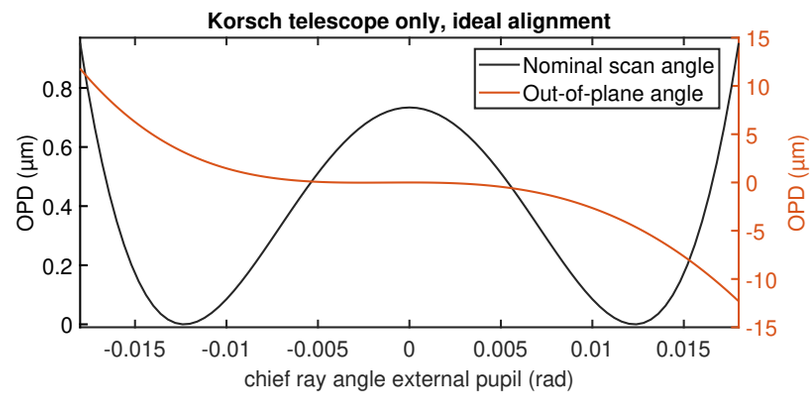

(a)

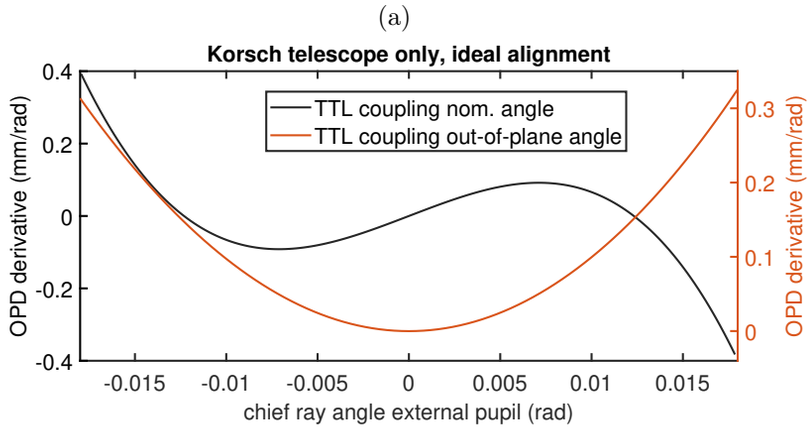

(b)

Figure 2.5: a) OPD vs. optical chief ray angle of the IFP reflective telescope stage. b) TTL coupling for small angle jitter of in- and out-of-constellation plane angular jitters for the entire FOV covering the entire pointing range. The OPD is shown for a single pass, scanning the chief ray. For details, please refer to the text. Computed using a custom raytracer.

to compensate for the angular breathing of the constellation. The red curve gives the change in optical path length versus the out-of-plane angle: While contributions of uneven functions dominate the OPD, the polynomial is constituted of both even and uneven functions. The OPD derivative in the in-plane angle gives the TTL along the nominal scan direction (see Fig.2.5b, black curve). Additionally, the TTL due to out-of-plane jitter is calculated over the entire nominal pointing range by performing out-of-plane tilt scans for a large number of in-plane angles (red curve). For a LOS jitter of $10\,\mathrm{nrad}/\sqrt{\mathrm{Hz}}$ both in- and out-of-plane, the geometrically summed path length jitter thus is well below $5\,\mathrm{pm}/\sqrt{\mathrm{Hz}}$. The exit pupil shift in the complete telescope's detector plane, including refractive magnifying and relay stages, is shown in Figure 2.6b, where y is the horizontal and z is

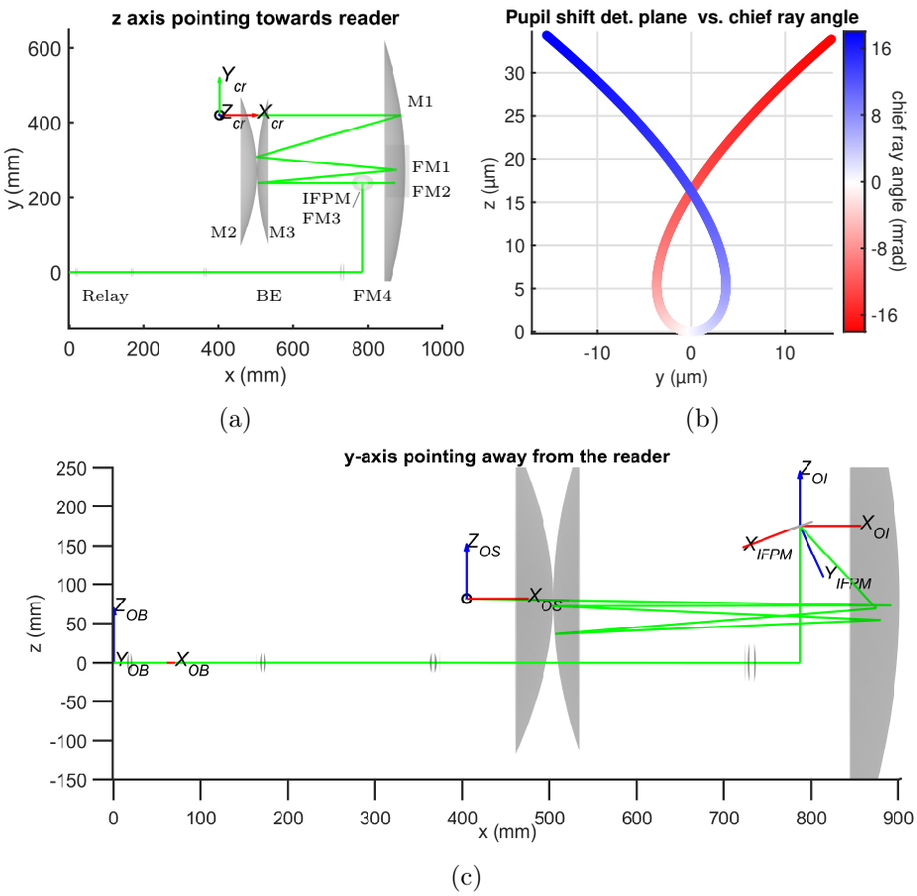

Figure 2.6: a+c) Top and side-view of the IFP setup, including refractive magnifying and relay stages. Shown are the parent mirror surfaces of the Schiefwinkler telescope. Also shown are the coordinate systems of the OB, Chiefray (C_{cr}) for the definition of the pointing angles, SCS (C_{OS}), and IFPM (C_{OI} for shifts in the OB system relative to the nominal position, C_{IFPM} for describing TTL in the coordinate frame of the IFPM nominal frame as defined in the section on piston at active mirrors). b) Wandering of the pupil over the entire pointing range, axis are toggled due to the periscope IFPM-FM3.

the vertical displacement on the detector caused by a linear increase of the in-plane angle. The trajectory is color-coded, representing the value of the in-plane scan angle the pupil shift was calculated for. For raytracers not considering lateral detector offset TTL, this trajectory can be used to separately describe the change in OPD due to beam wandering. [26] The raytracer used here can take into account the geometric contributions of the pupil shift and dedicated numerical simulations in Matlab were performed

to investigate non-geometric contributions as well (see section 3.4). The (purely geometrical) OPD of the telescope in dependence on the in-plane or nominal pointing angle can be described sufficiently well by a simple polynomial $O(\varphi)$:

$$\mathrm{O}_i(\varphi) = a_i \cdot \varphi^4 + b_i \cdot \varphi^2 \tag{2.7}$$

where φ shall be the nominal pointing angle in-plane (on the level of the IFPM, see Fig.2.6c, the axis of rotation is identical to both y_{OI} or z_{IFPM}, rotation counter-clockwise (looking in positive y_{OI} direction) corresponds to an increase in angle) and a_i and b_i are coefficients that depend on the detailed telescope design and alignment for a scenario denoted by index i. These coefficients can be either experimentally or numerically determined, for example, using a raytracer. For misalignments, uneven polynomials may have to be added.

2.4 Semi-analytical model of the setup

By combining the description of telescope OPD using polynomials with the model of OPD at active mirrors and including the results of Finite Element Modeling (FEM) of parasitic hinge deformations to account for variations in misalignments over scan angles of the active mirrors, one can model the OPD of the entire IFP setup. It is important to be aware that the description of TTL at active mirrors and that of TTL originating in the telescope using numerical raytracing does not consider the effects of WFEs, diffraction, and scanning of surface irregularities in the calculation of RX TTL (also see Ref. [27]). However, the phase detection entails the interaction of the two Gaußian beams (in the experiment probing the performance of the IFP concept or Gaußian and Flat-top in case of LISA) of imperfect wavefronts with a QPD. Non-geometrical effects also have a significant contribution to TTL and must be accounted for. Therefore, the beam parameters of the signal and the local oscillator beam were measured, and the scenario detailed above was investigated in dedicated simulations (see section 3.4 for more details). Those simulations yielded a near-linear response in OPD to lateral offsets of the detector under scans of the in-plane angle in the case of the IFP setup, with slightly modified values for the TTL compared to the purely geometrical case. Thus, based on numerical and analytical considerations, one can model the entire IFP setup and every scenario from a partially integrated setup to a fully integrated setup. In particular, the system behavior in terms of OPD for different types of scans in beam tilt performed using mechanisms featuring active mirrors can be included. For each scenario, the inputs are modified accordingly. If deviations become apparent, this immediately hints at additional misalignments; the (likely) candidates can be pinned down by a combination of raytracing and Monte-

Carlo simulations. As discussed, the OPD at active mirrors depends on various misalignments that can vary for different tilts.

These variations can occur due to parasitic hinge deformations, for example. The trajectories of the hinges' center of rotation (here coinciding with the mirror surface as per definition for $y_m = 0$, see [17]) were numerically determined for both the SCS and for the IFPM (designed by Netherlands Organization for Applied Scientific Research (TNO)) through FEM. [27, 28] The situation is slightly complicated because five distinct coordinate systems were used to determine parasitic hinge motions, raytracing, and description of the piston at active mirrors in Ref. [18]. Table 2.1 declares the model parameters and variables regarding misalignments of the SCS and IFPM mirrors. Besides the name of the parameters and variables and a short description, the coordinate system they are defined in C_{xy} is specified. The coordinate systems are illustrated in figures 2.6a and 2.6c.

Parameter	C_{xy}	**Displacement**
x_{I0}	x_{OI}	IFP mirror static disp.
z_{I0}	z_{OI}	IFP mirror static disp.
y_{mI}	y_{IFPM}	IFP mirror disp. in its holder
y_{S0}	x_{OS}	SCS mirror static disp.
x_{S0}	z_{OS}	SCS mirror static disp.
y_{mS}	x_{OS}	SCS mirror disp. in its holder
φ_0	$\varphi_{y\mathrm{OI}}$	IFPM mirror tilt offset due to folding
φ_{S}	$\varphi_{y\mathrm{OS}}$	SCS mirror tilt
L_i	x_{OB}	dist. beam pivot to det. plane
y_{det}	y_{OB}	lat. offset of beam phase center and detector
x_{IH}	x_{IFPM}	IFPM hinge center/ beam pivot point shift
y_{IH}	y_{IFPM}	dyn.IFPM hinge center/ beam pivot point shift
x_{SH}	$-z_{\mathrm{OS}}$	dyn. SCS hinge center/ beam pivot point shift
y_{SH}	x_{OS}	dyn. SCS hinge center/ beam pivot point shift
x_{I}	x_{IFPM}	tot.IFPM hinge center/ beam pivot point shift
y_{I}	y_{IFPM}	tot.IFPM hinge center/ beam pivot point shift
x_{S}	$-z_{\mathrm{OS}}$	tot.SCS hinge center/ beam pivot point shift
y_{S}	x_{OS}	tot.SCS hinge center/ beam pivot point shift
φ	$\varphi_{y\mathrm{IFPM}}$	relat. opt. angle in-plane at IFPM wrt. φ_0

Table 2.1: Displacements taken into account in the semi-analytical model and the respective coordinate systems they are defined in. The sign of angles in the OB system is toggled with respect to convention (not mathematically positive, but negative; corresponding to an increase in clockwise rotation).

The coefficients of telescope polynomials for three different scenarios are shown in Table 2.2.

		Tel. polyn. coefficient	
Scenario	**No.**	a (mm/rad^4)	b (mm/rad^2)
RT ideal alignment	1	47.71	-0.3832
Nikolov Zemax ideal	2	51.43	-0.3889
RT misaligned	3	49.19	0.2269

Table 2.2: Telescope polynomial parameters for the three different scenarios detailed in the text.

Scenario number one covers the ideal placement of the optics, including a corrective term for the angle of the IFPM mirror tilt, such that the interferometrically measured angle in the detector plane (measured by Differential Wavefront Sensing (DWS)) is always kept close to zero (defined by Local Oscillator (LO) beam alignment and wavefront distortion). Next, the coefficients for scenario number two are shown, which has been computed as part of IFP telescope design study and does not include the previously mentioned corrective term, nor detector offset TTL (rather the detector is treated as moving with the pupil).
Finally, scenario number three corresponds to a misaligned telescope (M3: 1 mrad clocking corresponding to a rotation of the parent mirror about the location the beam is incident on and around an axis oriented like the x_{OB}-axis, but shifted such that the axis intersects with the point of incidence on the mirror surface (see Fig.2.6a) as well as a shift $\Delta x_{OB} = 0.5\,\mathrm{mm}$, FM1: $\Delta x_{OB} = -1\,\mathrm{mm}$), but otherwise identical to the first scenario.

So far, the telescope polynomials for the different scenarios do not account for parasitic deformations of the hinges of SCS and IFPM. The trajectories of the parasitic motions of the hinges are interpolated based on FEM analysis results by fitting suitable polynomials. While these interpolants are not physical models of the behavior of the hinges, they allow the simple and rather practical description of the OPD over optical tilt in the IFPM plane (Table 2.3). For the various measurement configurations, such as small field angle scans and scans over the entire FOV of the telescope, some parameters need to be modified and additional parameters need to be introduced: For example, the distance between pivot and detector plane L_i depends on the presence and alignment of relay stages and thus is different at the various stages of the integration of the setup. The same is true for the magnification of the optical angle on the IFPM level to the respective reference frame (either detector plane ($M > 1$) or external pupil plane ($0 < M < 1$), where the SCS is positioned). Also, the angular range of scans for a step size A and the number of total steps and ramps the scan of the mechanical angles of the two mechanisms is comprised of, represented by the

	Parasit. Hinge deformations		
Variable	function	c_i	d_i
x_{IH}	$c_1 \cdot (\varphi/2)^3 + d_1 \cdot (\varphi/2)$	$202.6\,\mathrm{nm/rad}^3$	$-2.781\,\mathrm{nm/rad}$
y_{IH}	$c_2 \cdot (\varphi/2)^2$	$-420.6\,\mathrm{nm/rad}^2$	-
x_{SH}	$c_3 \cdot (\varphi/5)$	$1910\,\mathrm{nm/rad}$	-
y_{SH}	$c_4 \cdot (\varphi/5)$	$-26\,740\,\mathrm{nm/rad}$	-

Table 2.3: The hinge center shifts given approximately by the functions above correspond, for a perfect mirror alignment in the holder, to a translation of the rotational axis/pivot coincident with the mirror surface.

interval I, changes with each scenario. Scan mode dependent contributions of detector offset TTL for the different scenarios are taken into account by the distinct magnifications of optical angle in the IFPM plane to the detector plane: M_I and M_{SCS} for scanning the either IFPM or the SCS. If both mechanisms are scanned, the magnification of the angle in the SCS to the detector plane is 0, see below. Speaking of the details of the angular actuation, two different Modi are relevant here:

- Both mechanisms perform a continuous scanning motion. In the simplest of cases, a mechanism performs a motion at a constant angular rate. The other mechanism introduces tilt such that the beam tilt is compensated, resulting in a near-static beam in the detector plane with an angle close to zero relative to the LO. Due to the magnification in angle being dependent on the field angle, a higher order iterative correction can be applied (This was only done for the full-fledged raytracing, such that the IFPM is actuated in a way that the receive (direction) (RX) always is kept collinear to the normal of the detector plane as well as the LO beam.).

- One mechanism performs a step-stare motion to compensate for the tilt introduced by the other mechanism before DWS signal linearity and unambiguity are lost. In contrast, the other mechanism introducing tilt is actuated at a constant angular rate over the entire FOV.

In the first mode, only the total OPD of the system can be recorded in dependence on the pointing angle over the entire pointing range. Contributions caused by parasitic deformations of the mechanisms' hinges and misalignments of the pointing mechanism can not be differentiated from telescope OPD. In the second mode, contributions (of parasitic hinge deformations) of either IFPM or SCS and telescope are encoded in the discrete steps and thus can easily be removed, allowing the retrieval of those contributions.[1] Using Gauss brackets allows for a very compact description

[1] Effects of the refractive stage of a higher order than three would result in systematic errors but are not expected to occur here.

of parametrized optical tilt introduced by actuation of SCS and IFPM by decomposition of a linear tilt trajectory into a superposition of a step- and a sawtooth motion:

$$\varphi_1(t) = A \cdot \lfloor t \rfloor \qquad \text{for} \qquad t \in I \tag{2.8}$$

where $\varphi_1(t)$ describes a stepping motion with A being an amplitude corresponding to the size of a step, and t being a parameter that can be changed within certain bounds. A suitable sawtooth function yielding the desired motion is given by $\varphi_2(t)$:

$$\varphi_2(t) = A \cdot \left(t - \lfloor t \rfloor - \frac{1}{2} \right) \qquad \text{for} \qquad t \in I \tag{2.9}$$

	Alignment status			
Variable	T1	T2	T3	T4
L_1	-	1.2133 m	-	-
L_2	-	-	0.2493 m	-
L_3	0.0005 m	-	-	0.0005 m
M_I	10	2	10	10
M_SCS	25	5	25	25
I	$[-1800, 1800]$	$[-0.5, 0.5]$	$[-0.5, 0.5]$	$[-0.5, 0.5]$
A	50 000 nrad	500 000 nrad	100 000 nrad	100 000 nrad

Table 2.4: Values for the alignment scenario dependent parameters. The scenarios Tx are detailed in the text.

The FOV of the telescope and IFO define limits regarding the angular range given by the number of steps I, as well as the step size A, for the various cases. Alignment status T1 corresponds to the fully integrated setup and angular actuation over the entire FOV of the telescope; T2 to the setup before integration of any refractive stage; T3 to the setup post integration of the refractive 5x stage, and T4 yet again to the fully integrated setup and scans over small field angles.

Putting it all together Now that the model parameters, the trajectories of the mirrors in terms of angular as well as translatory motions are defined and that the mathematical description of TTL effects at active mirrors and in a Korsch-type off-axis telescope have been discussed, one can put it all together: By defining functions for the piston generated by the actively pointing mirrors due to static and dynamic misalignments introduced by placement or simply the design of the hinges themselves, using telescope polynomials to approximate the behavior of the Korsch telescope with the input of that function adapted to each scan scenario as well as introducing

a function that takes into account the TTL contributions by detector misalignment as well as the level of integration of the setup, a semi-analytic model presents itself, that can be used to describe all scenarios encountered later on in the experiments. Misalignments of the refractive optics can be investigated using the raytracer or ray transfer matrices. Misalignments in the lateral position of a single refractive element always result in a shift of the beam and LOS off-pointing in case of the 5x BE that can be corrected by introducing tilt via actuation of the IFPM for the in-plane angle. Such misalignments are highly undesirable, as well as their use to compensate linear TTL utilizing IFPM piston, because they tend to result in poorer quality of the wavefronts and may compromise the ability of the IFPM to perform the entire stroke in both directions, as a portion of the range is used for compensation already.
The trajectory of the mirror surfaces of the IFPM (x_I,y_I) and of the SCS (x_S,y_S) are given by:

$$\begin{pmatrix} x_\mathrm{I}(\varphi) \\ y_\mathrm{I}(\varphi) \end{pmatrix} = \begin{pmatrix} x_\mathrm{IH}(\varphi) - y_\mathrm{mI} \sin\left(\frac{\varphi}{2}\right) \\ y_\mathrm{IH}(\varphi) + y_\mathrm{mI} \cos\left(\frac{\varphi}{2}\right) \end{pmatrix} + \begin{pmatrix} -\cos(\varphi_0) & -\sin(\varphi_0) \\ \sin(\varphi_0) & -\cos(\varphi_0) \end{pmatrix} \begin{pmatrix} x_\mathrm{I0} \\ z_\mathrm{I0} \end{pmatrix}$$

$$\begin{pmatrix} x_\mathrm{S}(\varphi) \\ y_\mathrm{S}(\varphi) \end{pmatrix} = \begin{pmatrix} x_\mathrm{SH}(\varphi) - z_\mathrm{S0} \\ y_\mathrm{SH}(\varphi) + x_\mathrm{S0} \end{pmatrix} + \begin{pmatrix} 0 & -\sin\left(\frac{\varphi}{5}\right) \\ 0 & \cos\left(\frac{\varphi}{5}\right) \end{pmatrix} \begin{pmatrix} 0 \\ y_\mathrm{mS} \end{pmatrix} \tag{2.10}$$

$$\mathrm{O}_\mathrm{RLI}(\varphi_2) = L_3\left(\cos(10\varphi_2) - 1\right) + L_2\left(\cos(10\varphi_2) - 1\right) + L_1\left(\cos(2\varphi_2) - 1\right) \tag{2.11}$$

$$\mathrm{O}_\mathrm{RLS}(\varphi_2) = L_3\left(\cos(25\varphi_2) - 1\right) + L_2\left(\cos(25\varphi_2) - 1\right) + L_1\left(\cos(5\varphi_2) - 1\right) \tag{2.12}$$

$$\mathrm{O}_\mathrm{det}(\varphi_2) = M_x \cdot \varphi_2 \cdot y_\mathrm{det} \tag{2.13}$$

The above equations describe OPD due to longitudinal (pupil) offsets of the pivot points for scans performed using the IFPM (*RLI*) and SCS (*RLS*) as well as that of (additional) detector offset TTL. For scanning both mechanisms simultaneously such that the IFPM compensates the angle introduced by the SCS, the OPD can be described by (indices x denotes the telescope alignment scenario number, see Table 2.2):

$$\begin{aligned} \mathrm{O}_\mathrm{both} =& 2 \cdot \mathrm{O}_x(\varphi) \\ &+ 4\cos\left(\frac{-2\varphi_0 + \varphi}{2}\right)\left(x_\mathrm{I}(\varphi)\sin\frac{\varphi}{2} + y_\mathrm{I}(\varphi)\cos\frac{\varphi}{2}\right) \\ &- x_\mathrm{S}(\varphi)\sin\left(\frac{\varphi}{5}\right) + y_\mathrm{S}(\varphi)\cos\left(\frac{\varphi}{5}\right) \end{aligned} \tag{2.14}$$

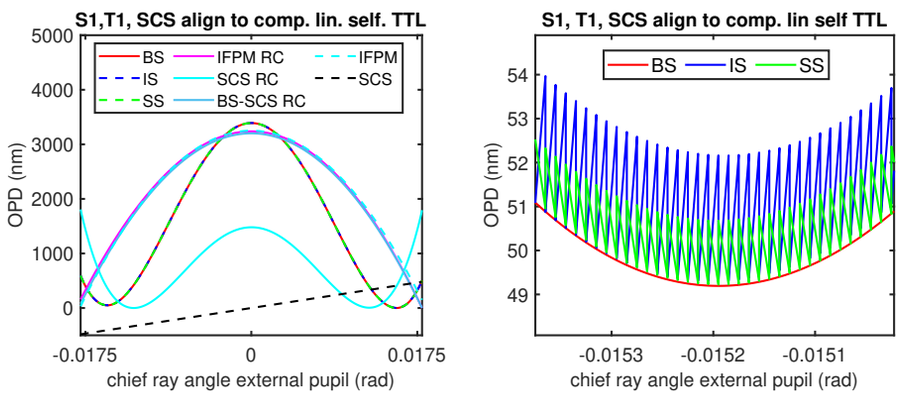

(a) (b)

Figure 2.7: a) OPD vs. optical chief ray angle of the IFP setup: BS: Both scan, IS: IFPM scans, SCS steps, SS: SCS scans, IFPM steps, IFPM RC: IFPM effects reconstructed by removal of system OPD encoded in steps, BS-SS RC: IFPM effects reconstructed by removal of system OPD, IFPM/SCS: Contributions of hinge deformations of the respective mechanism, SCS RC: Removal of steps encoding IFPM effects; left are higher order SCS effects and system OPD. b) Zoom showing the behavior of OPD under different scan variants.

For scans of the IFPM mechanism and steps of the SCS, we obtain:

$$\begin{aligned}\mathrm{O}_{\mathrm{IS}} =& \mathrm{O}_x(\varphi) + \mathrm{O}_x\left(\varphi_1 - \varphi_2\right) + \mathrm{O}_{\mathrm{det}}\left(\varphi_2\right) + \mathrm{O}_{\mathrm{RLI}}\left(\varphi_2\right) \\ &+ 2\left(\cos\left(\frac{-2\varphi_0+\varphi}{2}\right) + \cos\left(\frac{-2\varphi_0+\varphi+2\varphi_2}{2}\right)\right) \\ &\cdot \left(x_{\mathrm{I}}\left(\varphi\right)\sin\frac{\varphi}{2} + y_{\mathrm{I}}\left(\varphi\right)\cos\frac{\varphi}{2}\right) \\ &- \cos\frac{\varphi_2}{5}\left(x_{\mathrm{S}}\left(\varphi_1\right)\sin\left(\frac{\varphi_1}{5}\right) - y_{\mathrm{S}}\left(\varphi_1\right)\cos\left(\frac{\varphi_1}{5}\right)\right)\end{aligned} \tag{2.15}$$

And finally, for scanning of the SCS mechanism and stepping of the IFPM, we obtain:

$$\begin{aligned}\mathrm{O}_{\mathrm{SS}} =& \mathrm{O}_x(\varphi_1) + \mathrm{O}_x\left(\varphi\right) + \mathrm{O}_{\mathrm{det}}\left(\varphi_2\right) + \mathrm{O}_{\mathrm{RLS}}\left(\varphi_2\right) \\ &+ 2\left(\cos\left(\frac{-2\varphi_0+\varphi_1}{2}\right) + \cos\left(\frac{-2\varphi_0+\varphi}{2}\right)\right) \\ &\cdot \left(x_{\mathrm{I}}\left(\varphi_1\right)\sin\frac{\varphi_1}{2} + y_{\mathrm{I}}\left(\varphi_1\right)\cos\frac{\varphi_1}{2}\right) \\ &- \cos\frac{\varphi_2}{10}\left(x_{\mathrm{S}}\left(\frac{\varphi_2+2\varphi_1}{2}\right)\sin\left(\frac{\varphi_2+2\varphi_1}{10}\right)\right) \\ &+ \cos\frac{\varphi_2}{10}\left(y_{\mathrm{S}}\left(\frac{\varphi_2+2\varphi_1}{2}\right)\cos\left(\frac{\varphi_2+2\varphi_1}{10}\right)\right)\end{aligned} \tag{2.16}$$

For a perfectly aligned IFP setup (Scenario No.1, alignment status T1), the SCS is shifted laterally by $\Delta z_{OS} \approx -26\,\mu\text{m}$ to introduce linear TTL to compensate for the effects of parasitic hinge deformations as calculated for the load case and hinge dynamics of the SCS [28].

The expected system behavior in terms of OPD is shown in Figure 2.7. Scanning both mechanisms continuously in mode one (BS) does not allow differentiation between telescope TTL and IFPM TTL. All three scan modi show the same behavior on a macroscopic scale, but zooming into the curves reveals that the microscopic behavior depends on the scan mode (see Figure 2.7b): Removing the steps and stitching them together allows for the reconstruction of the contributions of IFPM and SCS and telescope (labeled RC, for details refer to the caption of Fig.2.7).

2.5 Definitions of the interferometric phase

Heterodyne IFOs within the LISA context typically use QPDs as detectors, which consist of four segments and allow, in addition to measurements of longitudinal displacements, to detect changes in the relative angle of measurement to the reference beam. The superposition of the electric fields on the detector results in modulated photocurrents that can be combined in different ways to retrieve the relative phase Φ. The beat of the two electrical fields C can be described by the integral of the product of two analytical fields, the complex conjunct of the electric field of the reference beam E_r^* and the electric field of the measurement beam E_m, over the detector surface area (also see [26]):

$$C \coloneqq \int E_r^* \cdot E_m \, dS = A \cdot e^{i\Phi}$$

In the case of a QPD, four complex-valued beat notes C_n result from four integrals. While numerous ways exist to define the interferometric phase, a couple of definitions have been used in the community regularly. [29] The reasoning behind investigations into the different definitions and their impact on the measurement is that some may offer benefits. The weighted arithmetic mean, for example, aims at minimizing phase noise by reducing the contribution of quadrants with lower signal and worse Signal-to-Noise-Ratio (SNR) to the total phase. As a consequence, this scheme is also more susceptible to jitter due to TTL (if no further corrections are applied) as well as introducing additional non-linearities as an undesired side product.

Simple arithmetic mean (AP)

The most intuitive definition of the interferometric phase is the simple arithmetic average.

$$\Phi_{AP} = \frac{\sum_{n=1}^{4} \Phi_n}{4} \tag{2.17}$$

LPF definition (LPF)

The LISA pathfinder definition could be considered closest to the case of a single-element diode, as only the signal from the slit is missing.

$$\Phi_{LPF} = \arg\left(\sum_{n=1}^{4} C_n\right) \tag{2.18}$$

Please note that the argument function arg shall directly yield the unwrapped phase here and in the following.

Weighted arithmetic mean (WAP)

The weighted arithmetic mean attempts to obtain reduced phase noise by weighing segments with lower signals to contribute less and vice versa. Expanding the LPF phase definition in its series representation shows that this definition is just a first-order approximation of the LPF definition.

$$\Phi_{WAP} = \frac{\sum_{n=1}^{4} |C_n| \cdot \Phi_n}{\sum_{n=1}^{4} |C_n|} \tag{2.19}$$

Weighted LPF (WLPF and WLPF2)

Weighing the complex beat notes by normalizing them before adding the complex values and determining the phase yields another definition similar to the simple arithmetic mean (WLPF):

$$\Phi_{WLPF} = \arg\left(\sum_{n=1}^{4} \frac{C_n}{|C_n|}\right) \tag{2.20}$$

To obtain a definition of the interferometric phase that is more sensitive to lateral offsets of an RX clip (or yields a steeper slope) in terms of TTL coupling, one can define a weighted LPF-like definition for the interferometric phase (WLPF2):

$$\Phi_{WLPF2} = \arg\left(\sum_{n=1}^{4} |C_n| \cdot C_n\right) \tag{2.21}$$

Chapter 3

Validation of the IFP concept

In this chapter, a breadboard of an advanced pointing concept for a LISA-like space-based gravitational wave observatory that enables an architecture with two bi-directional interferometric laser links per S/C referenced to a single active test mass is investigated: Critical performance parameters are experimentally probed, raising the credibility of the concept and providing crucial insights into the alignment procedure as well as key technologies for the LISA mission. Compared to the baseline concept, IFP eliminates the need for an optical backlink connecting two individual OBs and a massive flexing harness, significantly reducing the DFACS complexity and avoiding self-gravity effects due to large moving parts. A possible payload accommodation and mechanism design are shown in Fig.3.1. Measurements of the pointing jitter, a first demonstration of the active breathing angle compensation, data on the end-to-end TTL coupling over the entire LOS angle actuation range, as well as compensation of linear TTL using active apertures are highlights to be on the lookout for. Comparisons of experimental data with the semi-analytical model presented in the theory section underline that key effects have been understood and accounted for. For additonal, non-public information, refer to the project progress reports and the final report. [30–47]

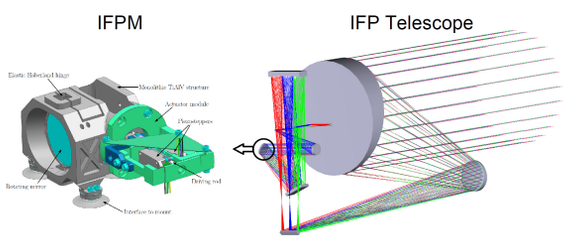

Figure 3.1: Left: CAD model of the IFPM mechanism for beam steering (Courtesy TNO). Right: Optical design of a possible IFP wide-field off-axis telescope; ray color indicates various pointing angles (Courtesy ADS).

3.1 Objectives

The main research objectives of the project 'Performance Verification of the In-Field Pointing for eLISA' can be summed up as follows:

- Experimental investigations of the critical performance-relevant aspects of the IFP concept
  1. Investigations of angular noise as well as of TTL effects of mechanisms and optics depending on the field angle and over the entire FOV
  2. Investigation of the thermal noise and coupling thereof
  3. Verification of active pointing
- Implementing a representative setup including a scaled-down telescope and a heterodyne IFO
- Design, manufacturing, and testing of an IFPM prototype

In the following, the experimental setup for obtaining the results to fulfill the research objectives stated above is detailled.

3.2 IFP setup

The experimental setup, like the baseline payload concept TP, uses pupil imaging to mitigate the effects of TTL coupling, which is crucial for obtaining the required path length noise levels. For IFP, the telescope is split into two stages: Here, a reflective and a refractive one, in between which the pointing mechanism can be placed in an intermediate pupil plane. It currently consists of six main components as well as numerous supporting systems and infrastructure elements serving the setup.

The six main components are (from left to right, shown in Figure 3.2):

1. A heterodyne IFO for optical readout of path lengths and optical angles using DWS by employing QPDs (also see Ref. [48]). As mentioned in the theory part, the photodiodes are the defining aperture and are imaged onto a planar mirror M0 - thus defining the pupil plane. The IFO also contains a refractive 1x pupil relay.

2. The Active Aperture Mechanism (AAM) is capable of laterally moving an aperture close to the location of a pupil plane, that clips the RX beam to introduce linear TTL for compensation of TTL due to misalignments.

3. A refractive five times magnifying BE, which images the pupil plane in the IFO onto the IFPM. The refractive stage nominally is operated at an FOV of zero, irrespective of the pointing mechanism angle.

4. The IFPM, designed by TNO, needs to be positioned in an intermediate pupil plane with its rotational axis coinciding with the mirror surface and centered in the pupil in case of an ideal alignment and no parasitic hinge motions.

5. The second magnifying stage is a reflective OAT with a magnification of five of the Korsch-type, that images the IFPM onto an external, real pupil plane, the M0 (mounted onto the Spacecraft Simulator (SCS)) is situated in. This situation is different from LISA, where the external pupil is a virtual one located behind the telescope and centered on the test mass, such that the entire optics become (at least in good approximation) invariant towards rotations about the test-mass center.

6. The SCS allows reenacting the motion of a distant space-craft and thus the constellation dynamics with only one setup by not only back-reflecting the transmitted beam, which consequently becomes the received beam but also by allowing the introduction of tilt in the constellation plane.

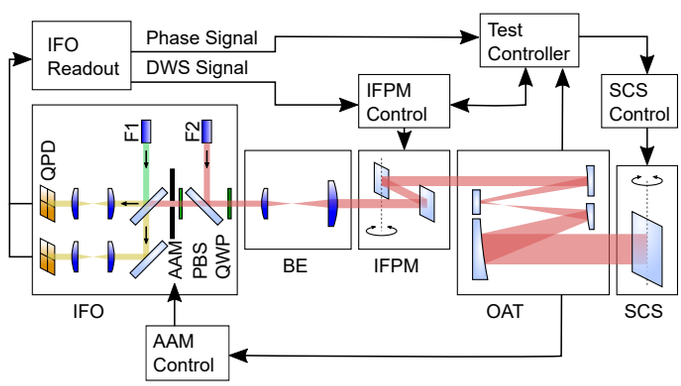

Figure 3.2: The layout of the setup: SCS: Distant Spacecraft Simulator, OAT: Off-axis Korsch-type wide FOV, low field curvature telescope 5x, IFPM: In-field Pointing Mechanism, BE: Beam expander 5x, IFO: interferometer, QWP: Quarter-Wave Plate, PBS: Polarizing Beam Splitter, AAM: Active Aperture Mechanism, QPD: Segemented quadrant photodetector, F1: FIOS local oscillator, F2: FIOS measurement beam. For details, see the text. Adapted from Ref. [14].

Critical infrastructure elements are:

1. The phase meter is used for the evaluation of the photodetector signals. This includes the front-end electronics with instrument amplifiers (there is still room for improvement, as was recently shown). [49]

2. Laser light infrastructure providing local oscillator and measurement laser signals. As well as actuators for stabilization of the laser frequency using a reference interferometer of unbalanced arm-lengths and the segmented photodetectors QPDR1+2 for feedback (piezo squeezing the non-planar ring oscillator's crystal and a thermoelectric controller manipulating its temperature, part of the Mephisto 500 NE laser), relative optical phase (fiber length stabilization, piezo-actuated mirror) using QPDPR1 to provide the feedback signal as well as DC and 1-f RIN stabilization (with PD1+2 as in-loop sensors) (see Fig.3.4).

3. Custom electronics developed within the scope of this thesis for driving the bimorph piezo actuators, used in SPM and IFPM, allowing for ultra-low noise operation out-of-loop and reduced control effort in-loop.

The most important auxiliary systems are listed below:

1. An active platform tilt stabilization system in addition to the passive pneumatic dampeners to level the platform at low frequencies, thus negating adverse effects of seismic noise (quasi-monolithic pendulum with capacitive read-out and pneumatic actuators driven by a modulated airflow generated using resonant electromechanical proportional valves).

2. A vacuum system (with slide valves and newly added dampening bellows as well as valves for venting): The bellow attenuates vibrations during the evacuation of the setup, the slide valve allows hermetically sealing the chamber to allow shutting down the pumps during performance measurements and the venting valves allow faster deceleration of the rotor of the turbomolecular pump, thereby limiting excess vibrations causing settling.

3. A multi-layer passive thermal shielding system to which a thick layer of Neopor foam for convective decoupling was added as additional insulation. An improved air conditioning system for enhanced active temperature control of the laboratory facilities was implemented.

The design choices in the implementation of the setup strive to enable the measurement of all driving noise terms (angular noise of the mechanisms and system, temperature noise at various locations of interest, laser frequency

noise...) as well as coupling factors (TTL, WFE, etc.).
To ensure representativity for LISA and show active pointing on the ground for the first time experimentally, ambitious requirements were imposed on the project and consequently on the setup. In the following, the noise shape function $u_n(f)$ denotes a relaxation towards low frequencies and is given by $u_n(f) = \left(1 + (2.8\,\mathrm{mHz}/f)^4\right)^{1/2}$ where f is the frequency:

Measurement band: 0.1 mHz to 1 Hz

The measurement band is relevant to the ability to characterize driving noise contributions. But linear coupling factors such as TTL may be characterized at higher frequencies to make use of higher stabilities. To show that the required levels of stability can be reached at the low-frequency end of the measurement band, the front-end electronics, phase meter, and control loops must be compatible with long-term stable operation.

Path length noise: $3\,\mathrm{pm}/\sqrt{\mathrm{Hz}} \cdot u_n(f)$

The allocation of coupling factors (such as TTL, system CTE, etc.) requires setting a path length stability. Here, the path length stability is chosen to be more demanding than current LISA requirements and is based on the thermoelastic effects and TTL contributions only. The test setup is not mechanically stable, relying on mounting by gravity, and also the laser is not stabilized to a frequency standard. Thus the setup is not intended nor expected to reach those levels of stability. Still, path length noise level down to $\approx 30\,\mathrm{pm}/\sqrt{\mathrm{Hz}}$ were reached for some frequencies, which is even more impressive considering that the setup is located on the first floor.

Angular noise: $4\,\mathrm{nrad}/\sqrt{\mathrm{Hz}} \cdot u_n(f)$

This angular noise contribution refers to the on-sky LOS jitter and the requirement for the IFPM mechanical angular noise requirement of $10\,\mathrm{nrad}/\sqrt{\mathrm{Hz}} \cdot u_n(f)$ was derived from this value (a factor of 5/2 due to magnification of the IFP telescope and the reflection off the plane pointing mirror). In the detector plane, an angular noise of $100\,\mathrm{nrad}/\sqrt{\mathrm{Hz}} \cdot u_n(f)$ is allowed accordingly (due to the total magnification of 25 of the telescope).

Temperature noise: $10\,\mu\mathrm{K}/\sqrt{\mathrm{Hz}} \cdot u_n(f)$

This requirement was based on the thermal noise levels reached by LPF in orbit and also requested for LISA. The IFP setup showed that such stability levels are achievable on the ground and require less effort than initially thought, as will be showcased by the data on the temperature sensor test bench (see Section 3.6.1, Appendix D).

3.2.1 Optical design

IFO The IFO is of the heterodyne type, the same architecture as will find application in LISA. However, the heterodyne frequency is chosen to be only around 10 kHz as we will not measure significant Doppler shifts compared to the phasemeters in LISA. This simplifies the design of the electronics and phasemeter significantly. Otherwise, many characteristics are shared between the IFP and LISA IFOs:

- Quasi-monolithic IFO design, all optics except waveplates and relay optics are bonded using OH catalysis bonding. [50]
- Polarization clean-up after FIOS using a PBS for both LO and measurement beams is done.
- Polarization routing of RX and TX beams is performed.
- Laser light injection is achieved utilizing fibers and fiber launchers for both LO and transmitted (measurement) beam (TX).
- Relay optics for imaging a pupil plane onto the detectors are integrated.
- A measurement IFO with two QPDs is used for DWS measurements and balanced detection using the beat of RX beam and LO (QPDM1/2, see Fig.3.4a).
- A reference IFO (QPDR1/2, see Fig.3.4a) with highly unbalanced armlengths, which detects the beat of LO and RX beam of the reference path over the Zerodur breadboard taking a similar path compared to the light in the measurement beam (in terms of distance and effective Zerodur CTE) is implemented. The reference IFO is used for the stabilization of the laser frequency.
- The unstable part of the IFO exposed to ambient conditions (fibers towards heterodyne frequency generation/ laser light infrastructure) is actively stabilized using a phase reference IFO (QPDPR1 and PDPR2) by beating LO and TX beams on the ultra-stable OB.

Telescope In earlier LISA studies, numerous IFP telescope designs were investigated concerning their suitability for LISA: The resulting trades arrived at an off-axis three-mirror near anastigmatic telescope of the Korsch type for the main telescope and a refractive BE for the second stage as the most attractive option for the IFP telescope. [24, 27, 51, 52] The final optics design is shown in Fig.3.4b and a CAD rendering of the setup excluding the refractive 1x relay stage on the OB and integrated SCS mechanism is shown

in Fig.3.3. In the table 3.1, some more details are given (and information regarding the TTL and pupil shifts was provided in the theory section): [1]

Requirement	**Value**	**Comment**
D_{external}	150 mm	Diameter ext. pupil; scaled-down for compactness.
D_{IFPM}	30 mm	Pupil diameter in the IFPM plane; see above.
D_{internal}	6 mm	Internal pupil diameter.
λ	1064 nm	Wavelength Nd-YAG, as in LISA.
$\varphi_{y\text{OS}}$	$\pm$18 mrad	Typical FOV covering LISA orbits.
$dO_{\text{pd}}/d\varphi$	2 mm	TTL allocation derived from path length and angular stabilities.
WFE	$\lambda/20$	For minimizing far field TTL
Polarization	circular	For polarization routing of RX and TX light, differs from LISA

Table 3.1: Important telescope specifications.

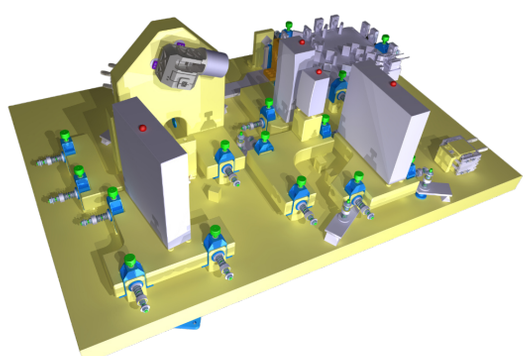

Figure 3.3: Rendering of the setup after integration of the 5x refractive BE but before integration of SCS and 1x refractive relay stages on the IFO OB. The yellow structural parts as well as the reflective optics and the IFO OB are made from the ultra-low-thermal-expansion glass ceramic material Zerodur. LISA Technology Package (LTP) heritage is used in the shape of the glued-in invar inserts of the adjustable mounts: Zerodur blocks are pressed against Zerodur and held in place using friction only.

[1] The exact mirror and placement information is included in the files stored at ADS (raytracing v4)

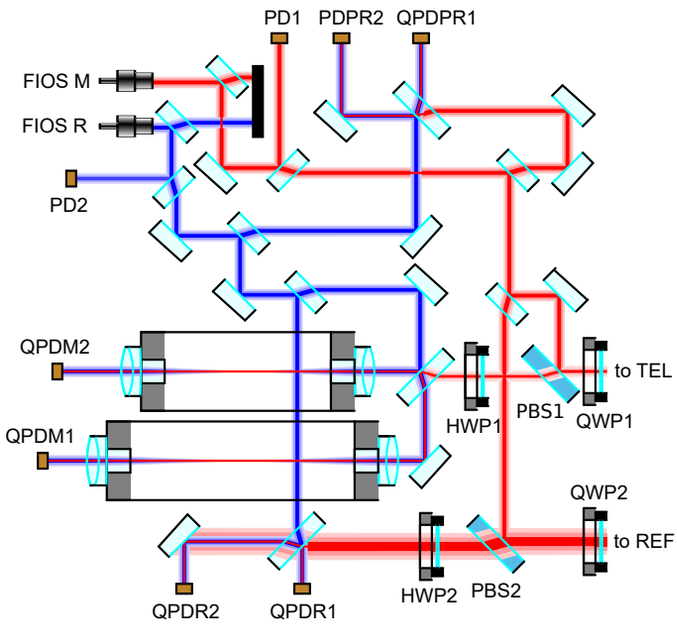

(a)

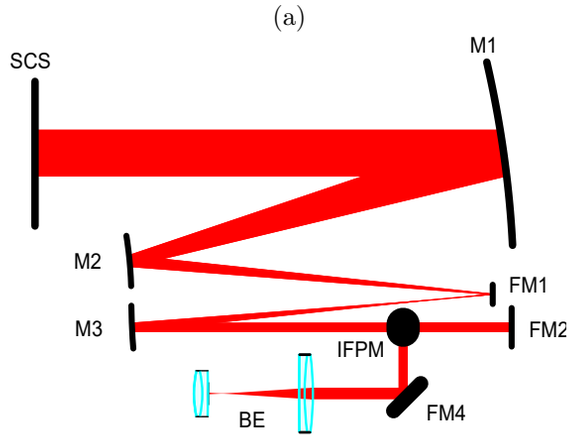

(b)

Figure 3.4: a) Layout of the IFP heterodyne IFO OB in OptoCAD. FIOS: Fiber Injector Optical Subassembly, PD: Photodiode, PDPR: PD Phase Reference, QPDPR: QPD Phase Reference, QPDR: QPD Reference, QPDM: Quadrant PhotoDiode Measurement, QPDR: Quadrant PhotoDiode Reference, HWP: HalfWavePlate, PBS, beamsplitters, mirrors, and 1x refractive relay stages are not labeled. b) Actuated back-reflecting mirror and telescope comprised of off-axis Korsch and refractive telescope stage: SCS: Space Craft Simulator, M1-3: curved mirrors, FM1-4: Folding Mirrors, IFPM: In-Field Pointing Mechanism (covering FM3), BE: 5x refractive beam expander.

3.3 Completion of the integration and alignment

Here, we discuss the alignment of the IFPM, BE, and relay optics as well as the detector and the procedure of replacing the static M0 mirror with the modified SCS mechanism for large FOV TLL and active breathing angle compensation measurements. The reflective telescope, static M0, and IFO have been aligned by using a laser tracker (LT), two theodolites, a hexapod-mounted wavefront sensor (Shack-Hartman Sensor (SHS)), matrix detectors, and the IFO itself. Documents [30–41, 53] include details regarding the design and alignment of the reflective optics.

The complete alignment procedure can be summed up as follows:

- Initial placement of the reflective optics using LTs and theodolites
- Fine placement using SHS wavefront measurements
- Placement and alignment of the IFPM using LTs, theodolites, and TTL measurements for fine positioning.
- Integration and alignment of the refractive stage using WFE measurements, a matrix detector, and the IFO itself as well as a ruler for rough alignment. TTL measurements were performed for fine alignment as well as additional WFE measurements to verify that the WFE was not compromised.
- Integration of the refractive pupil relay on the IFO OB. This was done using a matrix detector as well as a WFE sensor.

3.3.1 IFPM

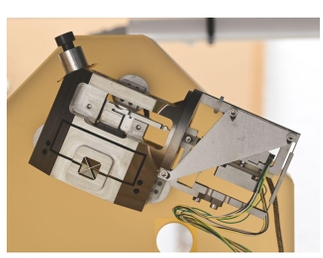

Figure 3.5: Photo of the IFPM post alignment.

Placement of the IFPM was done using a laser tracker and theodolite to check orientation and position (The silver mirror (lower center) and the laser tracker target nest (top left) were used for fine positioning, see Fig.3.5.). Manual placement and first adjustments using the micrometer screws of the Zerodur mounts were performed in advance for course positioning using the LT and theodolites. Further fine positioning steps using the micrometer screws were performed using DWS to maintain the angular alignment and angular scans to obtain the longitudinal and lateral displacements and hence the deviation of the nominal position from TTL measurements under both ambient and vacuum conditions (see Fig.3.6a and section 2.2). Ideal values would be zero lateral offset and a longitudinal pupil offset of the detector plane to the intermediate

pupil plane the IFPM mechanical pivot is situated in of approximately 1.21 m (which also takes into account the OPD due to travel through refractive and transmissive optics such as beam splitters). The final values obtained are (in the following lateral pupil offsets are specified in the IFPM plane and longitudinal ones such that they give the distance from the detector to the closest (intermediate) pupil):

Parameter	**Value**	**Error** (3σ)
lateral pupil offset	59.9 µm	±3.2 µm
longitudinal pupil offset	1.21 m	±0.04 m
WFE ($\lambda = 1064$ nm)	0.032λ RMS	0.005λ RMS

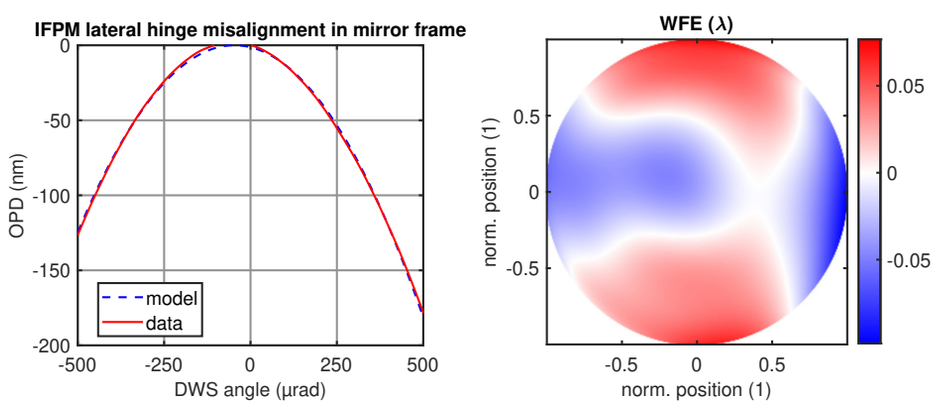

(a) (b)

Figure 3.6: a) TTL measurement: OPD vs. optical angle, as average over many data sets and both scan directions to cancel out systematic errors (red) compared to the semi-analytical model with lateral and longitudinal misalignments fitted to the experimental data (blue). b) Combined WFE of the reflective stage and IFPM mirror.

Therefore, longitudinal alignment is in excellent agreement with the ideal value within error margins, while lateral placement could still be optimized; resulting in a shift of the extreme value of the parabole towards a DWS angle of zero. Using the 180 thread-per-inch screws of the Zerodur base, the IFPM is bolted to; we could systematically achieve values better than ≈ 14 µm or even down to the measurement accuracy when going for small random, alternating changes. This would require turning the screw back and forth and performing measurements until one by chance obtains a value better than that we obtained above. It should be noted that here, the limitation is not given by the resolution in actuation using the finely threaded screws but rather the fact that built-up tensions in the mounts are released after fastening the bolt that pretensions the spring ensuring that contact

pressure is sufficient to allow for friction to keep the mount position stable and retraction of the fine thread screw.

3.3.2 Refractive 5x stage

Alignment of the BE was performed as follows: The BE was pre-aligned outside of the IFP setup using wavefront sensing in a double pass configuration and optimizing for a minimal WFE (piston and tilt were not included here). Next, a flip mirror was placed between FM4 and IFPM such that the DWS signal was unchanged. The mirror used is the same as the one used as a reference during pre-alignment, special attention is paid to the mirror orientation and alignment, such that the WFE is sampled over the same sub-aperture. This allows for measurements of BE alone and both BE and Korsch OAT later on under the same field angle. Due to spatial constraints, both measurement QPDs had to be unmounted, and instead, a beamsplitter was placed at the rough location of QPDM2. At the transmission output, a matrix detector capable of centroiding was placed to track and maintain the lateral beam displacement. The other port was used for WFE measurements by coupling light of the SHS into the setup, using two pinholes, and a power meter as well as a flip mirror referenced to the DWS signal earlier for tilt alignment.

This setup allows for placing the BE while maintaining the lateral beam position in the detector plane with a precision better than two microns, an angle of the returning wavefront better than 10 µrad while also fine-tuning the WFE first of the BE alone and technically also allows to perform fine-tuning of the combined WFE. Longitudinal placement is less alignment-critical and performed using a metal ruler. Fine-tuning of the WFE would require either removing (due to limited access to the locking and alignment screws) the BE and, for example, rotating the lenses of the BE followed by another pre-alignment and repeating the steps from the first BE alignment iteration or misaligning the BE such that at least the tilt in the nominally fixed axis of the IFPM is unaltered. If this is done, the IFPM must be used to correct in-plane tilt. Both strategies would be driving the effort quite a bit and are only to be considered if the performance can not be reached otherwise. Within the scope of this activity, it was decided, that such measures can be evaluated by analysis later on, if desired. Once completed, the secondary support equipment is removed, and the interferometric readout is restored. Angular scans performed by introducing tilt using the IFPM again yield TTL measurements a model can be fitted to; allowing for the extracting of longitudinal (detector to intermediate pupil now relayed to a location on the IFO optical bench) and lateral offsets (scaled to a corresponding offset in the intermediate pupil plane, the IFPM is situated in (approximately)). As before, a shifted parabole results, indicating a slightly imperfect and, yet, incomplete pupil

imaging onto the detector (see Fig.3.7a).

Parameter	**Value**	**Error** (3σ)
lateral pupil offset	52.7 µm	±29.8 µm
longitudinal pupil offset	220 mm	±8 mm
WFE ($\lambda = 1064$ nm)	0.028λ RMS	0.006λ RMS

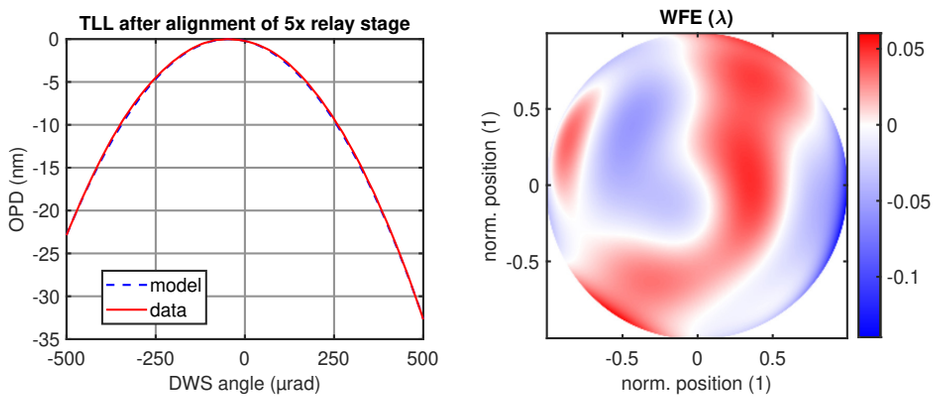

(a) (b)

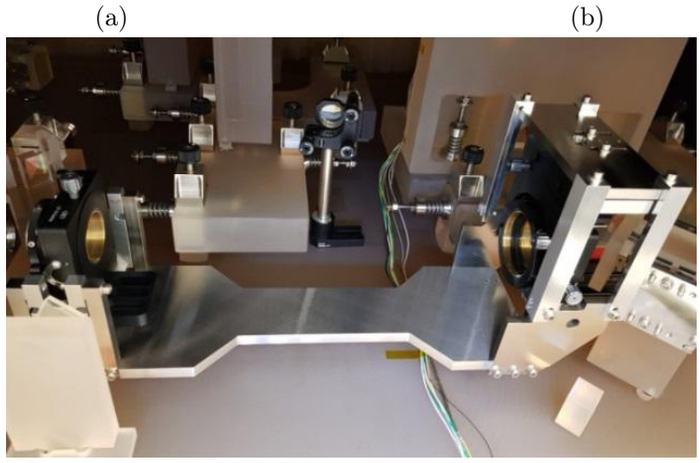

(c)

Figure 3.7: a) TTL measurement: OPD vs. optical angle, as average over many data sets and both scan directions to cancel out systematic errors (red) compared to the semi-analytical model with lateral and longitudinal misalignments fitted to the experimental data (blue). b) WFE of the refractive stage. For details, refer to the text. c) Photo of the 5x refractive BE: Visible are the two lens mounts with 5 adjustable degrees of freedom each, the central Invar strut connecting the two lens mounts as well as the thermal compensation scheme applied to keep the lenses stable in their height over the Zerodur breadboard.

A larger number of measurements can be taken to reduce the error of the measurement, as the fit values for the lateral misalignment exhibited a Gaussian distribution for scan in a direction, such that the error scales with the inverse of the square root of the number of measurements performed. Scans from positive to negative angles and vice versa were centered around different values, as slow drifts caused systematic errors, that can be corrected for by averaging over the two scan directions. Limiting is the drift of the optomechanics holding the BE-lenses upon locking using screws, as settling effects cause drifts in the order of up to several 10 µm (for the Newport LP-2A lens mounts, data not shown, deduced from comparison of measurements right after locking and a couple of days later; such drifts were not present before integration of the lens mounts).

3.3.3 Refractive 1x relay stage

The same procedure is applied for the most part as earlier. Only a pre-alignment is not possible due to the lenses being mounted separately. Further complicating matters is the lack of adjustable degrees of freedom. Merely one lateral degree of freedom is continuously adjustable by tapping against the mount. The z-axis (lens optical axis height over IFO OB) relies on shimming. Clocking and nick can not be adjusted continuously and yaw only by tapping against the mount. However, as both the reference and measurement beam are affected in the same way by the 1x relay, the impact of a slight misalignment is not expected to contribute much. Surprisingly, the WFE assumes a value that is as good as that of the reference used ($\approx \frac{1}{50}\lambda$). The final lateral misalignment in z is near perfect due to a stroke of luck as the shims (aluminum foil from the local supermarket) had a thickness of 13 µm when 12.5 µm shims were required (data not shown).

Figure 3.8: Photo of the 1x refractive pupil relay stage right after shimming with aluminum foil and gluing.

Parameter	**Value**	**Error** (3σ)
lateral pupil offset	24.3 µm	±0.7 µm
longitudinal pupil offset	−0.52 mm	±0.53 mm
WFE ($\lambda = 1064$ nm)	0.012λ RMS	0.011λ RMS

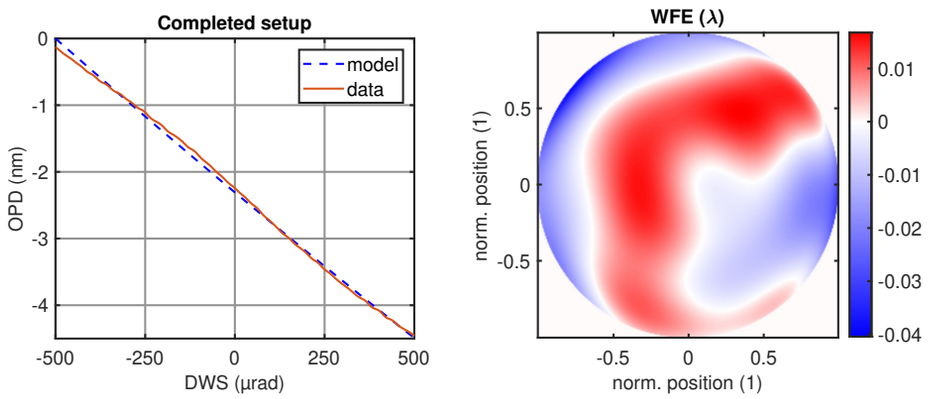

(a) (b)

Figure 3.9: a) TTL measurement: OPD vs. optical angle, as average over many data sets and both scan directions to cancel out systematic errors (red) compared to the semi-analytical model with lateral and longitudinal misalignments fitted to the experimental data (blue). b) WFE of the refractive relay stage.

3.3.4 QPD

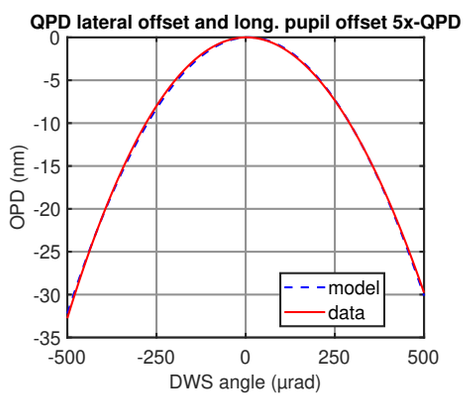

Figure 3.10: a) TTL measurement: OPD vs. optical angle, as average over many data sets and both scan directions (red) compared to the semi-analytical model with lateral and longitudinal misalignments fitted to the experimental data (blue).

The alignment of at least one of the QPDs in paths containing two QPDs for balanced detection is, in general, done by characterizing the gain of the amplifiers connected to the 4 segments by injecting an electronic test signal or an optical one to obtain correction factors for each quadrant. Next, the detector is laterally placed such that the Gaußian LO beam generates equal signal levels on the calibrated segments. In case angular scans are performed, while one 1x relay is still not integrated, a highly differential TTL measurement allowing for a very precise determination of relative longitudinal and lateral offsets of both detectors is enabled. The placement of the QPDs in such cases is limited by the calibration or lack thereof. Without systematic errors due to a lack of calibration data, the statistical error (three times the standard deviation of the mean) is roughly

40 nm. This precision is beyond the capability of typical optomechanics and manual alignment. Of course, one could again attempt to reposition the QPD until one gets lucky or improve the opto-mechanics design further in future implementations.

Parameter	**Value**	**Error** (3σ)
differential lat. pupil offset	11.19 µm	±0.04 µm
differential long. pupil offset	249.25 mm	±0.09 mm

3.3.5 SCS

Alignment Integration and Testing (AIT) of the SCS was performed after retrofitting with an LT40 bimorph piezo drive of the walking leg type and an encoder of the type Mercury II 6000V as well as a rotary optical grating ruler for optical readout. The SCS was aligned using a laser tracker, a theodolite as a redundant measurement for angular alignment of nick and yaw, and dial gauge measurements to determine the clocking of the mirror. Due to the fact, that the laser tracker nests were screwed in and removed after initial alignment, the laser tracker targets had to be placed again, limiting the overall achievable precision in the placement of the SCS. Longitudinal pupil offsets were detected by monitoring lateral beam wandering on a paper screen placed on the M0 mirror. Drifts were caused by a relaxation of the zerodur mounts, initially prohibiting large FOV measurements, as the resulting clocking of about 4 mrad resulted in contrast degradation at larger field angles. The final shift of the external pupil and clocking values of the M0 mirror are given in the following table:

Figure 3.11: SCS after integration and before adding temperature sensors.

Parameter	**Value**	**Error**
longitudinal positional offset (x_{OB})	±0.84 mm	$(\pm[0.44, 1.67] + 0.2)$ mm
lateral positional offset (z_{OB})	26 µm	±50 µm (2σ)
clocking	60 µrad	±40 µrad

3.4 Compensation of linear TTL by active apertures

By either laterally shifting the beam in the detector plane or lateral translation of a clipping aperture stop, additional linear TTL can be introduced intentionally to compensate for misalignments. These concepts are referred to as Beam Alignment Mechanism (BAM) or AAM. Here, the concept of active apertures is investigated further, as the compact nature of the clipping aperture allows for easy integration into the preexisting setup. First, we simulate the experiment and then compare simulation and experiment. The simulated scenario is as follows: Two Gaussian beams are imaged onto a QPD with the same dimensions and slit width as in the experiment. The beat of these beams and the phase resulting are computed using the different definitions of the interferometric phase introduced in section 2.5 of the theory chapter. In the case of a scenario including a clipping aperture, the aperture is placed in the RX beam, and the TTL is computed for different lateral shifts of the aperture. All simulations were performed in Matlab. Beam parameters were experimentally measured. Parameters for the simulation are given in the table A.2.

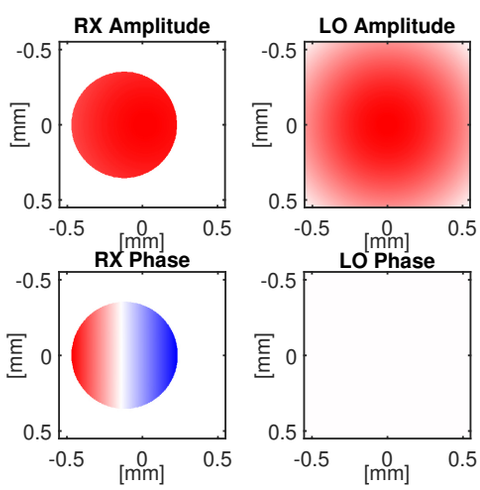

Figure 3.12: Beam amplitudes of clipped and tilted RX beam and LO beam, as well as corresponding phases, are inputs for the simulation.

Diffraction effects were ignored, as those are assumed to be mitigated by pupil imaging. A typical simulated scenario is shown in Fig.3.12: The RX-beam is clipped with a circular aperture that is laterally shifted. Parameters for the simulation are detailed in Table A.2. The RX beam is tilted, while the LO beam is static and, ideally, not tilted. Varying the angle of the RX beam about its pivot while leaving the lateral shift of the clipping aperture unaltered and repeating this process for different lateral positions results in the added TTL for each position. The linear TTL on the OB level versus the position of the clipping aperture can be seen in Fig.3.13 for our four definitions of the interferometric phase. The sensitivity of the DWS used for interferometric measurement of the angle of incoming relative to the

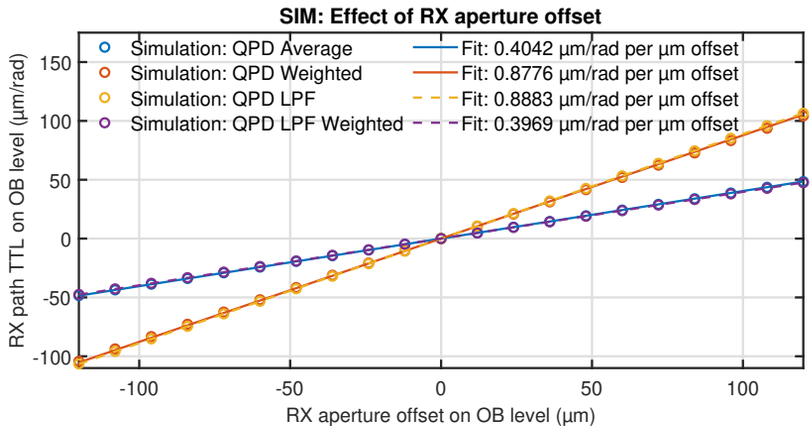

(a)

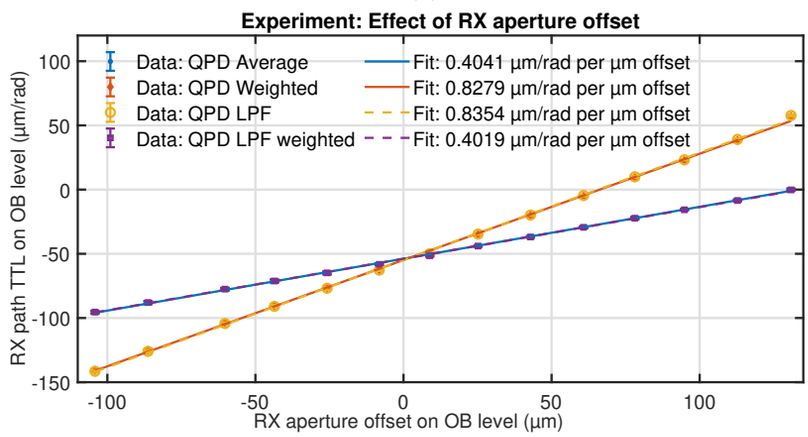

(b)

Figure 3.13: a) Simulation of linear TTL introduced by shifting an aperture clipping the RX beam for various definitions of the interferometric phase. b) Experimental data on linear TTL introduced by shifting an aperture clipping the RX beam for various definitions of the interferometric phase. Error bars are three times the standard deviation of the mean.

reference beam has to be calibrated at the very least when changing the diameter of the RX clip, as it depends on the RX clip diameter.

In case of a misaligned setup (corresponding to an offset in linear TTL in the simplest of cases), the shift in RX aperture position required to compensate will depend on the definition of the interferometric phase that one chooses for implementation in the phasemeter.

In general, it also may not be beneficial to zero or fully compensate linear TTL because an offset in lateral clip position also leads to reduced contrast and, thus, increased phase noise. Also, once the clip stops overlapping with the detector, the TTL and RX aperture offset relationship becomes in-

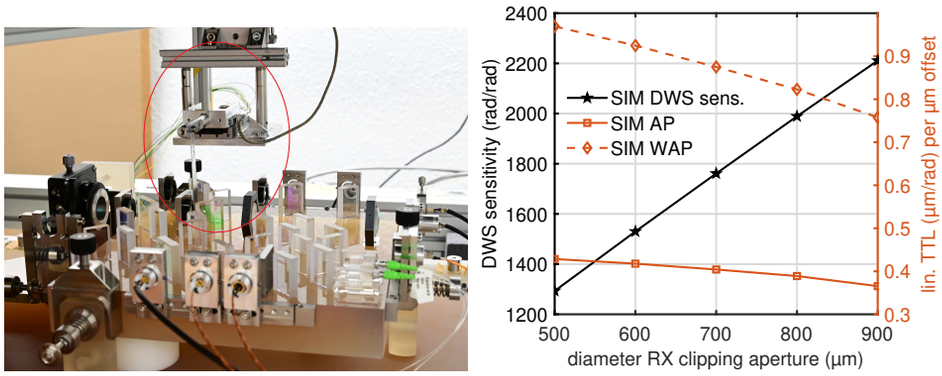

(a) (b)

Figure 3.14: a) Photo of the quasi-monolithic heterodyne IFO after completed AIT, including AAM (red ellipse); b) Effect of the diameter of the RX clipping aperture on DWS sensitivity and on added linear TTL per lateral clip offset in a simulation of the setup.

creasingly non-linear. Simulations furthermore show that smaller apertures yield slightly higher change in linear TTL when varying the lateral position. However, as expected, this also reduces the amount of signal available and changes the DWS sensitivity; corresponding data is shown in Fig.3.14b.

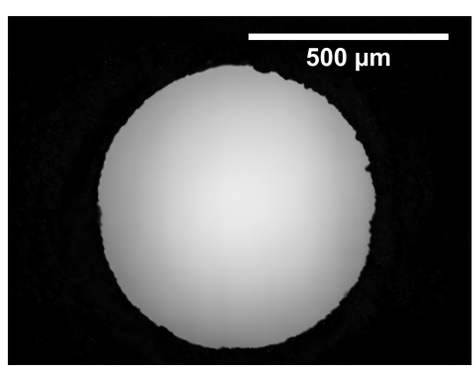

Figure 3.15: Microscope image of the aperture machined by laser cutting and subsequent removal of excess material at the cut by irradiation at lower fluence.

Upon calibrating for the new DWS sensitivities when adding a clip in the RX beam, several tens of scans in tilt were performed while recording the mixed beat signals for each position of the RX aperture. Each data point shown is the average over the linear TTL obtained from roughly 60-70 single scans; the error bars correspond to three times the standard deviation of the mean. The experimental data nicely matches the simulation results regarding linear TTL coupling introduced per increment in a positional shift of the RX aperture clip. Also, the existence of misalignments yielding additional linear TTL highlights that the position of zero linear TTL depends on the choice of the definition of the interferometric phase. In case of a 700 µm RX aperture and a 1mm detector diameter, it is only possible to move the

aperture less than 150 µm before the relationship between TTL added and aperture shift becomes increasingly nonlinear. Usage of an aperture larger in diameter than the QPD results in no change in TTL as long as there is no overlap of clip and detector surface, as one would expect (data not shown here, tested with a 2.2 mm circular aperture).

In conclusion, the introduction of additional linear TTL using a clipping aperture positioned in the measurement beam and in (or close to) an intermediate pupil plane was experimentally and numerically confirmed. Smaller aperture diameters result in slightly more added linear TTL per aperture position offset increment and reduced signal levels. Adding an aperture requires recalibration of the differential wavefront sensing sensitivity, such as introducing a known tilt using a scanning mirror equipped with capacitive sensing. While translations of that aperture can be used to compensate residual linear TTL originating elsewhere in the experiment (pointing mechanisms, lens or mirror misalignments,...), the offset of the clipping aperture required depends on the choice of the definition of the interferometric phase used. Further investigations into the ideal placement of that clip should include the reduction of interferometric contrast and be based on a maximization of SNR respective minimization of phase noise. As two of the definitions of the interferometric phase are approximations of the other two for small phase angles and the differences regarding linear TTL are primarily due to numerical errors, usage of only the definitions AP and LPF is recommended.

3.5 Key TTL measurements

So far, linear and quadratic TTL around small nominal pointing angles have been measured as part of the alignment process. Now, we investigate the impact of the WFE on the TTL due to LOS jitter and off-pointing on the phase noise in the signal received by the distant satellite as well as how the TTL changes with the field angle over the FOV covering the pointing range. The telescope design with its low WFE and wide FOV with optimized, low Petzval field curvature, aims to minimize both contributions. However, the alignment to obtain the desired properties represents a challenge due to very tight tolerances.

3.5.1 Far-Field TTL

The WFE for various field angles from $-1°$ to $1°$ was determined using a SHS and setting the field angle by tilting the SCS and compensating with the IFPM such that the TX and back-reflected RX light are colinear and counter-propagating. The WFE after decomposition into Zernicke polynomials can be seen in Fig.3.16 (at least the lowest 36 Zernicke polynomials in ISO indices notation were included in fits to the experimental data). The data is transformed into a far-field phase by the Kirchhof integral using Fraunhofer approximation. Similar calculations for the Rayleigh-Sommerfeld approximation can be found in reference [54]. The far-field intensity and phase for a FOV of $0°$ as well as the resulting far-field TTL plotted versus the pointing angles Φ and η of the emitting S/C are shown in Figure 3.17. Additionally, the WFE for both a FOV of $-1°$ and a FOV $1°$ are shown.

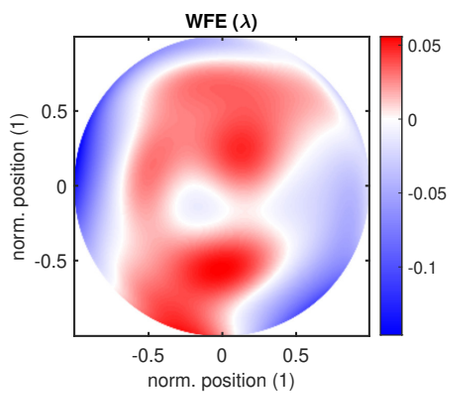

Figure 3.16: The WFE of the IFP telescope at a FOV of $0°$ assumes a value of $0.0346\,\lambda$ RMS.

Within a field of regard of 500 nrad, the resulting maximum TTL coupling factor (geometric sum of both contributors, assuming no correlation between in- and out-of-plane angles with a proper implementation of DFACS) of less than 1 mm is slightly below the allocation (which is based on the assumption that a pointing jitter below $10\,\mathrm{nrad}/\sqrt{\mathrm{Hz}} \cdot u_n(f)$ is feasible).

The far-field TTL coupling was calculated for a telescope with a 150 mm radius assuming the same WFE can be obtained for a larger aperture as well; thus justifying the imaging of the phase map onto a larger pupil. The results obtained for the different field angles are summed up in the table below in terms of maximum TTL coupling within the fields of regard specified above:

FOV	$\mathbf{C}_\phi$	$\mathbf{C}_\eta$	$\mathbf{C}_{\mathbf{total}}$	**WFE (RMS)**
$-1°$	0.649 mm	0.209 mm	0.682 mm	$0.0458\,\lambda$
$0°$	0.464 mm	0.151 mm	0.488 mm	$0.0346\,\lambda$
$1°$	0.729 mm	0.335 mm	0.802 mm	$0.0455\,\lambda$

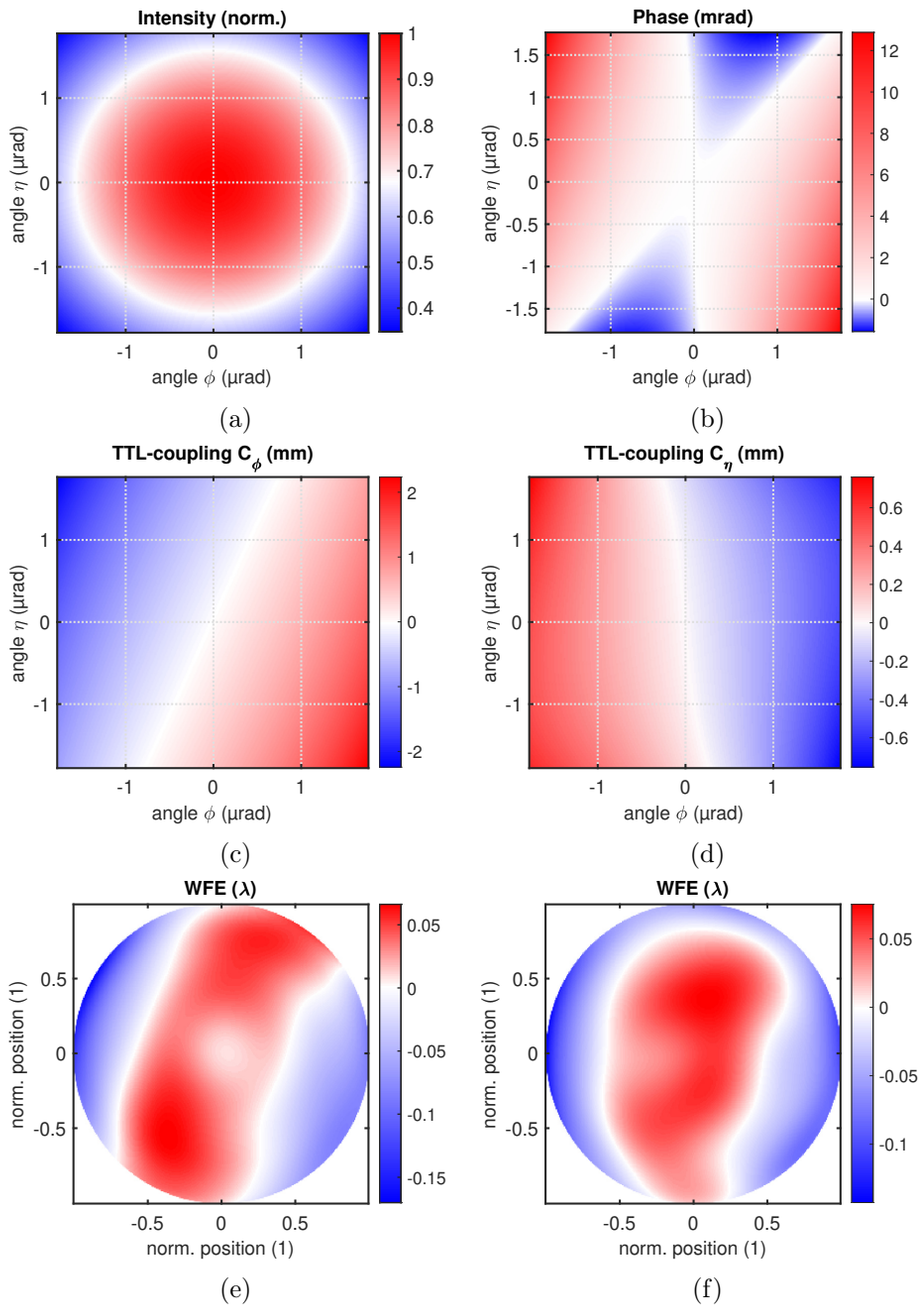

Figure 3.17: Far-field intensity (a), phase (b), and TTL coupling factors (the angle derivative of far-field optical phase, as calculated from the WFE, decomposed into Zernickes): c) for angle ϕ and d) for angle η for 0° e) The WFE of the IFP telescope for a field angle of 1° assumes a value of 0.0455 λ RMS and for a field angle of −1°, a WFE of 0.0458 λ RMS is measured (f).

3.5.2 End-to-end system TTL

The piston introduced by scanning over the FOV of the telescope and that of the active pointing mirror compensating the angle introduced must be either kept small enough not to contribute or well characterized, such that a correction in post-processing of the data can be performed.

Active compensation of excess TTL is also feasible by setting the AAM or BAM to compensate for the local slope in OPD by adding a linear OPD contribution with the opposite sign as part of housekeeping could also be an option (at least provided that the BAM or AAM settles quickly enough to avoid transient gaps in low-noise data acquisition and features sufficient resolution and range).

During AIT, the linear TTL of IFPM and refractive stages was determined already by measurements around small field angles close to zero, as well as quadratic contributions from longitudinal displacements of the pivot points from the detector plane. Below, the OPD caused by the telescope, pointing mechanism and SCS are shown. The measurement beam probes the setup twice, as it is back-reflected from the planar mirror of the SCS. The peculiarities of this double-pass configuration and how the angular magnification is impacted for the various measurements are discussed in the theory section covering the semi-analytic model of the setup. For a perfectly aligned telescope and mechanisms not suffering from parasitic hinge deformations, the nonlinear OPD is given by the yellow curve in Figure 3.18a.

However, we expect at least further contributions of the same order of magnitude due to the parasitic hinge deformations discussed in the theory section. Additional contributions due to the telescope's imperfect alignment are also to be expected, particularly as the telescope mirror M3 is known to be misaligned in terms of clocking. When continuously actuating the SCS to scan over the entire FOV, and compensating with the IFPM, the contributions of the telescope and mechanisms are indistinguishable. From such a measurement alone, it is unclear if a deviation from the model can be explained by a different deformation behavior of the hinge or a misalignment of the reflective telescope. As an example, additional contributions of the IFPM are ruled out by performing a stepping motion with it and scanning the SCS around various field angles. Each data point represents an average over many measurements: Without the parasitic motion of the IFPM hinge contributing, the data trend is still modeled well using the same misalignments of the telescope (see Fig.3.18b). Consequently, the IFPM is not causing the additional TTL observed in the experiment. To experimentally verify that the SCS does not exhibit an unexpected parasitic hinge deformation yielding the additional piston observed, a separate (pre-) characterization of the SCS with respect to non-linear TTL at large field angles should be performed.

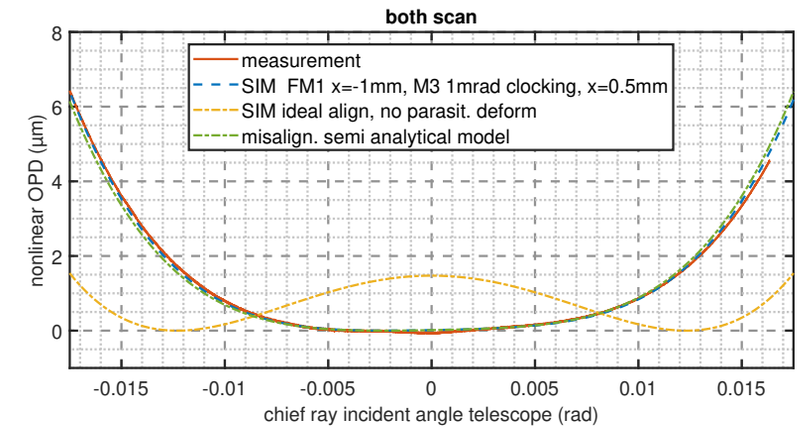

(a)

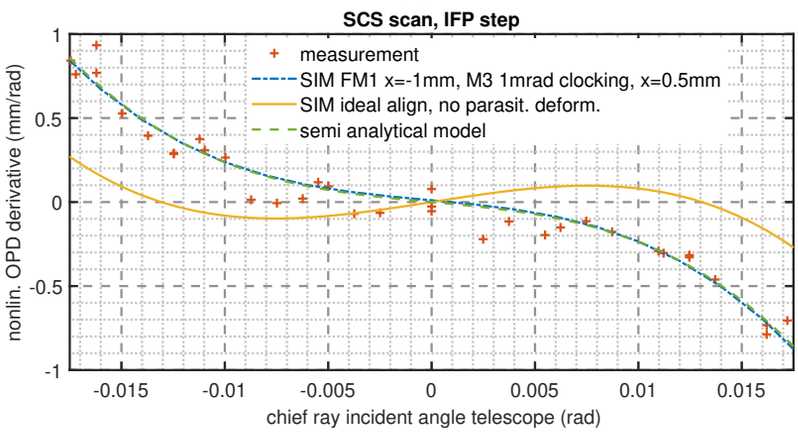

(b)

Figure 3.18: a) Nonlinear OPD in double pass caused by TTL coupling when performing a continuous scan with SCS and compensating with IFPM compared with various scenarios (see the legend, text); b) Scanning motion of SCS and step-stare motion of IFPM (correspond to a single pass, as the derivative removes static contributions) around various field angles shows that the IFPM is not causing the additional quadratic TTL observed in the experiment (offsets due to the linear TTL of 3.2 mm have been subtracted).

Due to hysteresis in path length caused by the IFPM (discussed later on in section 4.6), the lock-in measurement used previously can not find application in this instance when using scans of the IFPM and a stepping motion of the SCS to characterize the integrated IFPM directly: It relies on a linear detector response as well as on a response of the hinge in terms of hysteresis in path length that is sufficiently small and ideally independent of the field angle around which the scan is performed. The second condition is not fulfilled, and therefore the alternative is scanning around larger angles

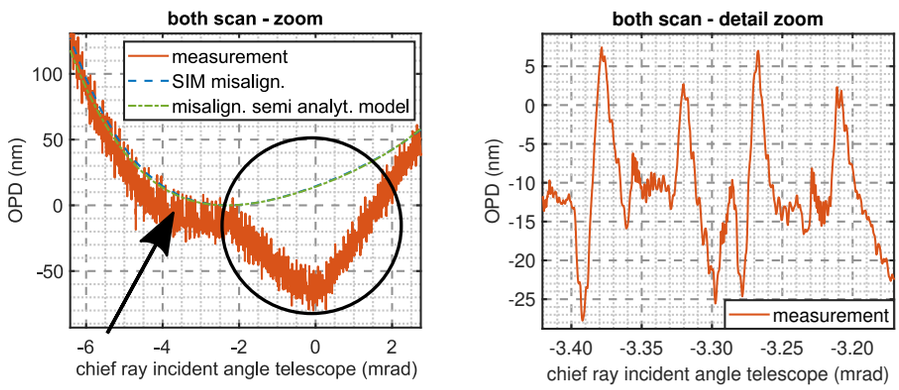

(a) (b)

Figure 3.19: a) A zoom into Figure 3.18a shows effects not included in the models: Encircled is a local deviation due to a nonlinearity in the IFPM mechanism (bistable behavior) and an arrow points out the spikes in OPD, which result from the non-linear behavior of the bimorph drive using only a single iteration of the optimization procedure presented later on rather than random path length noise in the measurement. b) Detail zoom into the data showing the spikes due to actuator nonlinearity.

such that the hysteresis effects are only affecting the measurements at angles where the DWS is nonlinear and using interferometric data only from intervals, where the angle of the incoming wavefront is less than 0.5 mrad. However, this scheme is less effective in discriminating noise. It requires more scans and larger scan amplitudes, which limits the measurements and does not allow for meaningful measurements, as the scattering due to drifts is substantial. In the future, an improved mechanism design will strive to avoid hysteresis in path length and mechanical angle, so these effects do not adversely affect critical measurements. Assuming, the SCS globally does behave according to the FEM simulation and does not exhibit unexpected behavior, a possible misalignment explaining the results from both scan modes shown as well as the WFE obtained in addition to being coherent with the fact, that a clocking of M3 was recorded during AIT of the reflective telescope would be a combined displacement of FM1 ($\delta x_{OB} = -1\,\mathrm{mm}$) and M3 ($\delta x_{OB} = 0.5\,\mathrm{mm}$ and $\vartheta = 1\,\mathrm{mrad}$ clocking (around an axis parallel to x_{OB} at the location intersects with the M3 mirror)).

A zoom into Fig.3.18a shows effects not included in the models (see Fig.3.19): Encircled is a local deviation due to an additional nonlinearity in the IFPM mechanism and an arrow points out the recurring spikes in OPD, which result from the non-linear behavior of the bimorph drive using only a single iteration of the optimization procedure presented later on rather than random path length noise in the measurement (also see detail zoom, figure 3.19b.

3.6 Environmental noise contributions

Avoiding excess noise due to the coupling of temperature fluctuations, seismic noise, acoustics, or other disturbances to the observed variable is critical to the success of the experiments presented: Especially low-frequency measurements often suffer from noise scaling proportionally with the inverse of a power of the frequency of at least one or greater: Such as flicker noise (f^{-1}) or thermal noise (typically f^{-2}). Besides using DC- and 1-f-RIN stabilization and implementing a phase-locked loop (to compensate for effects such as CTE and acoustics in unstable heterodyne generation infrastructure outside the thermally stable vacuum environment of the IFP chamber) as well as a frequency lock by locking the phase of the highly unbalanced reference IFO to an electric reference signal, also the temperature of the lab was actively stabilized and the platform tilt noise of the chamber actively controlled.

3.6.1 Thermal noise

The temperature fluctuations present in the lab are attenuated in the ultra-stable part of the IFP setup (situated in a vacuum chamber) as well as in the laser infrastructure (heterodyne frequency generation using passive means in conjunction with active control of the outer layer using a custom controller for the air conditioning unit in the optics labs). For the ultra-stable chamber, the following measures were implemented:

- An outer layer of Neopor foam for decoupling of the steel chamber from the airflow in the lab, thus eliminating convection.
- The chamber itself acts as a low pass due to its thermal inertia resulting from large capacitance, poor convective and conductive coupling to the environment, and allows for evacuation: Heat transfer towards inner layers is primarily radiative by design.
- MLI radiation barriers cover an anodized aluminum thermal shield that has high emissivity on the inside and acts as another lowpass poorly coupled to the outer layer, but well coupled to the inner layer to even out temperature gradients.
- Usage of all-Zerodur transfer functions and low linear CTE materials as well as thermal compensation of relevant degrees of freedom of metal structures wherever possible.
- Thermal diagnostics system, for evaluation of lab temperature and temperatures inside the setup at numerous locations. Sensor cables are taped to the chamber to avoid heat bridges.

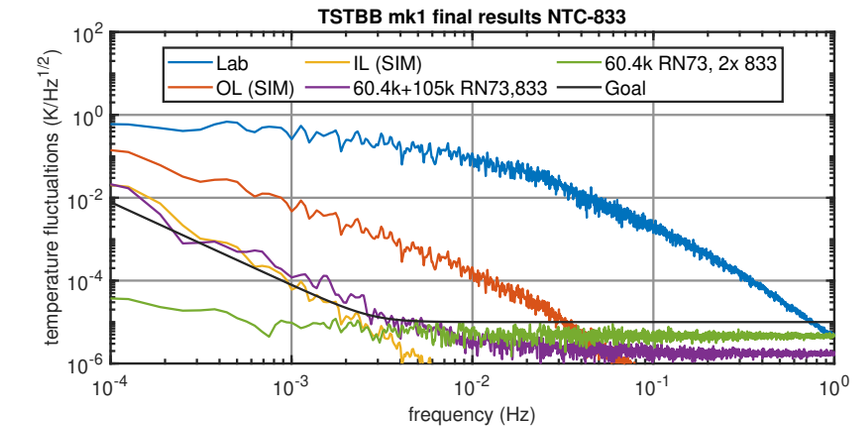

(a)

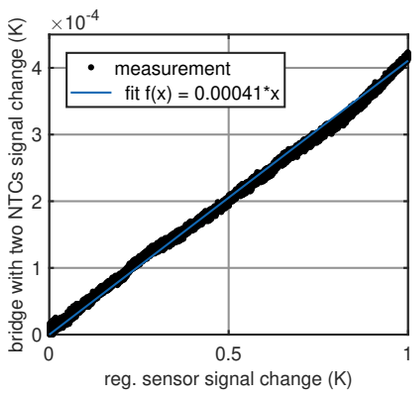

(b)

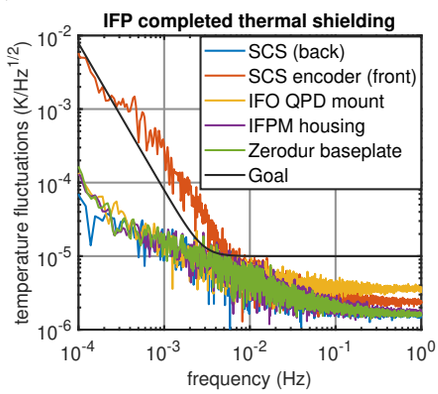

(c)

Figure 3.20: a) Thermal noise of the temperature sensor testing breadboard simulated for the inner layer (IL), and outer layer (OL) based on the logged data (Lab) as well as a sensor with two NTCs for common-mode suppression (green, 2x833) and standard sensor (purple, 833). b) Common-mode thermal noise suppression (linear coupling). c) Temperatures at various locations; only the encoder produces noise above the measurement noise floor.

The system CTE of the IFP setup is estimated to be the sum of the products of the lengths of each material in the path multiplied by their linear CTE (resulting in a conservative value of $\approx 1 \cdot 10^{-6}\,\mathrm{m\,K^{-1}}$). In case, the temperature fluctuations are below the level of $10\,\mu\mathrm{K}/\sqrt{\mathrm{Hz}}$, thermal expansion and changes in the refractive index of the transmissive optics would only contribute with less than $10\,\mathrm{pm}/\sqrt{\mathrm{Hz}}$. Figure 3.20 shows the simulated and achieved noise performance of a testbench built for the selection of low-noise components finding application in the sensors as well as the performance levels obtained for the final sensor configuration.

The setup for component selection was designed to allow for fast testing

of components independent from work on the main setup: The thermal noise performance is nearly as good as the target stability of the main setup, and equipping the Wheatstone bridges with two instead of one NTC of the same kind allows for further common mode suppression of thermal noise by more than three orders of magnitude (see Fig.3.20b). For high frequencies, the measurement noise is limited by Johnson noise, and for low frequencies, by the current noise of the components of the bridge (see the green curve, Fig.3.20a).

The thermal performance of the testbed and the simulation predictions are validated by measuring the thermal noise using a regular sensor with one NTC thermistor and three reference resistors and plugging into the simulation the ambient temperature fluctuations logged by another sensor (blue, Fig.3.20a): The purple curve representing the experimental data overlaps with the simulation (yellow) at low frequencies, whereas for high frequencies the electrical noise of the sensor is limiting (green curve). A dedicated noise model for the electronics exists, that could be combined with the thermal model to give predictions over the entire frequency range. In Figure 3.20c, the measured temperature fluctuations at various locations of the IFP setup are shown. Temperature noise immediately next to the

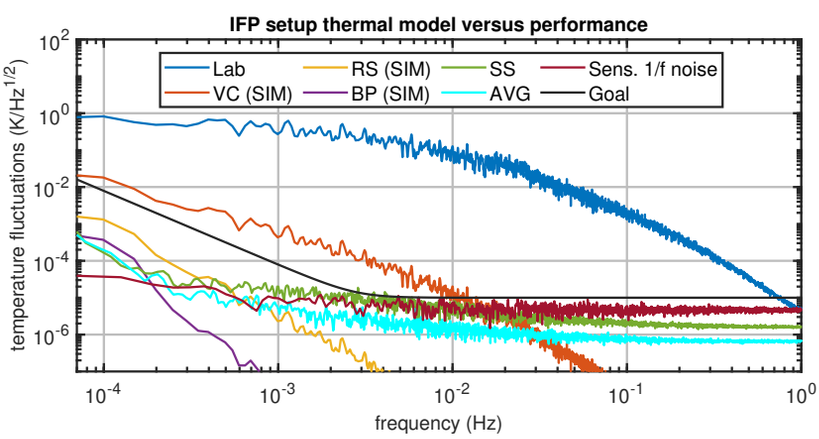

Figure 3.21: Thermal model of the IFP setup for dimensioning the thickness of the Neopor and data measured: RS: Radiation Shield, BP: baseplate, VC: vacuum chamber, AVG: average all sensors, SS: single sensor. Simulations are indicated by (SIM).

optical encoder exceeds acceptable levels, while sensor noise dominates in other locations. The thermal model set up for the IFP setup in Matlab (see Figure 3.21) aided in dimensioning of the thickness of the Neopor insulation material. As a final note, the performance of the setup is better than predicted by the simulation, as the geometry was simplified and assumptions were conservative to ensure performance levels are reached. Measurements of sensors connected to the chamber itself showed noise levels compatible

with the requirement (not shown).

3.6.2 Seismic noise

Besides the availability of real estate for a 2.5 Gm baseline antenna, seismic noise in the low-frequency range is the reason why the LISA experiment is going to be performed in space and presents a challenge when using a setup that makes use of large optics mounted by gravity using isostatic mounts based on three Zerodur spheres and pads with form fits shaped as hollow cone, wedge and solid plane to define all degrees of freedom.

Seismic noise can act upon the setup through lateral acceleration, angular acceleration, and quasi-static tilt in conjunction with gravity.

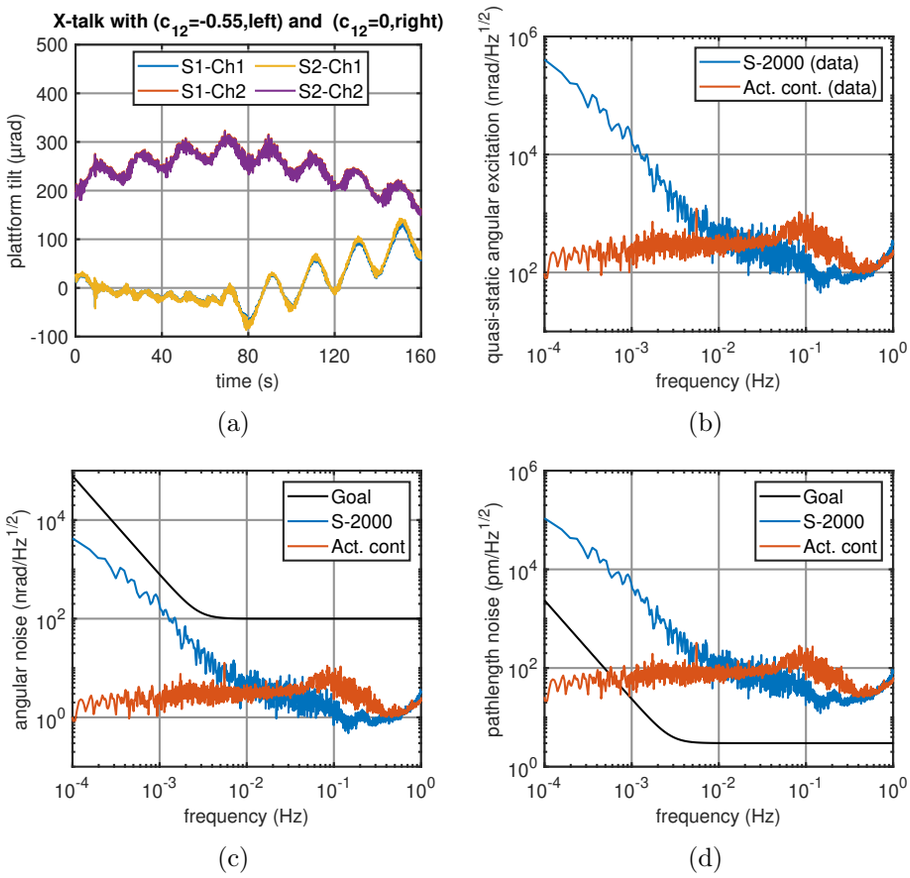

Figure 3.22: The effects of passive and active platform tilt stabilization: a) Resonse in open loop with and without orthogonalization of the DOFs in tilt. b) Quasi-static angular excitation as measured using the two-channel tiltmeter. c) Angular noise due to the quasistatic excitation. d) Path length noise due to quasi-static angular noise excitation.

For a mirror mounted on three Zerodur spheres using the isostatic

mounting concept applied here, one can show that the component tilt noise due to seismic activity $\Delta\varphi$ is proportional to:

$$\Delta\varphi \propto \left(\frac{I}{Mg}\ddot{\eta}^2 - h_0\left(\frac{\ddot{x}^2}{g} + \eta\right)\right)$$

where I is the moment of inertia, M the mass of the mirror, g the acceleration due to earth's gravitational pull, η the angular motion of the platform the experiment is situated on due to the ground tilt induced by seismic activity, h_0 the height of the mirror and x the lateral motion of the ground in pointing direction (equal to $-x_{OB}$ in the raytracing coordinate system in the theory section). For low frequencies below 10 mHz, the largest contributor (by several orders of magnitude) couples via the induced platform tilt noise according to this simple structural model: Tilt acceleration is suppressed with the fourth power of the frequency and also by a factor of nearly ≈ 100 due to the scenario dependent prefactor; Contributions due to acceleration noise resulting from the lateral motion with an Amplitude Spectral Density (ASD) of typically less than $1\,\mu\mathrm{m}/\sqrt{\mathrm{Hz}}$ can also be neglected. [55] The present model uses the mirror geometry, placement of the Zerodur spheres, and material parameters as inputs and relies on the assumption that the spheres can be described as Hertzian contacts. Measuring the tilt noise of the platform and either actively controlling it or logging the data and removing the effects of platform tilt in post-processing are both valid options to be considered. The first option was pursued, as it has the benefit of not relying on post-processing the data, which can be quite complex and prone to errors.

The tilt of the platform is measured in two axes using a quasi-monolithic spring pendulum read out via capacitive sensing. As actuators, the pneumatic dampeners from Newport of type S-2000 are used (in addition to providing acoustic isolation): After retrofitting electromechanical proportional valves and introducing a controlled leak by adding manual needle precision valves and high precision pressure regulators to ensure a very controlled leakage flow that can be either over- or under-compensated, the platform can be either lifted or lowered. Two legs retrofitted this way, acting together, can level the platform with nanoradian resolution. Later on, ultra-thin lifting cushions were used, as the volume flow needed for actuation can be reduced and thus delay in the response, improving the performance further by increasing the control bandwidth. Figure 3.22a shows a critical step in improving system performance: The determination of the inverse crosscoupling matrix to orthogonalize the system response and reduce the control effort. For measurement times after 70 s, one tilt axis (Ch2) is performing an open loop sine motion, and due to crosscoupling, the nominally un-actuated axis (Ch1) performs a motion as well. From the response recorded in several such experiments, a crosscoupling matrix was derived and inverted, such that open-loop actuation in one channel

does not couple into the other axis (in first order), which was successfully implemented (for times until 70 s, afterward the inverted crosscoupling matrix was replaced by a diagonal matrix). In Figure 3.22b, the in-loop tilt noise of the platform is shown with (red) and without (blue) active platform tilt leveling, as well as calculated estimates of the contribution to angular (c) and path length noise (d) in both instances, when taking into account only the motion of M0/SCS mirror center and mirror tilt as well as the magnification of the telescope. The projected pathlength noise contribution and noise shape in the passive case fit well with the results obtained by interferometric noise measurements and are very close in amplitude. The performance of the platform leveling system was confirmed using an out-of-loop sensor. Here, it was observed, that the out-of-loop signal noise levels never fell significantly below $0.1\,\mu\mathrm{rad}/\sqrt{\mathrm{Hz}}$. Plotting the response of the two sensors (of the same type) against each other after rotating the data such that the differential noise for both axes is minimized, showed that the nonlinearity of the sensors is the root cause limiting the performance to the levels mentioned before. In-loop and out-of-loop data for active and passive control (AC) are shown in Figure 3.23.

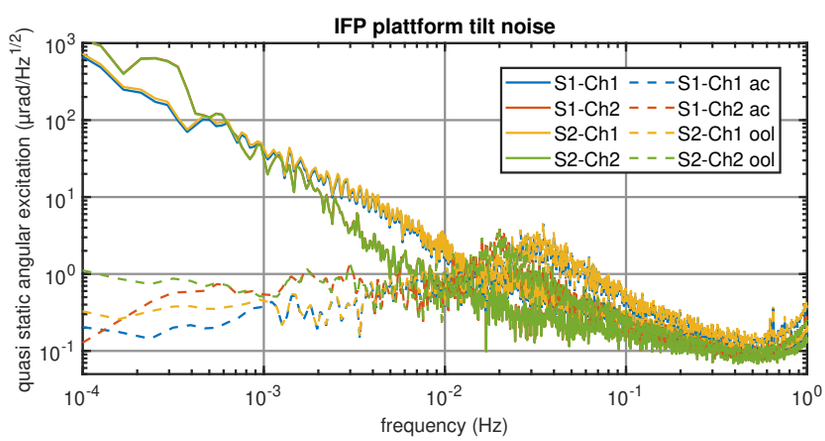

Figure 3.23: Passive stabilization with active mechanical coarse leveling (solid lines), and active mass flow control (dashed lines) using the signal from sensor S1 as feedback (ac) and sensor S2 to provide an out-of-loop measurement (ool): At low frequencies, tilt noise can be suppressed by several orders of magnitude.

3.7 Optical noise performance

First, the path length noise measurements and improvements to the IFP setup are presented. While the path length noise was never expected to be close to LISA requirements due to the limitations of the environment and

mounting concept, the continuous improvement in performance and further refinements in the future may allow for measurements limited by stray light performance only. The angular noise performance is critical to allow for validation of the active pointing. Special attention was paid when designing the setup, such that it is capable of meeting the requirements.

3.7.1 Path length noise

Initially, the laser infrastructure including heterodyne frequency generation via AOMs was situated outside the vacuum chamber under ambient conditions without any protection from thermal noise, air flows, and acoustic noise present in the laboratory. For this scenario, a typical measurement

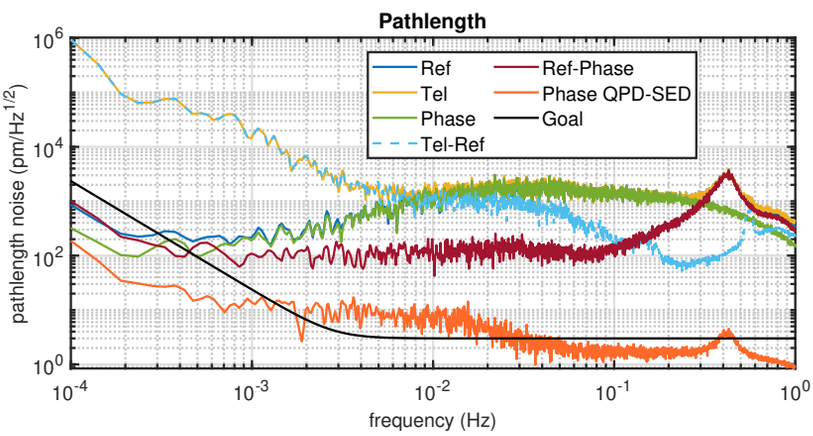

(a)

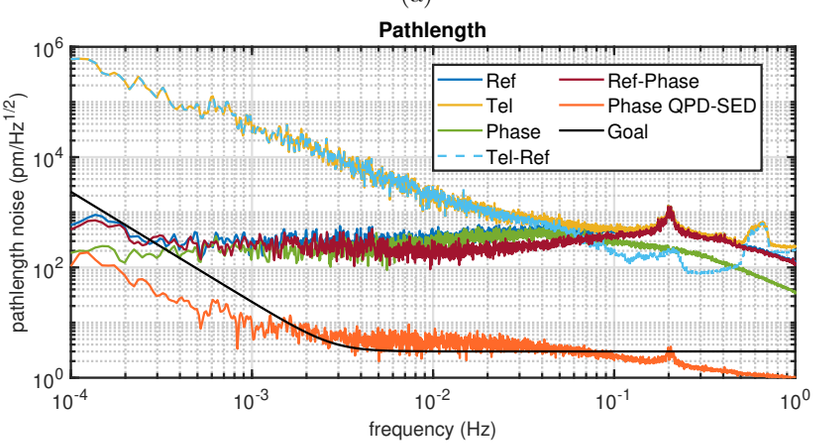

(b)

Figure 3.24: a) Initial noise performance is limited at mid frequencies by the performance of the PLL performance. b) Improvement of control loop parameters yielded a slight improvement and also revealed additional noise sources hidden under the noise floor so far.

is shown in Figure 3.24a: The noise of the phase reference is used as a feedback signal for the PLL (green), and the reference path is used as feedback for the FLL (blue). The difference of phase reference and reference (burgundy), which is an indicator for the laser frequency noise, the path length noise in the measurement path is plotted in yellow, the differential noise of measurement and reference path, which allows suppression of certain noise sources using common mode rejection in light blue as well as the differential noise of phase QPD and SED in orange to gauge the out-of-loop performance of the PLL, and the desired path length stability in black are shown.

After a first optimization of the control parameters (see Fig.3.24b), the residuum of the PLL and FLL are significantly improved, and the peak in the burgundy curve corresponding to the path length noise caused by residual laser frequency noise is identified to be caused by too high a gain of the FLL. Additionally, the peak at around 0.6 Hz in the measurement path (TEL, yellow) is now above the measurement noise floor and investigations showed that this peak is caused by CPU lags, as a software spectrometer implemented for debugging is using too large a share of available computational power. A revision of the software allowed for the elimination of this particular noise peak.

In a second optimization iteration (see Fig.3.25a), special care was taken to reduce the control effort of the PLL minimizing the relative phase noise between measurement and local oscillator beams: An enclosure was constructed around the optical infrastructure, as the reduction of ambient noise is expected to yield lower residuals in-loop without improving the gain of the control loops. The walls of that enclosure are made from aluminum sheet metal covered on the outside with a layer of several centimeters thick Neopor foam and painted on the inside with LabIR ultra-high emissivity paint to reduce thermal noise and gradients on the inside. Additionally, the optical fibers are clamped down onto the breadboard using soft foam, reducing both acoustic noise and thermal noise. These efforts yielded a further improvement of up to more than one order of magnitude concerning the performance of the PLL and up to more than two orders of magnitude for the FLL. Several resonance frequencies characteristic of the setup can be spotted in Fig.3.25a: The resonance of pneumatic dampeners of the optical table at 1.7 Hz, the mechanical resonances of reflective telescope optics from 30 to 100 Hz and difference frequencies of those resonances between from 5 Hz are visible. For frequencies above 5 Hz, some crosstalk between the telescope measurement path and the phase reference IFO is clearly visible. This crosstalk was identified to be caused by a stray light IFO and subsequently was reduced by a factor of roughly five using ND filters. A final iteration for reducing the ambient noise in the unstable part of the IFO included moving the AOM driver electronics to the outside of the enclosure as well as the introduction of thin aluminum sheet metal bend around the optics to form

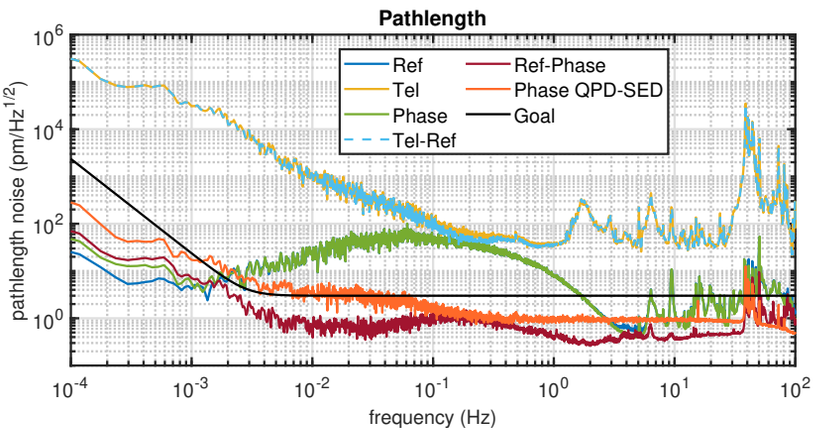

(a)

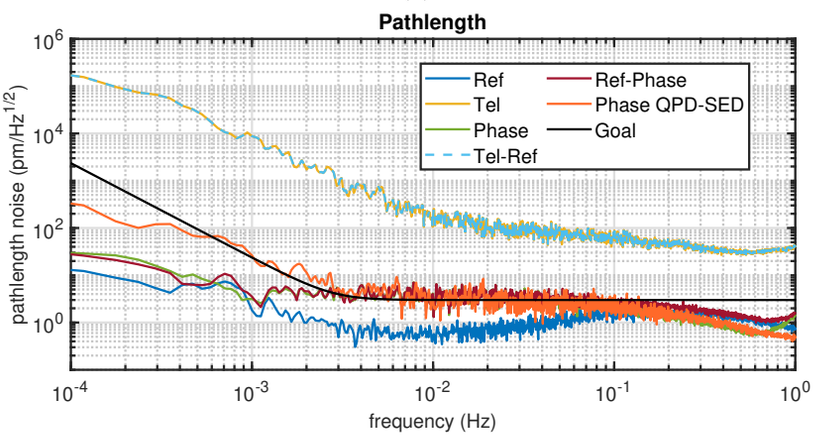

(b)

Figure 3.25: a) Further improvements in PLL and FLL performance and mirror resonances at higher frequencies. b) Final performance of the control loops without balanced detection and stabilization of the laser to either the cavity or iodine frequency standards.

compartments further restricted airflows and reduced thermal gradients as well as placing thin aluminum sheets covered in ultra-high emissivity paint on top of the bend sheets forming the compartment, allowing for a reduction in air volume available for convection and further reducing temperature gradients (see Fig.3.25b). This resulted in a further improvement of the PLL residual by more than one order of magnitude for mid-frequencies in the LMB.

While for some frequencies, a path length noise about $30\,\mathrm{pm}/\sqrt{\mathrm{Hz}}$ is reached, the path length noise is significantly higher than the requirement that was demanded for the allocation of coupling factors. However, it should be noted that the experiment was never expected to reach these values

nor is it required for the determination of the coupling factors as well as driving noise terms. As was discussed in section 3.6.2, the active seismic compensation was expected to result in a significant improvement, as the coupling of quasi-static platform tilt to path length noise is projected to be at levels about the same as the remaining path length noise observed in the experiment. However, a first measurement using the active seismic control scheme showed no significant improvement. This hints at laser frequency noise being a contributor of a similar magnitude as seismic noise, although the differential noise of the FLL and PLL indicates low residual frequency noise in the reference IFO, common mode suppression depends on the relative phase of measurement and reference paths and thus laser frequency noise in the measurement path may on average be not as well suppressed as the residual noise levels suggest. [56, 57] As the thermal noise is more than one order of magnitude below the requirement, it contributes according to the conservatively calculated system CTE with less than $1\,\mathrm{pm}/\sqrt{\mathrm{Hz}} \cdot u_n(f)$. This means, that thermal noise is not expected to be limiting, whereas laser frequency noise remains to be ruled out. One way to do so would be locking the IFP laser an external optical reference, e.g., an optical cavity or spectroscopy setup (Note the performance crossover observed for optical cavities and doppler free iodine spectroscopy!). [58, 59] Doing so while the seismic compensation is online and offline should allow to either verify the effectiveness of the seismic control and shed light on new limits imposed by other noise sources so far hidden in the noise floor. Additionally, balanced detection should be used in the FLL and PLL as well to reduce the impact of RIN noise. In this regard, a lower heterodyne frequency or a frequency generator with higher modulation output bandwidth and dynamics may be useful to reduce residuals further.

3.7.2 Angular noise

Angular noise was not much affected by any improvements to the unstable part of the IFOs, as the DWS signal is derived from a highly differential measurements, where most noise sources are efficiently suppressed by common mode rejection. Angular noise was scaled when adding the magnifying refractive stage as expected. Low-frequency noise is expected to be driven by seismic effects as well as thermal effects. Electronics noise from DWS read-out is expected to be limiting in case, active pointing using the IPFM is performed. In Figure 3.26 the angular noise recorded during the path length noise measurements presented in the previous subsection is shown for the reference IFO (blue), the phase reference IFO used for stabilization of the unstable part of the IFO (green), the measurement path (yellow), and the goal (black, depends on integration level). Discernible in Figure 3.26c is the crosstalk mentioned before from measurement path to phase reference IFO. On a final note, electronics noise contributes with

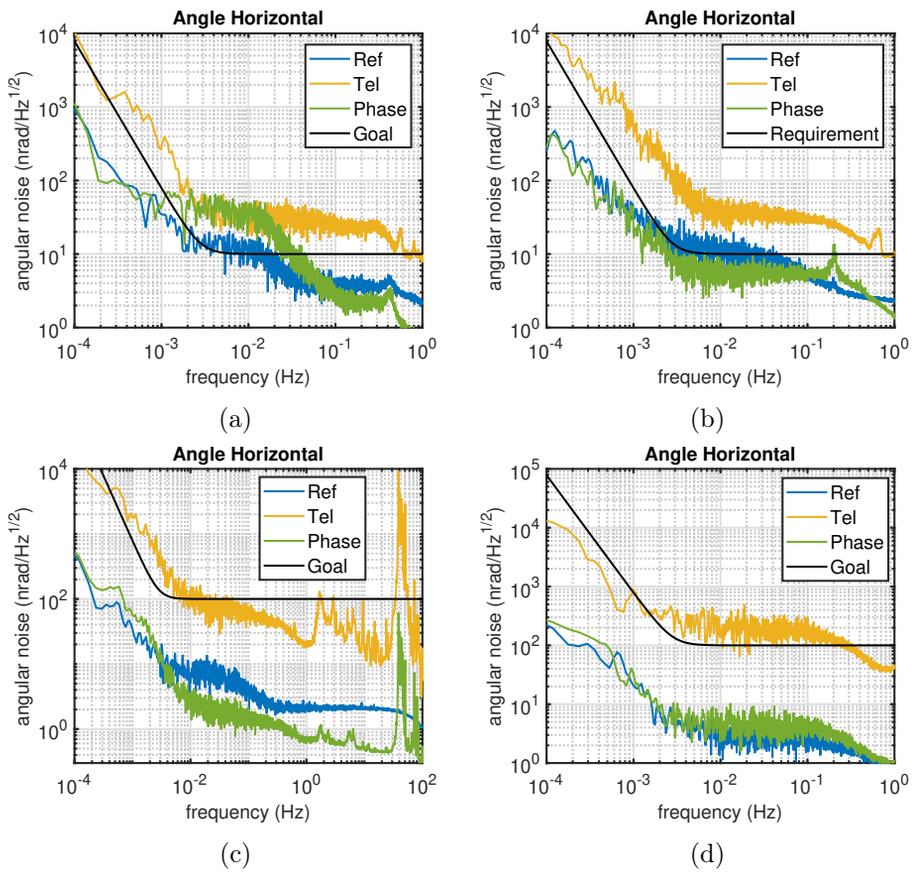

Figure 3.26: The angular noise of the in-plane (constellation) pointing angle corresponds to the path length noise measurements above. The noise is mostly affected by adding the magnifying refractive optics, as improvements in the control loops have little effect due to the high common mode rejection in DWS. The corresponding path length noise data, derived from the same measurements, is shown in the same order in figures 3.24a,3.24b,3.25a and 3.25b.

less than $1\,\mathrm{nrad}/\sqrt{\mathrm{Hz}}$ end-to-end, as was shown by blocking one beam and modulating the other beam in intensity to emulate a stable beat note using the arbitrary function generator part of the infrastructure for heterodyne frequency generation.

3.8 End-to-end demonstration of active pointing

The procedure for testing active on-sky-breathing angle compensation, or, simply, LOS pointing can be sketched out as follows:

- Tilting of the SCS at the largest angular rate predicted by orbital models to re-enact the orbital dynamics of the constellation.
- Measuring the tilt of the RX beam to LO using DWS yields a feedback signal, one can lock on.
- Addressing an actuator phase to the bimorph drive of the IFPM with a suitable control law and parameters, such that the tilt introduced by the SCS is compensated.
- Recording data to investigate the performance obtained.

In Figure 3.27a, the path length noise in the double pass is plotted for both active pointing (with a constant angular rate of $\approx 3.3\,\mathrm{nrad\,s^{-1}}$ on SCS/M0 level) and the static M0 case (without active pointing). In Figure 3.27b, the in-loop angular noise in the detector plane as determined by DWS is shown for the nominal pointing axis: The in-loop angular noise is on the same level as that of the Zerodur reference (and limited by electrical noise in the read-out chain of the FEE). In Figure 3.27c, the orthogonal axis is shown, which should not be affected by the active pointing: In fact, the stability appears to be slightly lower (likely due to cross-coupling), but still within the requirement. It should be noted, that a minor crosscoupling depending on the misalignment of the measurement QPD or the rotational axis of the IFPM is to be expected as well as due to parasitic tilt of the mechanisms for large strokes of the actuator. The noise of the nominally actuated axis (in-plane of the constellation) is of much higher interest: Where the requirement was slightly violated before, the noise floor during active pointing is well below the requirement over the entire measurement band. For most frequencies, the noise floor is situated even with a margin of a factor greater than one order of magnitude below the requirement. Comparing the noise floors for inactive and active pointing, the gain of the controller can be experimentally determined and is coherent with that of a PI controller. For the lowest frequencies, a suitable control law could yield improvements, but as the noise at low frequencies is dominated by electronic noise, the electronics would require further optimization to obtain a benefit from such measures. For the initial tests, which were already sufficient in terms of angular noise performance in-loop, no optimized waveforms were used. However, it was observed in the following tests, that the gain was highly dependent on the phase of the actuator: For certain phase offsets parameters had to be chosen, which resulted in unstable behavior arising within the duration of the measurement. The reason for this behavior is

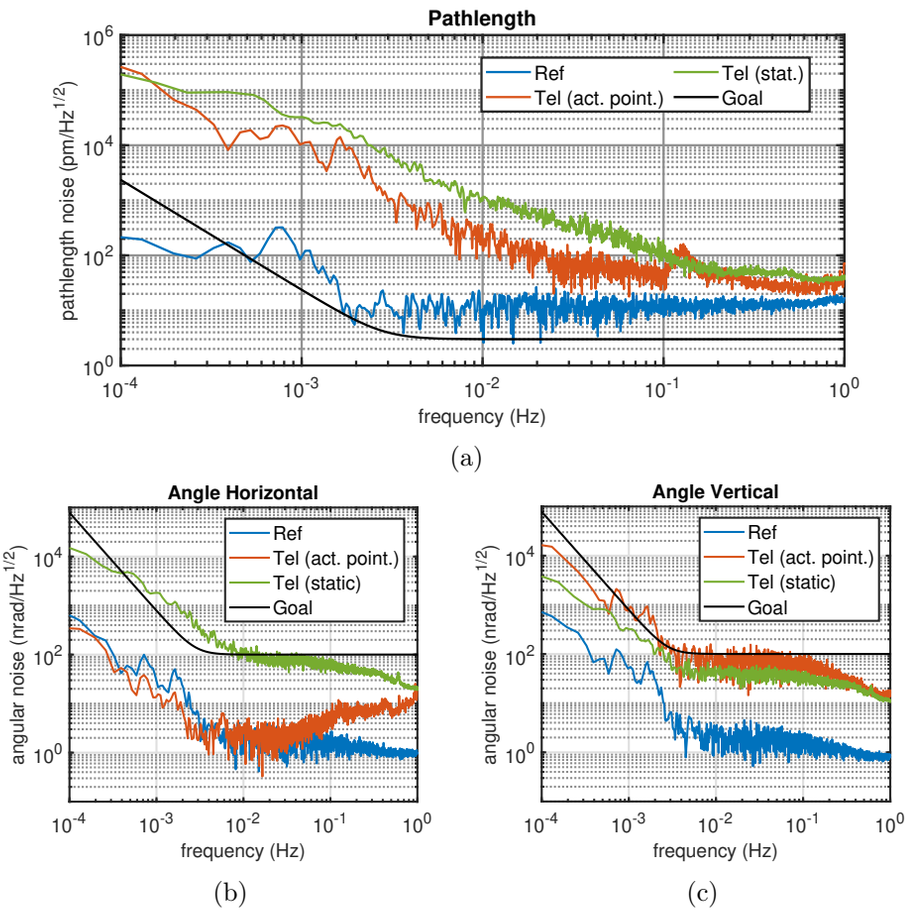

Figure 3.27: Effect of active pointing on path length noise (a) and angular stability of the actuated, 'soft' axis (b) and that of the nominally unactuated, 'hard' axis (c). Pointing occurs at a rate of $\approx 3.3\,\mathrm{nrad\,s^{-1}}$ on SCS level.

found to be the periodic nonlinearities intrinsic to actuators with internal periodic processes and is addressed in the upcoming section.

Based on the in-loop angular noise performance during the simulation of active pointing, and the previous measurements of TTL of the setup, the contribution of TTL to OPD jitter can be inferred (s. Table 3.8). The path length jitter resulting from TTL is in the order of $3\,\mathrm{pm}/\sqrt{\mathrm{Hz}} \cdot u_n(f)$, which corresponds to the total allocation for the setup. This is without using a BAM or AAM for further reduction of coupling factors, which would result in even lower TTL contributions to overall pathlength noise.

Contributor	**TTL** ($\mathrm{mm\,rad^{-1}}$)	**Ang. jitter** ($\mathrm{nrad}/\sqrt{\mathrm{Hz}}$)	**Summation**	**Comment**
FF-TTL in η (out-of-plane)	0.34	4	linear	-
TTL out-of-plane telescope (SIM)	0.18	4	linear	-
	OPD jitter ($\mathrm{pm}/\sqrt{\mathrm{Hz}}$)			
Total out-of-plane	**2.06**		**RSS**	-
	TTL ($\mathrm{mm\,rad^{-1}}$)			
FF-TTL in θ (in-plane)	0.73	1	linear	-
nonlin. TTL in-plane tel.	0.85	1	linear	-
linear TTL (in-plane)	0.66	1	linear	-
	OPD jitter ($\mathrm{pm}/\sqrt{\mathrm{Hz}}$)			
Total in-plane	**2.20**		**RSS**	-
Total OPD jitter	**3.04**			**wo BAM**

Table 3.2: Rough estimate of expected OPD jitter due to TTL measured and current best estimate of angular noise based on the measured pointing performance (in-loop). This is not considering (regular) usage of the BAM to compensate for excess coupling, resulting in even lower TTL.

The regular usage of the BAM is currently not foreseen. Residual TTL would still be present due to the error of in in-orbit coupling factor determination (or errors in the on-ground calibration as well as additional effects due to settling) as well as the beam displacement accuracy of the BAM (which will be better than 1 µm in the detector plane and capable of beam displacements larger than 100 µm, if the BAM performs as specified).

3.9 Periodic nonlinearities of bimorph actuators

In this section (which is available as pre-print, and will be published in an actuation journal, see Ref. [60]), an algorithm is discussed that eliminates the periodic non-linearity of a bimorph piezo actuator by modifying the phase of the voltage waveforms used for driving the actuator. The procedure presented here allows for separate optimization of the motion of the actuator groups to obtain the properties desired (such as a specific stepsize or maximum force) and is limited by measurement noise or manufacturing tolerances only. Performance improvements are not only obtained for open-loop operation but also closed-loop operation using DWS as feedback during nominal science operation. This is because near handovers of the ceramic rod between adjacent legs, the response of the actuator is decreased considerably, increasing the control effort. The linearized response resulting from the waveform optimization allows for the use of control parameters not depending on the actuator phase. All pointing architectures using actuators with internal periodic processes fulfilling the requirements stated further on in the text (such as non-resonant operation) will benefit from the optimization proceedure presented.

3.9.1 Background

While classic piezo actuators, made from a stack of piezoelectric crystals, allow for an actuation precision better than 1 nm, their total stroke is limited to a fraction of the stacks' dimensions. [61] Bimorph piezo drives on the other hand maintain the advantage of ultra-high precision positioning capabilities while being also able to perform strokes larger than the piezo stacks themselves. [62, 63] In the case of walking leg drives, this is because a rod is clamped down on and transported by one or more sets of two actuator groups (legs), thus allowing for a stroke that is equal to the length of the rod less the separation of the tips of the outer piezo legs. [64, 65] However, this operating principle requires a periodic motion that also yields an undesired periodic nonlinearity of the actuated variable. [66] While there are several types of these piezo drives commercially available that have a different design in detail (see Fig.3.28), they all intrinsically suffer from periodic nonlinearities: When unoptimized, symmetric voltage waveforms are used for driving the actuator, the hand over of the rod is performed

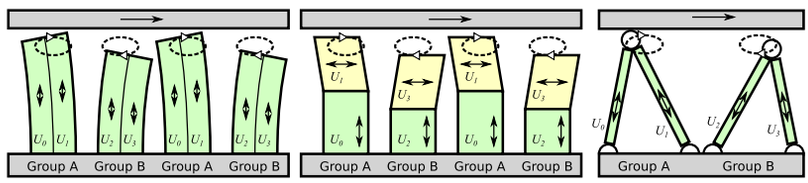

(a) (b) (c)

Figure 3.28: Typical geometries for piezo actuators of the bimorph type each featuring at least two groups consisting of two elements to each of which a voltage (U_0 to U_3) is applied. In a) the bending type is shown. Prominent examples are the Piezo LEGs by Piezomotor or the NEXACT by Physik Instrumente; b) shows the clamp-sheer type drive, an example would be the NEXLINE by Physik Instrumente; c) features the PICMAWalk developed by Physik Instrumente. The dashed ellipses represent example trajectories of the tip of the legs (Images: Courtesy A. Sell).

such that the legs at least partially hinder one another: The motion slows down during the hand-over. While a model based optimization of bimorph piezo drives is limited by the accuracy of the model, the method presented here is limited only by the accuracy and repeatability of the measurement device used during optimization. [67] The procedure yields in principle improvements for both open-loop and closed-loop operated systems, as in closed-loop operation the control effort is reduced due to a more linear response. [66, 68, 69] Furthermore, it can be applied to systems with several actuated degrees of freedom as long as the drives can be separately addressed and the resulting motion can be measured; the motion needs to have a slower dynamic than the lowest resonance frequency and the movement sequence must not change for typical speeds. E.g. inertia based friction drives can not be optimized using the presented method.

3.9.2 Principle of the optimization procedure

The input of an actuator, whose response is to be linearized, shall be a phase ϕ that takes into consideration the internal periodicity of the actuator. A phase value of 2π thus corresponds to one internal cycle (for example one revolution of a spindle or one step of a walking motion). The procedure presented here requires, that the actuated variable a (position, angle, etc.) can be measured as a function of that phase.
The general working principle of the method is as follows: The measured actuator position $a(\phi)$ is filtered such that a function $A(\phi)$ containing only the linear increase with ϕ (with a slope of $\frac{c_0}{2\pi}$) as well as harmonics of the fundamental frequency is left. By recording many actuator periods (typically more than 16) and filtering of harmonics, the procedure becomes thus resistant to measurement noise, but also requires that the measurement

device used (capacitive sensors, IFOs or optical encoders) during the initial optimization process has a much smaller (periodic) nonlinearity than the actuator to be optimized; or a different periodicity. By solving the equation $A(\psi) = \frac{c_0}{2\pi}\phi$, a function $\psi(\phi)$ that is periodic except for a linear slope can be determined. Using this function as input signal of the actuator instead, the actuator position now follows by design the function $A(\psi(\phi)) = \frac{c_0}{2\pi}\phi$, that is linear in its response to the new input. Therefore, all deterministic periodic perturbations are eliminated from the resulting motion (within the limits imposed by measurement accuracy and repeatability). In case of the internal processes suffering from hysteresis (e.g. when piezoelectric crystals are driven by voltage amplifiers), the procedure can be applied in an iterative fashion $\psi_1(\psi_2(...(\psi_n(\phi))))$.

Optimizing initial waveforms to yield a more linear response In order to obtain a linear response of a piezo friction drive, one should use a waveform that is derived using a model-based approach as a starting point for the optimization procedure discussed before. [67,70] In the simplest form (without hysteresis effects, for a beam of high aspect ratio and small deflections compared to the beams' dimensions), one can use a linear model based on Euler-Bernoulli beam theory in order to describe the two dimensional trajectory of the tip of a single leg depending on the voltages applied to a leg (x, y-coordinates as defined by convention):

$$\vec{D}(\phi) = \begin{pmatrix} x_A(\phi) \\ y_A(\phi) \end{pmatrix} = \begin{pmatrix} m_{11} & m_{12} \\ m_{21} & m_{22} \end{pmatrix} \begin{pmatrix} U_0(\phi) \\ U_1(\phi) \end{pmatrix} = \boldsymbol{M} \cdot \vec{U} \tag{3.1}$$

For the second group of legs 'B', the phase is shifted by π, assuming identical properties of that group. Different actuator geometries (see Fig.3.28) can be taken into account by choosing the coefficients of the matrix $\boldsymbol{M}$ accordingly: For walking leg piezo actuators with bending legs $m_{12} = -m_{11}$ and $m_{22} = m_{21}$, while for clamp-sheer actuators $m_{11} = m_{22} = 0$. Therefore, only 2 coefficients have to be determined for actuators of these geometries from the measurements. A trajectory yielding a linear motion should fulfill following conditions (also see references [66, 71]):

- $x_A(\phi)$ and $y_A(\phi)$ are 2π-periodic.
- There is exactly one phase $\phi = \phi_0$ in the interval $[0, 2\pi[$, for which $y_A(\phi_0) = y_A(\phi_0 + \pi)$ with $y_A(\phi_0) < y_A(\phi)$ for $\phi \in]\phi_0, \phi_0 + \pi[$ as well as $y_A(\phi_0) > y_A(\phi)$ for $\phi \in]\phi_0 - \pi, \phi_0[$. For $\phi \in]\phi_0, \phi_0 + \pi[$, actuator group A is thus responsible for transporting the rod (also see Fig.3.1).
- The lateral speed of the load bearing actuator shall be as constant as possible in order to yield a steady motion of the actuator, especially in the hand-over region: $\frac{dx_A}{d\phi} = \text{const.}$ for $\phi \in [\phi_0, \phi_0 + \pi]$.

- The movements in both axis shall be as smooth as possible; at least continuously differentiable.
- The absolute vertical velocity of the load bearing actuator group should be smaller than that of the non-load bearing group, and as small as possible at handover points.

Two sets ($i = 1, 2$) of simple piece wise defined functions fulfilling these requirements are:

$$x_{A_i}(\phi) = \frac{3\sqrt{6}}{4\pi} x_0 \begin{cases} \phi & , \phi \in \left[-\frac{\pi}{2}, \frac{\pi}{2}\right] \\ \frac{4}{\pi^2}(\phi - \pi)^3 - 2(\phi - \pi) & , \phi \in \left]\frac{\pi}{2}, \frac{3\pi}{2}\right[\end{cases}$$

$$y_{A_i}(\phi) = \frac{1}{2}\left(1 + \cos\left(\frac{\phi^2}{\pi}\right)\right)^i , \phi \in]-\pi, \pi]$$

A value of $i = 1$ will yield a rounded triangular shape as trajectory (waveform 2) and $i = 2$ results in a trajectory the shape of a box with rounded edges (waveform 3). In order to obtain the voltages yielding approximately the desired trajectory, one simply inverts the model matrix and multiplies it with the trajectory. Waveform 1 is based on trivial sine/cosine functions and corresponds to an elliptical trajectory with an offset.

3.9.3 Results

In the following, data on the validity of the piezo model, the performance of the optimization procedure as well as on the characteristics of the LT40 piezo actuator is presented.

Characterization of the stepsize for different loads and validation of the piezo model In order to validate the piezo model, the piezo actuator was rewired and driven such that the sets of legs attacking the ceramic rod from the opposite side were moving in tandem with their counterparts. Both actuator groups were performing the same elliptic motion (waveform 1), so that the rod was oscillating in x- and y-direction. The model presented in equation 3.1 is fitted to the data with a R-square value greater than 0.98 (Fig.3.29a). The model may thus generate an initial waveform to be used as starting point for the optimization procedure. Plotting the leg deflection in x-direction (travel direction) versus the difference of the voltages applied to one leg yields a linear relationship in case there are no nonlinear effects present such as hysteresis and the piezo leg is accurately described by the linear model. This is not expected, and this expectation is confirmed by the distinct hysteresis loop that the experimental data exhibits (Fig.3.29b). A nonlinear model would provide a better starting point. A distinct hysteresis

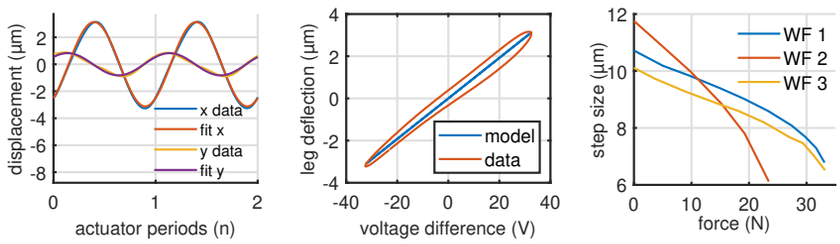

(a) (b) (c)

Figure 3.29: a) The trajectory of the tips of the legs plotted versus the actuator period; the linear model is fitted to the data in order to determine the model coefficients and verify the model. b) The presence of hysteresis is confirmed by plotting the leg deflection in x versus the difference in voltage applied to both elements of a leg. c) Experimental step size dependency on the external force for the optimized waveforms.

demands, that the procedure has to be applied in an iterative manner. In Figure 3.29c, a comparison of the dependency of step size from load is shown for the three waveforms defined earlier when optimized. While waveform 2 allows for the largest step size, it also produces the smallest maximum force. The general behavior observed is in agreement with the literature: Increasing the load first results in a linear reduction of step size, while for higher load slippage of the legs sets in, resulting in a drastically reduced step size (stalling). [63] This results in increased wear.

Scaling of waveforms To investigate the behaviour of the piezo under a variety of loads when scaling the waveforms, the step size in dependence of the actuator load was recorded for different scales and types thereof: Both x- and y-motion were varied. When scaling the x-motion, one would expect that the difference in clamping force on the rod, defined by the difference between y-position of transporting and non-load bearing legs, is practically unaffected. This assumes that both tips are in contact with the rod at all times. Thus, stalling should start out independently of the scaling, while the step size should be proportional. However, scaling the y-motion will reduce the difference in clamping forces on the rod and as a result, one would expect stalling to set in earlier compromising the maximum obtainable actuator force while also affecting the step size and increasing wear. These expectations are confirmed by the experimental data shown in Figure 3.30. The pretension of the legs is also affected by the offset changing as a side effect of the scaling in our case. It is worth noting that the overall pretension of the piezo elements is defined by a leaf spring; as the largest possible step size was of interest and reduced pre-tensioning due to a slightly less deformed leaf spring having minor effects only, no action was deemed necessary.

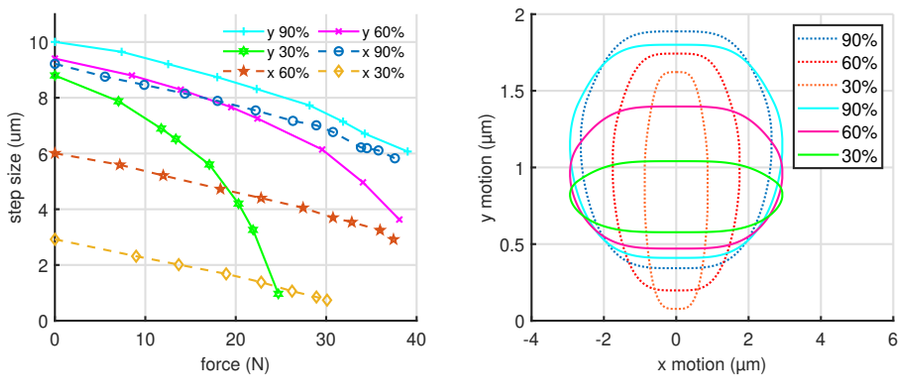

(a) (b)

Figure 3.30: a) Step size versus external load when the trajectory of waveform 2 is scaled in x- and y-direction (dotted and full lines); b) Tip trajectories predicted by the linear model for different scales: x is the lateral deflection of a leg, y the elongation.

Iterative optimization of the waveforms When iteratively applying the optimization procedure, the termination criterion is, that the nonlinear periodic error is converging due to having reached limits imposed by measurement noise or manufacturing tolerances. In Figure 3.31a, the resulting deformed voltage driving waveform for one of the two voltages acting on a leg is shown for the LT40 actuator. Additionally, the speed of the piezo tip along the trajectory is shown based on the linear piezo model for the unoptimized and optimized function. The optimization alters the speed to be more constant along the trajectory with spikes at the handover points, where corrections are required to yield a more linear motion of the ceramic rod. If one subtracts the linear trend of the motion, one can better compare the effect of the optimization on the periodic deviation or error (see Fig.3.31b): With each iteration, the periodic error is reduced until converging at a value about one order of magnitude below the initial one. The proposed waveform with $i = 2$ (waveform 3, Fig.3.31c+d) shows an analogous behavior as a result of the optimization. However, the initial periodic nonlinearity error is lower than for the trivial sine-based waveform. Fewer iterations are required and the final waveform is not deformed as much as waveform 3 since a model-based trajectory was used as a starting point, fulfilling all but the speed requirement imposed on a trajectory that yields a highly linear response. The residual deviation is dominated by a contribution with a frequency of 1 per period, which may stem from the fact, that the different legs behave slightly differently (piezo expansion coefficients due to contacting of the electrodes, and manufacturing tolerances of stack dimensions, ...). So far, it was assumed that all legs behave the same

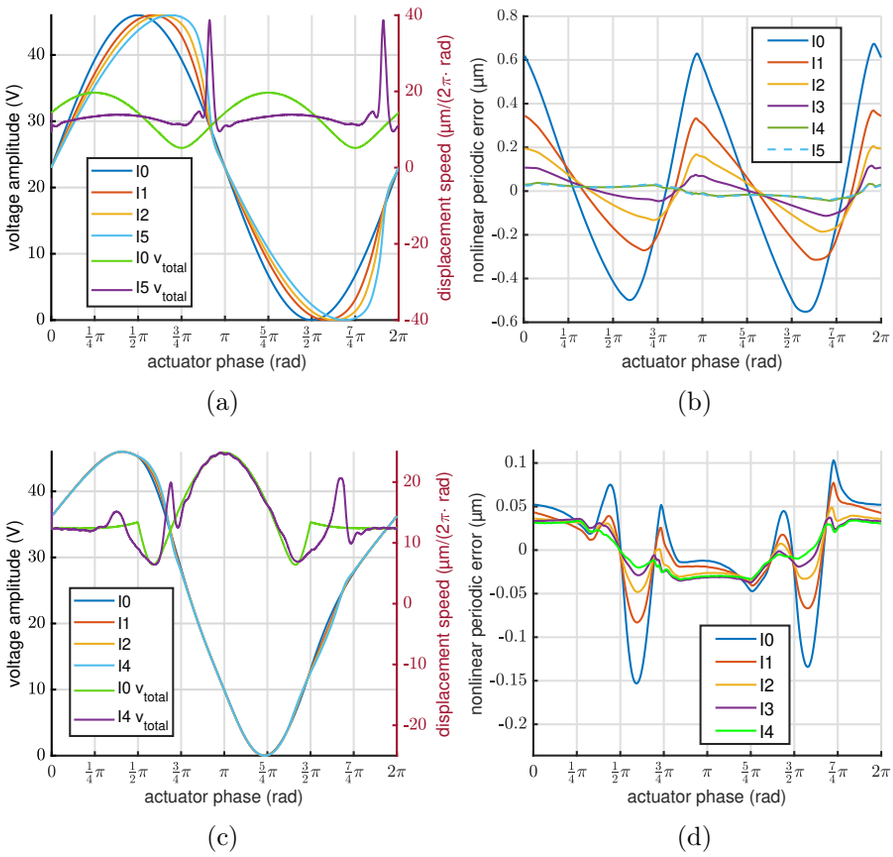

Figure 3.31: a+c) Plotted is the voltage U_0 for waveforms 1 (a) and 3 (c) over the actuator phase for different iterations of the optimization process. Iteration 0 is the original waveform. Total speed along the trajectory of the piezo tips in units of µm per actuator period for the unoptimized and optimized case is estimated by the linear model. In b+d) the experimental data on the periodic non-linearities is shown versus the actuator period for a number of iterations.

and merely shifting the phase upon optimizing the waveform is sufficient to be limited by measurement noise only. In practice, better results may be obtained by scaling the voltages for actuator groups A or B to compensate for the different effective piezo expansion coefficients of the other group or even optimizing them separately.

3.9.4 Changing the direction of travel

The optimization of a waveform yields a more linear response for one direction of travel only; moving in the other direction, there is still a nonlinear periodic error. In case, the piezo legs are symmetric in their response, the same waveform can be used for the reverse direction after switching the voltages U_0 and U_1 as well as U_2 and U_3 and time inverting the actuator phase $\Psi(\phi)$. The experimentally determined response for these scenarios is plotted in Figure 3.32 in terms of the deviation from a linear motion: The periodic non-linearity in the forward direction (yellow, waveform 3, optimized) is smallest. In the reverse direction (purple, waveform 3, optimized), the performance is slightly worse, as would be expected due to symmetry considerations.

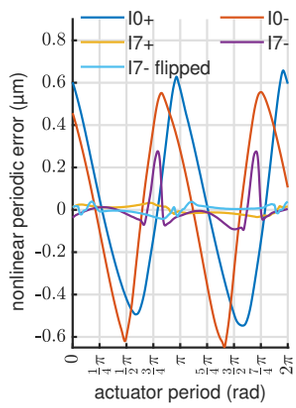

Figure 3.32: Data on the nonlinear periodic error for travel in the nominal and the reverse direction using various waveforms, for details see text.

However, switching voltages and time inverting the optimized waveform 3 (light blue) yields similar results for travel in the reverse direction. Doing so allows both legs to maintain their position when switching to the waveform look-up table for travel in reverse direction. Results for the unoptimized waveform in the forward (dark blue) and backward direction of travel (red) are shown for comparison.

Using the voltage waveforms derived, the residual motion is caused mainly by hysteresis not accounted for in the linear model and thus requires an iterative optimization. Compared to a purely model-based approach, the result was initially thought to be only limited by the measurement accuracy and repeatability. The data recorded showed that manufacturing differences of each leg must also be accounted for in both approaches. Nevertheless, depending on the initial waveform used, the nonlinear periodic error was reduced by up to one order of magnitude by applying the proposed optimization procedure iteratively. Furthermore, closed-loop operation is much simplified as symmetries allow for the usage of one optimized waveform for both directions of travel. Scaling of the trajectories of the piezo legs tips showed that variations in x-direction yielded a different step size without compromising the maximum actuator force while scaling y only or both x and y will always result in a reduced maximum actuator force with stalling setting in earlier. Besides benefiting the open-loop operation of the bimorph piezo drive, the control effort and gain during closed-loop operation with phase-independent, fixed control parameter sets is much higher, as the

response of the actuator using unoptimized waveforms may approach zero around the hand-over of the ceramic rod between actuator group thereby diminishing the controllers' performance. Please note, that if a sign change in speed occurs at high load during hand-over, this corresponds to a stalling by slippage. The algorithm can not be applied in such a case because the response is neither monotonous nor reproducible (see Fig.4.9b).

3.10 Summary of results

The most important results obtained from the measurements presented before can be summed up as follows:

1. The pupil alignment was completed and associated results regarding linear TTL and longitudinal pupil offsets obtained by small angle scans around field angle 0° showed that:

   (a) A precision in the determination of the lateral pupil offset of $\pm 19\,\mu m$ can be obtained (external pupil, scaled to LISA in case of 135x magnification, see subsection 3.3.3).

   (b) Lateral pupil offsets of less than $656\,\mu m$ are readily obtainable (scaled to a magnification of 135).

   (c) Longitudinal pupil offsets $< 525\,\mu m$ in the detector plane are feasible, which are compatible with the LISA on-ground calibration budget ($< 700\,\mu m$).

   With the completion of the alignment, a test stand, that allows for this type of measurement, probing the accuracy and stability of the alignment as well as trying out AIT techniques, is fully operational.

2. The precision of the relative alignment of the QPDs situated in a common measurement path is found to be not limited by the noise of the differential interferometric measurement due to its high common mode noise rejection, allowing for a measurement precision better than $1.1\,\mu m$ (lateral displacement in the external pupil, assuming a magnification of 135x).

3. The compensation of linear TTL using active apertures for clipping of the RX beam and the role of the different definitions of the interferometric phase was investigated in the experiment and a simulation. The results nicely match and thus show that such simulations can be employed to infer the response to lateral beam shifts caused by the successor mechanism, the BAM.

4. The WFE of the refractive and reflective optics showed good agreement with tolerancing predictions (Monte Carlo simulations, $\lambda/20$), although a clocking in M3 was not corrected during alignment.

5. The FF TTL and RX phase noise due to jitter in- and out-of-plane was derived from the WFE measurements at various field angles. Within a field of regard of 500 nrad, the total TTL coupling due to the slope in the far field phase distribution is less than 1 mm. If the pointing jitter performance is better than currently allocated, this also relaxes the allowable for the TTL.

6. The first end-to-end TTL measurement in RX direction to determine the system TTL for a LISA representative setup in terms of telescope optics and optical readout (wide field OAT and heterodyne IFO) as well as the separation of piston caused by the IFPM was performed. Linear TTL, most likely due to the clocking of M3 of about 3.2 mm is expected to be fully removable, either in postprocessing or within the limits imposed by the optomechanics, by alignment of M3 or the IFPM to compensate. The maximum non-linear TTL coupling assumes a value of about 0.85 mm. Historically, one of the main concerns regarding the IFP payload architecture was that additional projection effects from the telescope might present a showstopper. Our findings prove that the modeling of TTL effects agrees well with the experimental results; thus, no showstoppers are found.

7. The optimization of thermal diagnostics, validation of the thermal isolation concept of the IFP setup, and dissipation measurements now allow for the experimental determination of the contributions of active elements to thermal noise. The information gathered within the thesis and the hardware developed will prove helpful in the characterization of active components, and allow for the maintenance and updating of the LISA performance budget.

8. The results obtained using the setup's seismic isolation and structural modeling hint at laser frequency noise being in the same order of magnitude as seismic noise contributions. Locking of the laser to a frequency standard could soon allow the identification of the next smaller contribution(s) setup other than laser frequency noise. [72]

9. The path length noise measurements show that while noise floors down to single picometers require a highly stable environment as well as a (quasi-) monolithic structure, for some frequencies, a noise floor down to $30\,\mathrm{pm}/\sqrt{\mathrm{Hz}}$ was observed. As the setup was neither expected to reach the path length stability levels that were allocated for TTL coupling effects nor it is required to, these results were still better than initially expected. They could be further improved upon in the future (see above).

10. Critical to the performance of TTL measurements, the angular noise of the fully integrated setup without seismic control or active pointing was already better than or only in slight violation of the requirement of $4\,\mathrm{nrad}/\sqrt{\mathrm{Hz}}$ (or, equivalently $100\,\mathrm{nrad}/\sqrt{\mathrm{Hz}}$ in the detector plane).

11. One of the highlights is the, to our knowledge, first demonstration of active pointing in a setup that features this level of representativeness for LISA (e.g. that includes a representative, scaled telescope, mechanisms, IFO, thermal environment...). The in-loop noise data

collected can be used as a reference for the DFACS controllers, which are already designed using the actuator noise measured within the scope of the IFP project.

12. For faster angular scans using bimorph actuators, or actuators with periodic nonlinearities in general, it turned out, that reducing the subdivisional error can increase the performance by reducing the control effort significantly or even prevent a loss of the link. Further investigations are ongoing regarding the behavior at various loads and whether optimization is required at various field angles/loads. Another solution would be an over-sized actuator that only experiences small loads and variations thereof with respect to the holding force in conjunction with either the algorithm presented or a controller design considering a phase-dependent gain of the actuator.

Chapter 4

Design and validation of the SPM

In this chapter, a mechanism prototype for another previously proposed advanced pointing concept for a LISA-like space-based gravitational wave observatory that enables an architecture with two bi-directional interferometric laser links per S/C referenced to a single active test mass is presented and investigated. Compared to the baseline concept TP (detailed in the introduction), SP eliminates an optical backlink connecting two individual OBs and a massive flexing harness, significantly reducing the DFACS complexity and avoiding self-gravity effects due to large moving parts. An experimental validation of the pointing jitter and creep of the pointing mechanisms' linear axis is performed. The general design procedure can also be employed in lithography or other applications requiring ultra-stable manipulation of one or more opto-mechanical degrees of freedom. Additionally, lessons learned concerning the hinges' design and that of the actuator group can be transferred to the baseline architecture.

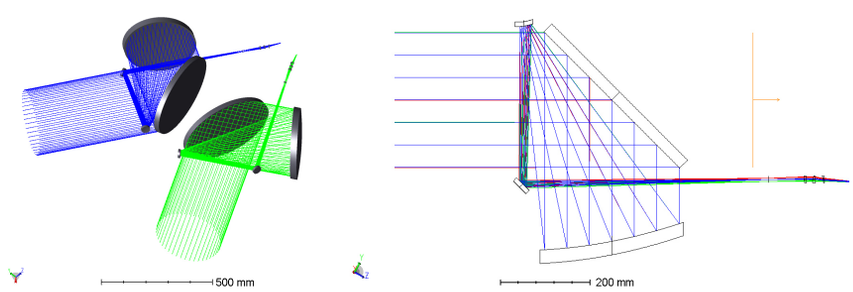

(a) (b)

Figure 4.1: The SP optical design using two curved mirrors and a refractive ocular. The design allows for compact accommodation thanks to the placement of the two main mirrors (Images: Courtesy ADS).

4.1 Objectives and the prototype mechanism

The second part of this thesis also received funding through the DLR project 50OQ1302, to fulfill the following objectives:

- Design of and pre-tests on a mechanism group representative in function for one used in SP
- Manufacturing and characterization thereof

The desired instrument sensitivity imposes demanding requirements on the instrument and environment in the LMB. Typical values for the SP-mechanism are specified in the table below using the frequency-dependent optical metrology noise shape function $u_n(f)$ introduced earlier.

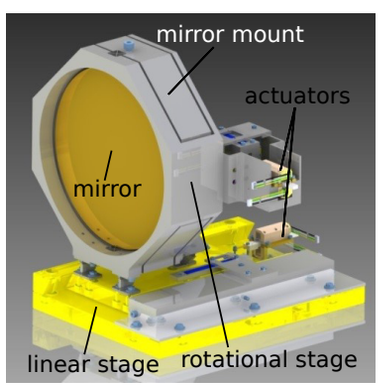

Figure 4.2: Rendering of the demonstrator mechanism: Dovetail linear guide made from Zerodur (bright yellow), the rotational stage made from grade-5-titanium (grey), and gold-coated Zerodur mirror (brownish).

As the linear axis performs a step-stare motion, the linear stage should come to rest quickly after stepping, causing only minor transient gaps and merely resulting in excess noise in the higher frequency part of the measurement band. This imposes not only harsh path length noise requirements for the linear stage, but also on controlled settling. Furthermore, the lowest mechanical resonance should be above the LMB to prevent excess noise in that frequency range. Critical in this regard is the stiffness of the (Haberland) hinges of the rotational stage. The positioning precision of the linear axis should be within several micrometers, and the linear and rotational axes should be tracked using an optical encoder with nanometer resolution. [8]

Parameter	**Goal**	**Comment**
PL noise	$3\,\mathrm{pm}/\sqrt{\mathrm{Hz}} \cdot u_n(f)$	tot. alloc. SP
angular noise	$1.67\,\mathrm{nrad}/\sqrt{\mathrm{Hz}} \cdot u_n(f)$	scaled from IFP
thermal stability	$10\,\mu\mathrm{K}/\sqrt{\mathrm{Hz}} \cdot u_n(f)$	due to CTE

A CAD rendering of the finalized SPM demonstrator prototype is shown in Fig.4.2: The mirror mount made from grade 5 titanium (brownish-grey) is mounted on the yellowish Zerodur dovetail linear guide. The mirror inserted is made from a gold-coated Zerodur substrate.

4.2 Design and dimensioning of the SPM

In this section, we discuss some detailed design considerations for the linear stage (including surface properties, choice of materials, and actuator technology) and the rotatory stage of the SPM building on experience from two mechanisms previously built and validated: The IFPM (in cooperation with TNO) and the SCS finding application in the IFP project. [28, 73]

4.2.1 Linear stage

Desired is a compact linear guide allowing for more than 66 mm travel that can be built from non-magnetic materials while providing the requested levels of path length stability. Path length stability requirements are especially harsh due to the fact that any path length jitter directly adds to measurement noise. To this end, a dovetail linear guide made from Zerodur was selected for the SPM demonstrator. While for a step-stare motion, a stepping motor that can perform $180\pm20\,\mu$m positional increments and covers a range of about 66 mm (including redundancy switching) is sufficient, we opted for a bimorph piezo actuator of the walking leg type (LT40 Piezomotor), that allows for sub-nanometer positioning and provides the desired stroke as well as an actuation force of about 35 N. [60] The position of the stage can be tracked using an optical encoder (Mercury II 6000V by Celera Motion). Our reasons for choosing the LT40 are that it is conceivable to integrate the piezo legs directly into the dovetail in a very compact future design. Otherwise, a standard stepper-motor-spindle-drive would be the more robust and simple choice. In addition, the choice is practical for the prototype as it allows us to use the same control electronics as for the rotational axis.

Path length stability To obtain the picometer path length stability of the linear stage, we designed the linear stage for minimum thermal expansion. It is consequently made from the glass-ceramic Zerodur, with a carriage that is pushed against an angled stopper block by a second angled and spring-loaded block while gliding on a base plate (see Fig.4.3). To provide well-defined contacts without the canting of the Zerodur parts, a combination of an aluminum pusher and Zerodur push block instead of a simple Zerodur pusher is used. As the CTE of Zerodur assumes a value of about $10^{-8}\,\mathrm{K}^{-1}$; in combination with a length of less than 0.1 m and

an environmental temperature stability as specified above, theoretical path length stability of $0.01\,\mathrm{pm}/\sqrt{\mathrm{Hz}} \cdot u_n(f)$ should be obtainable.

Tribological properties and required spring force The carriage features three machined pads towards the plane baseplate, while the spring-loaded push block and the stop block are in contact with two pads on the sides of the dovetail carriage each.

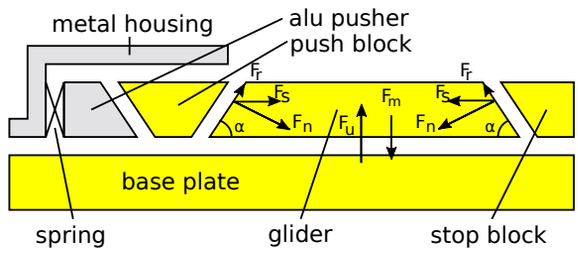

Figure 4.3: Forces acting on the dovetail guide generated by gravity and spring tensions: F_s: Spring force, F_n: Surface normal force, F_r: Friction in side-interfaces, F_m: Gravity force, F_u: Total normal force on the bottom of the carriage, F_c: Friction force, points in the opposite direction as F_s.

The spring force must overcome the static friction in all three interfaces for the stage to be adequately guided without canting or jamming. At the same time, the springs should not be oversized, as this would drive the actuator sizing and cause excessive stress in the Zerodur. To allow the usage of a compact 35 N-actuator, a surface coating with low static and dynamic friction is applied to the polished stop block, base plate, and spring-loaded push block. At the same time, the carriage contact pads feature a rough surface. We assume a dovetail-angle of $\alpha = \frac{\pi}{3}$, a friction coefficient of $\mu = 0.05$ for Diamond-like Carbon (The DLC static friction coefficient is tunable from 0.01 to 0.5), and a spring force of $F_\mathrm{s} = 31.32\,\mathrm{N}$, exerted by three multi-waved washer springs. [74–76] The condition for proper gliding on the side interfaces, $\mu < \cot\alpha = 0.58$, is fulfilled with ample margin. Considering the total force due to the mass of the carriage of $F_\mathrm{m} = 40\,\mathrm{N}$ for testing on the ground, the friction on the bottom F_c is

$$\begin{aligned} F_c &= \mu F_u = \mu\left(2F_\mathrm{n}\cos\alpha + F_\mathrm{m} - 2F_\mathrm{r}\sin\alpha\right) \\ &= 2\mu F_\mathrm{s}\frac{1-\mu\tan\alpha}{\tan\alpha+\mu} + \mu F_\mathrm{m} \approx 3.6\,\mathrm{N} \ll F_\mathrm{s}. \end{aligned} \tag{4.1}$$

Thus, the spring tension is sufficient to ensure proper guidance of the dovetail carriage.

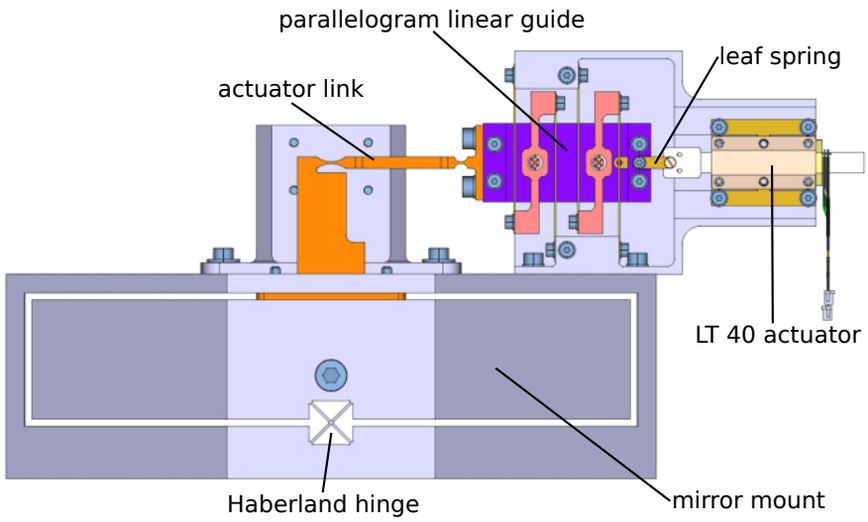

Figure 4.4: Rotational stage: The linearly moving actuator group is decoupled by not only the two solid state hinges in the actuator link/leaver arm part but also using a symmetric linear guide comprised of four blade springs as well as four small flex pivots and a small copper beryllium leaf spring. The mirror surface is aligned such that the axis of rotation is coincident with it, thus minimizing projection effects.

4.2.2 Rotational stage

To achieve the required angular stability and an angular range of ±1deg, an actuator technology previously validated for the IFP concept is employed: Bimorph piezo actuators of the walking leg type allow for large strokes while at the same time providing the precise positioning capabilities of conventional piezo actuators. Furthermore, the voltage waveforms driving these actuators can be optimized to yield a highly linear response, which is beneficial for open-loop operation. [60] Here, a PiezoMotor LT40 actuator was chosen, as it provides up to 35 N of force and the desired stroke while being suited for operation in a vacuum featuring a mass of only 60 g. However, these actuators need to be protected from external moments and forces on one hand while they also perform a periodic parasitic motion orthogonal to the nominal direction of actuation. Thus, in addition to using a copper-beryllium leaf spring (Fig.4.4, right), we decouple the rotational motion from the actuator using a symmetric linear guide and an actuator link with notch hinges. The symmetric linear guide comprises four blade springs and four small flex pivots. Symmetric guides prevent parasitic movements and were implemented here for comparison to an IFP mechanism prototype employing a simple parallelogram guide comprised of two-blade springs. [73] The actuator link features four notch hinges to decouple the rotational from

the linear motion. The primary rotary hinges are cross-flexural pivots, combining very low hysteresis, center shift, and backlash while providing a sufficient angular range and lifetime. [17,77,78] All hinges are no-friction, solid-state ones to obtain the desired angular noise performance. The mirror cage is manufactured from Titanium grade 5 using Electric Discharge Machining (EDM), which allows for the fabrication of the mirror cage and hinges out of one block of material in a single work step, ensuring a near-perfect mutual alignment of the two hinges and minimal tensions that otherwise could cause a bistable behavior. Alpha case, an oxide layer formed on the machined surface and removal thereof were considered and performed. The residual alpha case is not expected to impact the performance.

Path length stability As grade 5 Titanium has a CTE of $8.6 \cdot 10^{-6}\,\mathrm{K}^{-1}$, an effective material dimension of $20.2 \pm 5.0\,\mathrm{mm}$ and the temperature stability of the environment specified above yield a theoretical path length stability of $1.74 \pm 0.43\,\mathrm{pm}/\sqrt{\mathrm{Hz}} \cdot u_n(f)$. Rearranging the rotational stage's mounts (i.e. to a 120°-pattern) could further reduce this value by providing a centered, near-static position (ideally being coincident with the mirror surface plane and located on the hinges' rotational axis) at the expense of a slightly increased assembly effort.

Angular stability Contributors to open loop angular noise are thermoelastic effects, piezo amplifier voltage noise, and periodic nonlinearities of the motion due to imperfections of the periodic driving and the actuator itself. [60]

The system thermoelastic effects are estimated from its effective expansion coefficient $\sigma_{\mathrm{eff}} = \sigma_{\mathrm{actuatorlink}} + \sigma_{\mathrm{ceramicrod}} = 4 \cdot 10^{-6}\,\mathrm{K}^{-1} \cdot 80\,\mathrm{mm} + 100 \cdot 10^{-6}\,\mathrm{K}^{-1} \cdot 20\,\mathrm{mm} = 2.32\,\mu\mathrm{m\,K}^{-1}$, the thermal jitter s_T as specified above, and the lever arm length $l = 70\,\mathrm{mm}$: $s_{\varphi,\mathrm{TE}} = \sigma_{\mathrm{eff}} \cdot s_T \cdot l^{-1} \approx 0.3\,\mathrm{nrad}/\sqrt{\mathrm{Hz}}$.

Voltage jitter is dominated by discretization noise $s_U = U_{\mathrm{lsb}}/\sqrt{6 f_{\mathrm{dac}}} \approx 640\,\mathrm{nV}/\sqrt{\mathrm{Hz}}$ (with $U_{\mathrm{lsb}} = 0.7\,\mathrm{mV}$ and $f_{\mathrm{dac}} = 0.2\,\mathrm{MHz}$) and is considered via an actuator response factor of $C_{\mathrm{LT40}} = x_0/(\pi \cdot U_0) \approx 21\,\mathrm{nm/V}$ (with a peak-peak voltage of $U_0 = 46\,\mathrm{V}$ and a step-size $x_0 = 3\,\mu\mathrm{m}$), resulting in a negligible angular jitter of $s_{\varphi,\mathrm{U}} = C_{\mathrm{LT40}} \cdot s_U \cdot l^{-1} \approx 0.2\,\mathrm{prad}/\sqrt{\mathrm{Hz}}$. Thus, the actual noise terms are well below the requirements defined above.

Potentially the most significant open-loop contribution is subdivisional nonlinearity, which with typical error amplitudes at a 1%-level (i.e. $a_\varphi = 0.01 \cdot x_0/l \approx 430\,\mathrm{nrad}$) affects the angular noise spectrum at the base frequency $l\dot{\varphi}/x_0$ and its harmonics. With an actuator drive optimized for a smooth shape of the subdivisional errors, the harmonics fall with at least $1/f^2$, such that at realistic small angular speeds of $|\dot{\varphi}| \leq 2\,\mathrm{nrad/s}$ and a resulting fundamental frequency of $50\,\mu\mathrm{Hz}$ the noise is well within the control bandwidth of DFACS, which uses DWS data as feedback. Thus,

interferometric sensing limits closed-loop angular noise performance at low frequencies.

Required actuation force and Eigenfrequencies To verify that the actuator provides sufficient force (also see subsection 3.9.3, Fig.3.30a) for movement over the entire desired angular range of ±1°, analytical calculations and numerical simulations using FEM were performed. We also calculated the lowest Eigenfrequencies of the structure to ensure that those are neither in the measurement band nor close to acoustic Eigenfrequencies of our laboratory or other known sources of disturbances. The results are summarized in the table below; errors are estimated to be below five percent of the values:

Parameter	**Result**	**Comment**
act. force Haberland hinges	4.64 N	@ 1°, 70 mm lever
act. force lin. guide	0.50 N	@ 1°, 70 mm lever
act. force actuator link	0.78 N	@ 1°, 70 mm lever
total actuation force required	5.92 N	@ 1°, 70 mm lever
Haberland hinge lateral stiffness	18.8 N µm^{-1}	lowest struct. mode above 150 Hz
Haberland hinge center shift	<1 µm	@ 1°, FEM
lowest rotational mode	7.97 Hz	w.o. guide and act.
lowest rotational mode scaled	$\sqrt{\frac{5.92\,\mathrm{N}}{4.64\,\mathrm{N}}} \cdot 7.97\,\mathrm{Hz}$ = 9 Hz	incl. lin. guide, act. link
lowest structural mode	173.73 Hz	FEM w.o. act.

4.3 Experimental setups

In the following, the layout of the experimental setups for tribological tests of the low-friction surface coating critical to the proper functioning of the liner guide is detailed as well as the experiments for measurement of the angular jitter and creep.

4.3.1 Tribological tests

To measure the friction coefficient of different material pairings that were under consideration for usage in the linear stage of the SPM demonstrator, a simple setup was used: The friction partners can be placed on top of each other, and a force normal to the surface can be applied by placing a mass on top of the upper friction partner. The upper friction partner can be moved relative to the lower one back and forth while measuring the force

required, and the motion is monitored using an optical encoder as well as a commercial three-beam IFO (SIOS 5000TR, not shown). This setup is depicted in Fig.4.5a.

Dividing the force required to move the sample by the force generated by the mass normal to the sliding surface, the static and dynamic friction coefficients can be determined. Moving the sample back and forth is essential to remove systematic errors introduced by the tilt of the platform surface normal relative to the gravity gradient; experiments are typically performed under vacuum conditions at room temperature, as humidity can have a large impact on the friction coefficient.

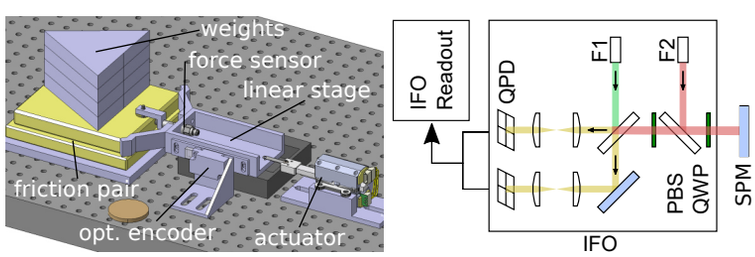

(a) (b)

Figure 4.5: a) Friction testbed with actuator, linear stage, and optical encoder (redundant SIOS 5000 TR three beam IFO for displacement and noise measurements not shown) and a capacitive quartz force sensor for recording the force required for sliding the upper sample weighted down using metal plates to apply a force normal to the surface. b) Layout of a setup for path length noise measurements. The SPM is placed in front of a custom IFO. The measurement beam is polarization-routed via a QWP and a PBS. QPDs serve as detectors. F1 and F2 are fiber collimators for a LO and a measurement beam. The SIOS 5000TR can be used as an alternative in the case of angular noise tests (adapted from Ref. [14]).

4.3.2 Path length stability measurements

To verify that the path length stability is not compromised by thermoelastic or other effects such as relaxation of tensions due to slip-stick, a heterodyne IFO, which has its optical components bonded to a Zerodur baseplate using hydroxide catalysis bonding, was used for measuring path length stability. [9, 14, 50] The layout of the optical system, as well as a description of the components used, can be seen in Fig.4.5b. Preliminary measurements have been performed with the SIOS 5000TR. In addition to path length noise measurements, several temperature sensors with microkelvin resolution were used to record the thermal noise to ensure its representativeness; experiments are performed under vacuum conditions at room temperature.

4.3.3 Angular noise measurements

As mentioned above, the same heterodyne IFO can perform differential wavefront sensing measurements or a two-beam angle measurement of the mirrors' surface. Again, the three-beam IFO was used for the preliminary two-beam measurements, this time equipped with a monolithic Zerodur periscope for increasing the beam separation and, thus, the angular resolution at higher frequencies.

4.4 Hinge natural frequency and actuation forces

The combined required actuation force of the actuator link, parasitic-motion-compensated parallelogram linear guide, and hinges was measured via a capacitive sensor to verify the expectation from the FEM simulations and the suitability of the chosen actuator. The maximum actuation force is critical for the optimization of the driving waveforms to obtain a more linear response or modify the stepsize, as those modifications can impact the maximum actuation force available; increasing the stepsize can be useful, for example, to further reduce the fundamental frequency of periodic nonlinearities. A nano silk string was used for connecting the force sensor and the linear guide of the rotational stage. The natural frequency of the two Haberland hinges connected via the lever arm to the parallelogram linear guide with the Zerodur mirror inserted into the mirror mount cage and the actuator disconnected was measured by manually deflecting the mirror cage and measuring the oscillation using an optical encoder, to verify that the natural frequency is above the LMB. A damped sine wave is fitted to the measurement data to obtain the natural frequency. Connecting the stiff actuator significantly increases this frequency. Results are detailed in the following table - measurement and simulation are found to be in good agreement:

Parameter	**Measurement**	**FEM, anal. Model**
rot. axis eigenfrequency	$9.383 \pm 0.005\,\mathrm{Hz}$	$9.00 \pm 0.45\,\mathrm{Hz}$
actuation force for 1 deg	$5.51 \pm 0.55\,\mathrm{N}$	$5.92 \pm 0.29\,\mathrm{N}$

The actuation force provided by the LT40 bimorph piezo actuator of 35 N is thus more than sufficient.

4.5 Tribological testing of low friction solid film coatings

First, a different version of the desired DLC coating with a friction coefficient of $\mu_g = 0.125$ instead of $\mu_g = 0.05$ was produced and tested for verification of adherence to polished Zerodur and checking if the expected friction

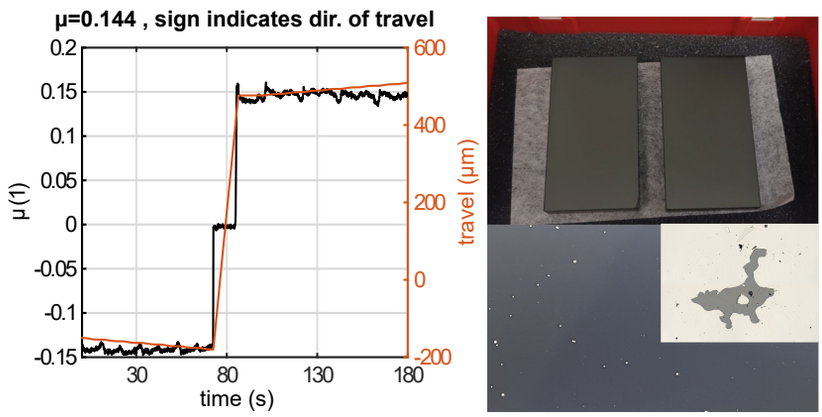

(a) (b)

Figure 4.6: a) Typical friction measurements involve travel in both directions to remove systematic errors (e.g., caused by platform tilt) b) Polished and DLC-coated Zerodur blocks with dimensions of 70x40x10 mm^3 before (top) and after (bottom) storage; bottom image insert vertical side is 1 mm long.

coefficient could be obtained. The sample, coated by IHI ionbond AG, is shown in Fig.4.6b. Visual inspection shows a smooth and continuous DLC film that is not flaking off or showing any other signs of lack of adherence or delamination of the coating, which could compromise mechanism function due to locally increased friction or cold welding and result in excess contamination. The experimental data of a Zerodur carriage with a surface roughness of $R_a = 0.25\,\mu\mathrm{m}$ on a polished Zerodur substrate (with a surface quality of $\frac{\lambda}{10}$ and coated with DLC of the type Tribobond 43) is shown in Fig.4.6a: The friction coefficient of $\mu = 0.144 \pm 0.020$ is in good agreement with the data provided by the manufacturer.

As the visual inspection of the sample and the tribological data looked promising, the counterparts of the Zerodur carriage were subsequently coated with an ultra-low friction coefficient version of the DLC coating (Tribobond 43 ADLC-K). While the properties of the ultra-low friction coating were not verified independently by us, even a friction coefficient similar to the one obtained for the higher friction coating would result in a total friction force of $20.78 \pm 1.35\,\mathrm{N}$, which is smaller than the available actuator force of 35 N (even assuming an error in the spring force of ten percent).

Therefore, the proper guidance of the dovetail carriage is guaranteed, and the actuation force of the LT40 piezo drive is sufficient. Over time, the DLC coating showed minor delamination from the Zerodur substrate; for the samples in storage as well as the linear guide.

4.6 Hysteresis and bistable behavior

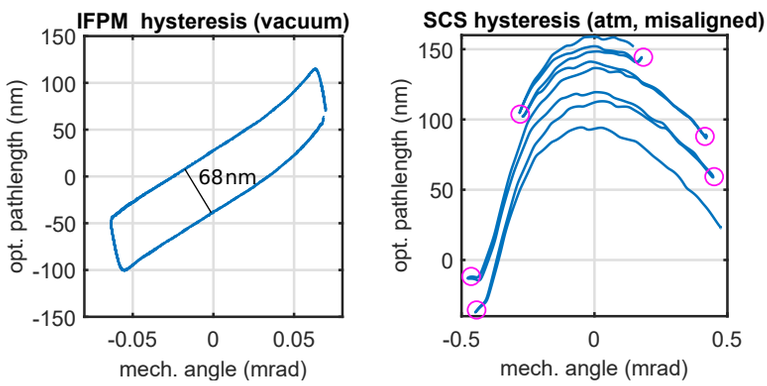

(a) (b)

Figure 4.7: Path length hysteresis measurements for IFP (a) and SCS (b); for details see text.

Previous work with the IFP mechanism prototype revealed significant mechanical hysteresis in optical path length vs. mechanical angle (see Fig.4.7a). For further investigations into the root causes of the hysteresis, another similar rotatory mechanism (so-called SCS, used to imprint the LISA constellation angular dynamics in a test setup for pointing architectures) has been characterized (Fig.4.7b). Although there is a significant path length drift over the measurement duration (due to ambient atmospheric test conditions), no hysteresis is apparent near the turnaround points when scanning the mechanism forth and back, as marked using pink circles.

First, we note that such measurements are not sensitive to displacement hysteresis in the nominal travel direction of the actuator group comprised of the linear guide and the actuator. Therefore, the entire actuator group is dismissed as the source of the path length hysteresis.

Next, one could suspect the mutual alignment of the primary hinges to cause a bistable behavior. This is ruled out by the data shown in Fig.4.7b, as here intentional misalignments between the hinges by $\approx$ 5 mrad had been introduced, which by far exceed any manufacturing errors during EDM of the monolithic IFPM and SPM prototypes. The same measurements eliminate phase delays in the interferometric readout to explain the hysteresis in Fig.4.7a. Another possible source for hysteresis could be a plastic deformation of the linkage between the linear guide and the rotatory mirror cage or of the primary rotary hinges. FEM-analysis indicates that both parts are far from plastic deformations with a critical load factor of ≈ 2 for the leverarm links and ≈ 4 for the hinges of SPM and IFPM.

However, this does not consider the alpha case created during

Component	Hysteresis cause	Mechanism affected	Status
actuator	voltage-driven piezo	all	ruled out
lin. guide	bistable behavior (alignment)	IFPM, SPM	ruled out
link lin. guide mirror mount	plastic deformation	IFPM, SPM	ruled out (FEM)
hinges	alpha case on surface creating nonlinearity	IFPM, SPM hinges fabricated w. EDM	likely in IFPM
	alignment of hinges (bistable behavior)	SCS	ruled out
phasemeter	phase delays	IFPM, SCS	ruled out

Table 4.1

the EDM processing of the IFPM prototype. In contrast, the hinges in the SCS mechanism were milled and thus are without alpha-case. Typical titanium alpha case thicknesses from EDM range from 40 µm for un-optimized processing down to 1 µm after process-optimization. [79,80] We conclude that the alpha case is the likely source for the hysteresis observed with the IFP mechanism, and thus took special caution to use optimized processing for the SPM prototype. The corresponding measurement data is shown in Fig.4.8, showing a path length hysteresis below 1 nm. The minor offset drift is attributed to temperature drifts and pressure increases due to outgassing and virtual leaks. Linear TTL due to a lateral offset of the rotational axis was subtracted, and the response shown results from second-order TTL due to the longitudinal offset between the mirror surface and IFO pupil plane. Table 4.1 summarizes the results obtained.

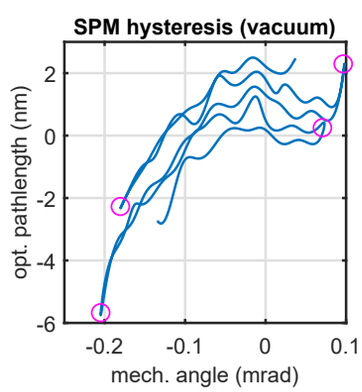

Figure 4.8: Path length hysteresis measurement for the SPM; for details see text.

To analyze the actuator group, we command linear movements of the SPM using un-optimized harmonic driving voltages for the actuator while monitoring the position of the linear guide.

The bistable behavior of the symmetric linear guide causes popping processes at four different angles or actuator travels due to inversion. These processes can result in slippage of the ceramic rod and a roughly 10 µm jump in travel corresponding to a 143 µrad change in mechanical angle of

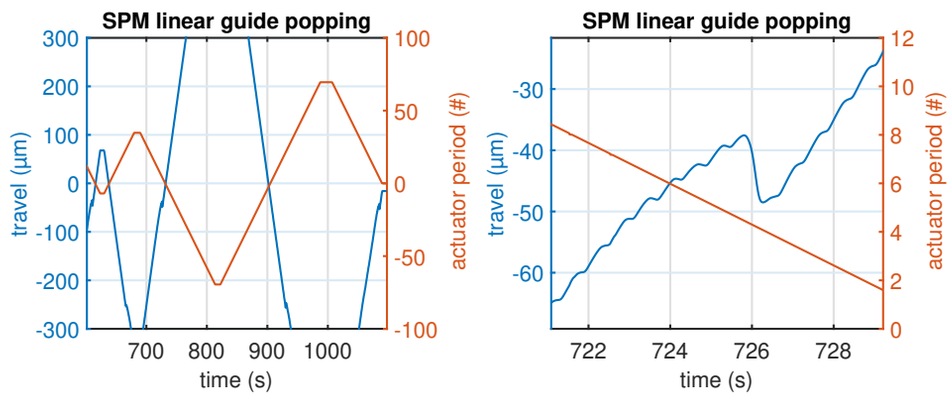

(a) (b)

Figure 4.9: a) Travel of the linear guide and commanded actuator position (in several steps) over time. Jumps indicate the popping of blade springs, a typical bistable behavior. b) The bistable behavior causes a decrease in stepsize, stalling (as can be inferred by observing the periodic nonlinearity), and slippage of the ceramic rod of the bimorph actuator in case both parallelograms are applying a pretension in the same direction. The actuator phase is increasing linearly in time, while the unoptimized voltage waveforms for driving the piezo yield a motion with cyclic errors, which aids in showcasing the stalling of the actuator near the position of an inversion process.

the mirror surface normal, depending on the history of the travel and the current travel by actuator (Fig.4.9).

This jump only occurs when both parallelograms apply a pretension in the same direction. If one travels far enough in both directions, both parallelograms of the guide are deformed in the same direction, causing that jump in displacement at two different positions. Otherwise, no significant slippage can be observed for one of the two positions, but there is a substantial reduction in the step size of the actuator.

For LISA, due to an interferometric field of view of $\approx 3.5\,\mu\text{rad}$, such jumps in the pointing angle would cause a link loss and thus have to be prevented for any of the three payload architectures. Therefore, parts that might cause bistable behavior must be avoided in the mechanism design, or it must be ensured to operate outside the bistable region, corresponding to a certain built-in pre-tension respective operation far outside the region where such effects can occur.

4.7 Creep of the linear stage

To quantify the creep of the linear stage after repositioning, travel of the linear stage under vacuum conditions is performed while measuring the displacement of the mirror (see Fig.4.10). For initial tests, the SIOS IFO is used. Our linear stage design features an actuator connection with a built-in backlash so that the actuator can disengage by simple retraction. In case

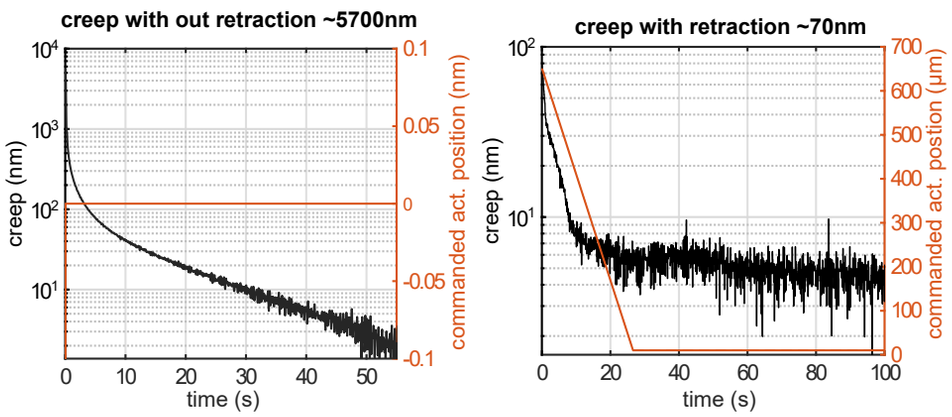

(a) (b)

Figure 4.10: Creep of the linear axis without retraction of the actuator to prevent excess tensions and ensure an all-Zerodur transfer function. Left axis: creep measured with a SIOS 5000TR (black), right axis: Commanded actuator position (red) from several ms before the start to the end of the measurement, prior to which a travel greater than 100 µm is performed.

one performs travel without disconnecting the actuator, the copper beryllium blade spring used for decoupling the actuator from undesired lateral forces and moments causes excess tensions: The movement of the carriage shows a significant creep of 5700 nm (black curve). However, disconnecting the actuator by performing a retraction (red curve, open loop actuator position in Fig.4.10b) yields a much-reduced creep of roughly 70 nm which settles to below the measurement noise floor after approximately 10 s, causing only minor transient gaps in science-data gathering affecting the high frequencies in the LMB above 0.1 Hz roughly every six days.

4.8 Noise performance

Measurements confirm that the angular noise of the demonstrator mechanism is compatible with the requirement (see Fig.4.11a, green and blue curve). The three-beam IFO limits the measurement performance at high frequencies, as seen from a reference measurement on a static Zerodur reference mirror (red curve). The beam separation of 12 mm was increased

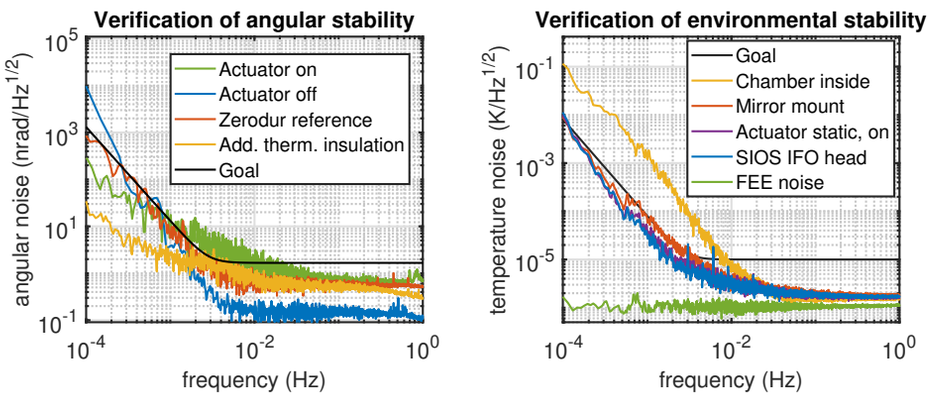

(a) (b)

Figure 4.11: a) SPM angular noise measurements using the SIOS IFO: Noise with active piezo driver and additional thermal insulation (green) compared to Zerodur reference (red), inactive piezo driver and added periscope for ruling out high-frequency contributions of the piezo driver (blue), inactive piezo driver and additional thermal insulation (yellow). b) Temperature fluctuations measured on the inside surface of the vacuum chamber (yellow), on mirror mount (red) and static actuator (purple), as well as SIOS IFO head (blue) and the requirement (black) are shown in addition to contributions of the temperature measurement board (green).

to 73 mm for the blue curve utilizing a monolithic Zerodur periscope, which consequently reduced the high-frequency noise floor. Therefore, the data shown at high frequencies should be considered an upper bound of the actual performance. Excess noise between 1 mHz and 10 mHz (green curve) is attributed to pink noise of the voltage amplifier, which is confirmed by powering down the amplifier (yellow and blue curves). On a final note, the higher-frequency angular noise performance is below our worst-case estimate of $0.3\,\mathrm{nrad}/\sqrt{\mathrm{Hz}}$ @ 1 Hz given above, indicating a sufficient understanding of the noise sources in our system.

A newly designed voltage amplifier with reduced flicker noise will ensure that the driver electronics will no longer limit the angular noise performance. The temperature fluctuations of the inside surface of the vacuum chamber (yellow), the titanium mirror mount (red), the powered-up actuator (purple), the SIOS IFO sensor head (blue), and the contribution of temperature measurement board front-end electronics noise (green) are shown in Figure 4.11b: While the thermal stability of the environment is not meeting the requirement at low frequencies, the temperature fluctuations of the mechanism itself are sufficient to meet angular and path length stability requirements.

4.9 Summary of results

The experimental investigation of the Siderostat Pointing concept showed no show-stoppers while also hinting at possible improvements in the design of future pointing mechanisms (used in gravitational wave detection):

1. The surface treatment using a DLC coating of the Zerodur counterpart of the carriage of the dovetail linear guide yields a friction force that is sufficiently low to be overcome by both the spring forces applied to the carriage and the force provided by the bimorph piezo actuator. Therefore, proper guidance and actuation of the linear axis are initially provided. Delamination of DLC from the Zerodur surface over time was observed to a minor degree, possibly posing issues with respect to particulate contamination. Therefore, alternative lubricants should be considered in addition to further investigations into the adhesion of DLC on Zerodur substrates (Such as CoolDiamond DLC®, which is applied at room temperature!).

2. The hysteresis in path length observed for the IFP mechanism is not present in either SPM nor SCS, most likely due to the removal of the alpha case, an oxide layer on the surface formed during the EDM process in manufacturing or fabrication by milling. Other hysteresis and non-linear effects, such as the observed bistable behavior of the symmetric parallelogram linear guide, must be addressed in LISA pointing mechanisms for any payload architecture to avoid a loss of the links or a measurement performance degradation. For telescope pointing, this should be considered both for the blades of the rotary hinges and the linear guide decoupling the actuator as well as the massive flexing cable harness connecting MOSA and S/C. To avoid oversight, these effects should be tested for in the fully assembled state. This is not easily performed for TP, as it requires gravity offloading.

3. Measurements of the angular noise and path length stability after translation along the linear axis (creep) of the SPM prototype are critical for demonstrating the feasibility of the Siderostat-Pointing concept. While we were able to demonstrate the angular stability of the static mirror that is compliant with the requirement, only preliminary path length stability measurements limited by the IFO noise floor are available so far. The post-nominal travel creep shows an exponential decay, which can be significantly reduced by disengaging the actuator. The resulting all-Zerodur transfer function should enable path length stabilities of the desired level for the linear axis, which will be verified using the monolithic heterodyne IFO of the IFP setup in future tests.

Chapter 5

Conclusion and outlook

In the first part of this thesis, the integration and characterization of the IFP testbed were detailed, and possible improvements and modifications were discussed. With the completion of the IFP test setup, a broadly representative test setup for a LISA-type optical payload allows for the characterization of system TTL coupling factors and driving noise sources (such as thermal, angular, laser frequency noise). This includes far-field TTL of the complete system based on the WFE measured and a first demonstration of active pointing using a DWS signal as feedback (featuring such a high level of representativeness).[1] The measurements performed, and results obtained thus permit the verification of core functionalities of the backup payload IFP for LISA. Additionally, AIT techniques for pupil alignment using TTL measurements were tested, providing information critical to the definition of OGSE in LISA.

In the second part of this thesis, a prototype for the SPM was realized, and its performance concerning the angular noise of the rotational axis and the creep of the linear axis was experimentally probed. This allowed for the verification of the functionality of a core element of the newly proposed SP payload architecture: Angular noise of the pointing mechanism was sufficiently low to be compatible with the requirements, and decoupling the actuator of the linear axis post-travel via retraction was shown to significantly reduce creep and, thus, lower the impact of transient gaps in the measurement band.

In addition to dispelling concerns associated with the TTL contributions from the IFP telescope, the results presented and summed up at the end of each part, aid in raising the technology readiness level and, thus, the credibility regarding the feasibility of two potential (backup or fall-back) options for the payload of a LISA-type mission.

[1] In terms of the optical setup and environ. conditions the tests were performed under.

5.1 Lessons learned and way forward

Four technologies that can find application in all three payload concepts were investigated:

- The compensation of linear TTL using the AAM was experimentally verified in a broadly LISA-representative breadboard and compared to corresponding simulations implemented in Matlab. This entailed retrofitting that mechanism after designing, integrating, programming, and testing it.

- The definition and iterative optimization of voltage waveforms for driving actuators featuring periodic nonlinearities and the design of low-noise amplifiers for driving the actuators were successfully undertaken. This greatly benefits the performance modeling of the DFACS and the design of the associated controllers.

- Design rules of frictionless solid state hinges featuring a negligible level of hysteresis in path length and exhibiting reduced bistable behavior, in particular, were identified: With the investigation into flaws in the design of the IFPM hinges resulting in hysteresis as well as into the bistable behavior in the linear guide of the SPM, the lessons learned will benefit the design of future ultra-high precision pointing mechanisms. The results presented highlight the importance of experimental testing and that stresses induced by parasitic moments and forces due to imperfect gravity offloading may cause bistable behavior in the hinges of the MOSAs during on-ground performance testing.

- The improvement of the thermal diagnostics by selecting components and choosing packages with minimal flicker noise allows for measurements of thermal noise due to the dissipation of active elements, and the lessons learned regarding the thermal isolation concepts and the criticality of adding thermal harness anchors will also find application in associated performance models.

Some questions are still open and should be tackled in the future. The following briefly discusses those and possible ways to address them.

- To ascertain the limitations regarding path length noise achievable with the IFP setup, the laser can be locked to external optical cavities. Additionally, simultaneous laser frequency stabilization can be performed using an optical cavity and a Doppler-free iodine frequency reference, exploiting the performance crossover towards lower frequencies. [59]

- The active seismic compensation system could also excite the setup with harmonic oscillations to derive the coupling from platform tilt to path length experimentally and to compare the results with the model. As the optics are mounted by gravity only, this was deemed too risky, although both a hardware and software emergency fail-save are in place.

- The excitation of oscillations of the room temperature, using excessive control parameters, was successful. Still, the gain is not high enough to allow for system-CTE measurements, as the thermal noise does not rise above the temperature noise floor detectable using the thermal diagnostics hardware. Here, the removal of the Neopor outer insulation material, as well as the usage of more potent actuators, may aid.

- The non-linear TTL performance of the SCS should be verified using a dedicated measurement. Also, in future implementations, the SCS should be integrated right from the start to allow for alternating scans of IFPM and SCS, allowing for the probing of linear TTL and telescope TTL right from the beginning.

- Improvement of DLC adhesion to Zerodur substrates could be attempted by using DLC deposition at room temperatures to decrease the stress in the film possibly responsible for the observed delamination (e.g., using CoolDiamond DLC®). Another possibility for improving adhesion is applying thin metal layers to promote adhesion and reduce lateral tension.

Appendix A

Additional information

A.1 Noise sources in heterodyne interferometry

In table A.1, a brief overview of typical noise sources in heterodyne interferometry and actions to mitigate those is given. While it is essential to understand the different noise contributions

Noise source	**Mitigation methods (not complete)**
Laser frequency noise	Locking to a frequency standard or
	an unbalanced IFO; in LISA: TDI [1, 58, 59, 72, 81, 82]
Path length noise	Lock of the relative phase of ref. and sig. beam
(unstable IFO part)	to an electronic reference (DSS) (fiber length stab.). [56, 82, 83]
Acoustic noise	Operation in vacuum, passive dampening of
	experiment suspension and elimination of sources.
Thermal noise	Radiation barriers, thermal capacitances, actively
	stab. lab and usage of low CTE materials. [52]
Seismic noise	Plattform (tilt) motion noise compensation
	in two to six-axis (active and passive) [3, 55]
Relative Intensity Noise	RIN active stabilization (DC,1-f,2-f)
	and balanced detection [57]
Electronics noise	Design: Choice of low (pink) noise components,
	chopper stab. OP-amps, relat. phase lock [82]
Periodic nonlinearities	Design of IFO, phase meter, and electronics [48]
Straylight	Adding of ND filter, balanced detection,
	optical design (baffles, coatings, wedged optics) [24, 51]
Shot noise	Laser signal power and usage of quantum sensing [51]

Table A.1: Possible noise sources in precision heterodyne interferometry and mitigation.

and knowledge of the underlying mechanisms and the typically associated noise shapes greatly aids in eliminating sources or at least facilitates attenuation of the noise, some noise sources are limiting. Either physically (shot noise) or due to the design of the setup (stray light, seismic noise...), which may be limiting in the current but not in possible future setups where lessons learned could be implemented. However, this is only possible if the noise sources have been

identified or pinned down. Sometimes, noise can trigger entire chains of effects such that the phase measurement is affected in a way that may not be clear without detailed investigations. For example, technological noise in a component driving the laser pump diode current can result in fluctuations in opical pump power that yield, in turn, RIN and, consequently, slight fluctuations in temperature of the facets of the non-planar ring oscillator crystal, in turn resulting in a change in laser frequency. Noise is often coupled, and special attention must be paid to the fact that control loops are orthogonalized. Otherwise, the effectiveness of control loops for stabilization of the environment, laser light, or any actuated variable, for that matter, may be compromised.

A.2 AAM simulation parameters

Simulation parameters for calculation of TTL by translation of the RX aperture clip:

Parameter	**Value**	**Remark**
LO beam waist	0.94 mm	measured
LO beam offset	[0,0,0]	
RX beam waist	0.86 mm	measured
RX beam geometric offset	[0,0,−0.0461 m]	due to AAM retrofit
Mag. refract. relay stage	1x	As in IFP
Wavelength laser	1064 nm	Nd-YAG NPRO
RX beam max tilt	450 µrad	OB level
RX aperture max offset	120 µm	<150 µm(linearity)
RX aperture diameter	700 µm	signal vs. added TTL
Clipping ratio	0.3723	RX clip diam./LO waist
QPD radius	500 µm	OEC GAP 1000 Q
QPD slit width	20 µm	OEC GAP 1000 Q
Image res. in pupil plane	512x512 pixels	10x interpol. of num. mesh
Simulated offsets	21	number RX clip offsets
Simulated angles	[5,5]	number hor./ vert. angles

Table A.2: Parameters for simulations investigating TTL resulting from the interference of two Gaussian beams on a segmented photodiode, where one beam is actuated in tilt.

Appendix B

Publications based on the above

Four peer-reviewed publications will be published based on the work performed within the scope of this thesis. Three further publications resulting from working on other projects within the scope of the LISA and NGGM missions - but not limited to those - will be published as well, and the near-complete first drafts are attached further below as well.

Active compensation of tilt-to-pathlength coupling in precision interferometry for LISA (See section 3.4.)
Status: Co-authors are reviewing the draft.

Elimination of periodic nonlinearities of actuators with internal periodic processes (See section 3.9.)
Status: Submission ready; pre-print published on arxiv.

In-Field Pointing: Validation of an advanced line-of-sight pointing concept beyond LISA This publication will be based on Chapter 3, excluding the sections making up the publications mentioned above.
Status: In work. Based on the first part of the thesis.

Siderostat Pointing: Validation of an advanced line-of-sight pointing concept beyond LISA This publication will be based on Chapter 4.
Status: A submission-ready draft exists.

Appendix C

Launch lock development

In case of a launch lock failure in LISA, retractable launch locks offer the benefit of requiring a reduced angular stroke by the other MOSA to compensate due to a locking at a centered position. This allows for more miniature actuators and better performance due to reduced TTL resulting from parasitic hinge deformations. However, mass tends to be slightly increased, and the design complexity of a retractable launch lock is significantly higher. The paper draft addresses such a mechanism's design, dimensioning, and testing.

Status: Pre-tensioning is underway. The test house needs to perform vibrational load tests, and surface evaluation needs to be performed post-testing. Results need to be added. These tasks will in part be done (as well as the complete design of the pre-tensioning tool) by intern J. Klesse, who will be added as co-author in this case. Author contributions so far are as follows:

- Alexander Sell, Tobias Ziegler, and Frederik Hasselmann invented the concept and submitted a patent application.

- Frederik Hasselmann performed the dimensioning (using analytical calculations as well as FEM simulations for the round, the rectangular, and the final round option), did draw sketches of reduced complexity, defined the surface coatings, and tests, aided in the design of the pre-tensioning tool and wrote the manuscript.

- Alexander Sell performed some of the dimensioning, implemented the CAD of the final design iteration and derived drawings for manufacturing, secured financial means, defined tests, supervised the project, and wrote parts of the manuscript.

- Tobias Ziegler provided advice and aided in finalizing the document.

A fully retractable launch lock that performs a linear motion only

Nils Frederik Hasselmann[1,*], **Tobias Ziegler**[2], **and Alexander Sell**[1]

[1]Airbus Defence and Space GmbH, Future projects and proposals, Friedrichshafen, Germany
[2]Airbus Defence and Space GmbH, Mission and Satellite Chief Engineering, Friedrichshafen, Germany
[*]nilsfrederik.hasselmann@gmail.com

ABSTRACT

We discuss the design of a hold-down and release mechanism that locks up to six degrees of freedom and fully retracts using a linear motion only. While the concept presented reduces the risk of fretting and is simple in mechanical complexity, the retraction is reduced compared to standard approaches. This makes our solution especially interesting for ultra-high precision pointing applications such as the optical angular tracking mechanism for LISA.

Introduction

When devices (mechanisms, robotic arms) are subject to high external mechanical loads for a defined duration (such as shocks and vibration during a rocket launch), a conventional solution is using a hold-down and release mechanism (HDRM) to protect those from damage by fixing them in place; thereby reducing the loads on actuators and joints of the parts that are nominally moving. Of course, the locking must be released to restore the mobility respective function of the device after the loads subside.[1]

Non-retractable HDRMs

Standard applications often require merely the release and clearance in one direction. For these applications, cup-cone form fits, which are held together using the pretension of a single bolt, are used. This bolt typically applies forces in the direction of release, while the form fits convert loads in other directions into forces acting against the pretension provided by the bolt. Such devices are commonly used, for they are simple and can lock up to six degrees of freedom (DOF) if they possess structured surfaces for their form fits. Also, the weight of such a minimalist design is typically on the lower end, making such a solution especially attractive for space applications.

In Figure 1, such an HDRM using a simple cup cone form fit is shown in the locked (a) and released (b) state: In the locked state, the bolt is pre-tensioned using a pre-tensioning nut and applies forces to the form fit such that the device acts as a rigid connection between upper and lower interfaces. In the example, a melt coil of a non-explosive actuator (NEA) can be triggered, resulting in the release of the bolt and pretension and the subsequent extraction of the bolt using a spring: Once the pretension is gone, the form fits no longer present a rigid connection, and the upper interface can move away from the lower interface or vice versa. As one interface is typically static (in our sketch, the yellow cup is bolted to the lower interface), the other interface can only move in one direction, as the other direction remains blocked.

Retractable HDRMs

Suppose the mechanical device to be released shall be able to move in both directions. In that case, an additional support structure and bearings are required, which enable moving the counterpart of the form fit out of the volume envelope required for the proper operation of the previously locked component or system. Conventional approaches typically use joints and springs to perform the retraction and no longer have HDRM components that hinder the nominal motion of the locked device.[2–4] The advantage of obtaining sufficient clearance for the operation of the locked device post-release comes with significant drawbacks in the case of state-of-the-art designs: Increased mechanical complexity, a much larger envelope, and the joint in the load path, which can not sustain substantial

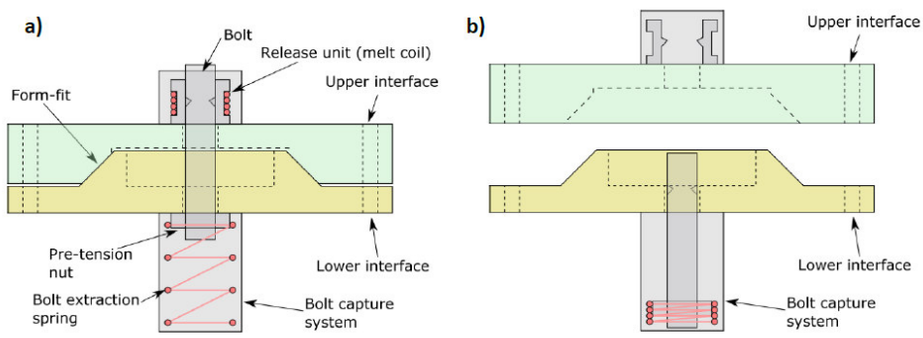

Figure 1. A simple cup-cone form fit is used to convert lateral to axial loads acting against a pretension by a releasable bolt. This is the basis of most non-retractable HDRMs. The locked (a) and released (b) states of the HDRM are shown.

loads, are among those. Also, state-of-the-art are fully retractable HDRMs that possess two sequential form fits and employ a combination of rotation and translation or translation and radial contraction to ensure that parts of the HDRM move out of the way after the release of the locked object.[5,6] These concepts are similar to the one presented here but possess a higher mechanical complexity regarding the motion performed during retraction, and mating surface pairs (for rotating mechanisms) must be able to glide during release. This potentially bears the risk of cold welding due to fretting if vibrational motion occurs.

We detail the design process and testing of a fully retractable HDRM (FR HDRM) that performs a linear motion only, is exceptionally compact and capable of locking up to six DOFs, depending on the detailed design, and is capable of restoring mobility in all DOFs after (electronically triggered) release. At the same time, it is possible to design the mechanism to allow for high loads in all DOFs. However, the retraction and, thus, post-release clearance is limited. Therefore, the proposed HDRM is especially useful for high-precision pointing applications. In contrast to other FR-HDRMs, a fully geometrically constrained design is possible, where those feature one joint or surface mating and must thus rely on static friction or a suitable surface treatment preventing fretting and cold welding.

Concept

The idea behind the proposed HDRM is that well-known and extensively tested principles and technologies are used: Pretension is provided by a typical actuator using a bolt, whose release can be triggered electronically. Form fits act as a rigid connector in the locked state - if the pretension is sufficient. To obtain a fully retractable HDRM performing a linear motion only, two central principles are introduced: Firstly, the usage of two form fits with opposite directions of release that bear the load sequentially. This allows for load capabilities that are as high as for simple, non-retractable HDRMs without increasing the complexity. Furthermore, this approach can also allow for clearance in at least both directions of release, whereas in case of a non-retractable HDRM based on cup-cone form fits at least the direction opposite to that of the release would be blocked. Secondly, using a single bolt and actuator for pre-tensioning and release and a stiff spring element for distributing the pretensions as desired on both form fits is central to our design. These demands are required to obtain competitive reliability (deploying more actuators is highly undesirable) and ensure that manufacturing tolerances do not cause deviations in the distributions of the pretension resulting in critical failure under loads. In Figure 2, the working principle for the design proposed by us is detailed: The parts that shall be locked against each other are bolted to the parts colored yellow and green. The two form fits that bear the loads sequentially, are labeled ’inner-’ and ’outer form fit’. The structure connecting the two form fits is named ’upper disk’. The bolt, release unit, and pre-tension nut are colored grey. The spring element distributing the pretensions as desired onto the two form fits is labeled ’lower disk.’ Upon release, one or more retraction springs can push the upper and lower disk into their resting positions against a mechanical stop. One can

use either the bolt as a guide or dowel pins in case the bolt is cut as part of the release action. The released state is depicted in Fig.2b.

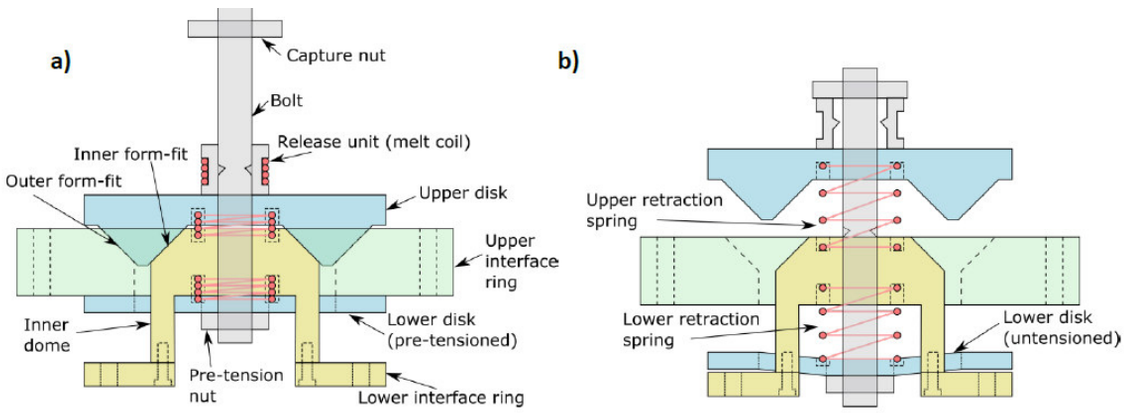

Figure 2. The prototype full retractable HDRM in locked (a) and released (b) state: Yellow and green interfaces are locked against each other and can -to an extent- freely travel with respect to one another upon retraction of the upper and lower disk.

Requirements

For the HDRM to function correctly, the total load acting against the pretension must be smaller than that pretension. Otherwise, the mating surfaces of the form fits can lift and the protection of the locked object from excess loads as well as a release of the HDRM can not be ensured, as vibrational motion may result in cold welding due to fretting. By modifying the stiffness of the lower disk and choosing the appropriate bolt pretension, one can ensure the proper function of the proposed HDRM. Depending on the geometry of the form fits, three to six DOFs can be locked geometrically, and the required pretension is roughly twice that of a non-retractable single form fit HDRM with geometry and the dimensions of the inner form fit. It is also critical that the lower disk does only deform elastically, which may require modifications of the geometry. For the reference use case analyzed here, relevant key requirements such as loads and stiffnesses are summed up in the table below.

Parameter				**Remark**
stiffness	axial (z)	lateral (x,y)	bending (x,y)	from structural mode analysis
	$1 \times 10^7\,\mathrm{N\,m^{-1}}$	$1 \times 10^7\,\mathrm{N\,m^{-1}}$	$1 \times 10^5\,\mathrm{N\,m\,rad^{-1}}$	incl. safety factors
forces (loads)	F_x	F_y	F_z	only quasi-static
	6000 N	12 000 N	6000 N	loads considered
moments	M_x	M_y	M_z	see above
	350 N m	300 N m	0 N m	
shock load	$f_1 = 100\,\mathrm{Hz}$	$f_2 = 1000\,\mathrm{Hz}$	$f_3 = 10\,000\,\mathrm{Hz}$	shock response spectrum (SRS)
emissivity	$\leq$200 m s^{-2}	$\leq$300 m s^{-2}	$\leq$2000 m s^{-2}	amplification factor of 10
clearance	z	r		r is the radial direction
(axial both dir.)	11.0 mm	9.0 mm		asymmetric retraction allowed
envelope	R	h		radius R and height h of
	65 mm	180 mm		a cylinder envelope
mass	$\leq$ 2 kg			with Space Lock 70 kN NEA

Selected analytical considerations in the design process

To allow large loads at relatively low bolt pre-tensioning forces F_B (and thus allow for usage of a smaller, lightweight actuator), a steep angle of the cup cone form fits β is desired to keep conversion of lateral loads F_1 to axial loads F_B to a minimum (Fig.3a):

$$F_B = F_1 \cdot \cos\beta \left(\frac{1}{\sin\beta} - \mu \sin\beta \right) \approx F_1 \cdot \cot\beta = \frac{F_1}{\sqrt{3}}$$

while higher static friction coefficients μ yield a reduction in the required bolt pretensions, one does not want to rely on friction. Therefore the no-friction approximation gives conservative estimates.

However, a steep angle of the form fit may also result in the form fit not being able to disengage without additional forces pulling the form fits apart, as friction forces due to normal forces F_N become larger while downhill forces F_H are reduced. For a given β and μ, the following condition must be fulfilled to ensure that the two counterparts of the form fit can come apart after pretensions were applied:

$$\mu < \sin\beta \cdot \cos\beta \Longrightarrow 1 < \sqrt{3} \Longleftrightarrow \text{true}$$

with $\mu \leq 0.25$ and $\beta = \frac{\pi}{3}$, the parts should come apart without issue, but this also is the reason for not relying on a higher μ for reduction of the required bolt pretension.

From the loads and the geometry of the form fit, we can determine the required bolt pretension for both inner and outer form fits under the conservative assumption that all loads can be fully correlated. As the geometry changes with each design iteration (to reduce mass or increase stiffness), these values are updated for each iteration in the design process. For an inner form fit radius r_{inner} of 33.25 mm, $\mu = 0$, $\beta = \frac{\pi}{3}$ and the loads specified before, the required pretension force is given by (coordinate system according to the right-hand rule):

$$F_{B,inner} = \left(\left(F_x^2 + F_y^2\right) \cdot \cos\beta^2 \left(\frac{1}{\sin\beta} - \mu \sin\beta \right)^2 + \left(F_z + \frac{M_x + M_y}{r_{inner}} \right)^2 \right)^{\frac{1}{2}} = 26.7\,\text{kN}$$

For the outer form fit with $r_{outer} = 46.63$ mm, the required pretension force is 21.4 kN. Higher pretensions without modifications of the geometry of the lower disk result in a further increase in the ratio of the distribution of pretensions $\frac{F_{B,inner}}{F_{B,outer}}$.

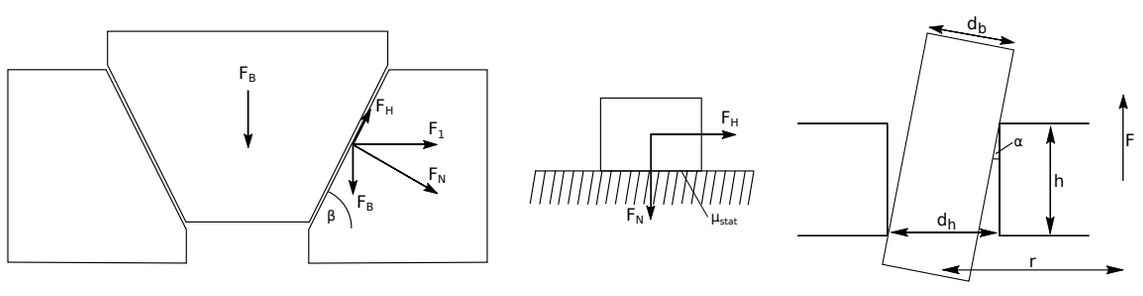

Figure 3. a) Forces due to pre-tensioning acting on a simple cup cone form fit. b) Definition of the static friction coefficient. c) Jamming due to a canting of a pin guided by a drilled hole.

Post-release, retraction springs push the upper and lower spring plates into well-defined final resting positions against three stoppers. During that process, dowel pins guide these parts. In case static friction μ or lever arm r are too high (or the guiding length h is too low), the parts cant and jam while retracting, resulting in partial release only. The condition for the minimal guidance length in case the bolt and hole diameter are well matched ($\alpha << 1$) is given by (see Fig.3c):

$$h \geq 2\mu \cdot r$$

Regarding the guidance of the pre-tensioning bolt, one should point out that the lever arm is very small and that the spring is coiled around the bolt and pushes on both sides of the bolt so that only nondifferential spring forces contribute to the creation of a canting moment while nearly the full spring force is available as downhill force. Nondifferential forces are small as the springs are polished to feature a non-convex line contact over which the force is applied. Therefore, only the three pins for guiding the upper and lower spring plate are considered critical. For a leverarm of $r = 18\,\mathrm{mm}$ and a friction coefficient of better than $\mu = 0.3$, the guidance length should thus be greater than 10.8 mm. Consequently, inserts of length 13 mm made from anodized aluminum and austenitic steel pins are employed to ensure proper guidance and retraction. A guidance length of 11 mm is opted for in the case of the pre-tensioning bolt.

Nummerical simulations

A finite elements model (FEM) containing a full assembly of the FR-HDRM with contact constraints and Coulomb friction pairs for modeling the mating surfaces of the form fits shown in Figure 4a: The deformation when applying a pretension of 50 kN is shown. Smaller deformations are equivalent to a lower energy stored in the system and thus lower shocks during release could be expected when optimizing for higher stiffness. CAD models of the final prototype FR-HDRM are shown in Figures 4b and 4c in locked and released states. Mass estimates, dimensions, and FEM simulations were obtained from or performed using this geometry.

Parameter				**Remark**
stiffness	axial (z)	lateral (x,y)	bending (x,y)	from FEM analysis,
	$2.2 \times 10^8\,\mathrm{N\,m^{-1}}$	$1.6 \times 10^8\,\mathrm{N\,m^{-1}}$	$1.8 \times 10^5\,\mathrm{N\,m\,rad^{-1}}$	driven by bending stiffness
distribution of	inner form fit	outer form fit		from FEM analysis
forces by lower disk	26 800 N	23 200 N		
clearance	z	r		r is the radial direction,
(axial both dir.)	12.0 mm	9.9 mm		asym. retraction
envelope	R	h		radius R and height h of
	63 mm	164 mm		a cylinder envelope
mass	$<$1.6 kg			w. Space Lock 70 kN NEA

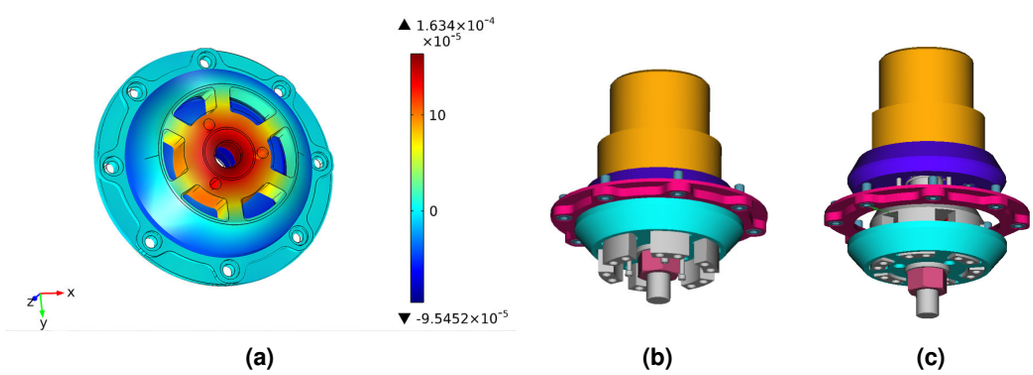

Figure 4. FEM of the volume displacement and contact forces due to pretensions applied by the bolt allow for dimensioning of the lower spring plate for the desired distribution of pretensions. On the right: CAD of the prototype FR-HDRM in locked (b) and released (c) states. Grey and pink parts are locked against one another using the form fits of the upper disk (purple) and pre-tensioning by the NEA (yellow), bolt (grey), and the lower disk for distribution of pretensions (turquoise).

Surface treatment of the formfits

In order to prevent cold welding and fretting of the form-fit surfaces in contact, one should choose a material combination or surface treatment that, ideally, is space-qualified and tested under launch conditions. As part of an ESA-financed activity, Aerospace and Advanced Composites GmbH tested a multitude of different material pairings to investigate suitable combinations and surface treatments. State-of-the-art is oxidizing or hard-coating one of the surfaces in order to avoid direct metal-on-metal contact and using a lubricant such as Braycote 601-EF to provide additional protection in case the hard coating delaminates or is worn down. Also, certain metals are known as solid lubricants not susceptible to cold welding. Here, we opted for the gilding of steel surfaces, oxidizing the titanium counterparts, as well as using Braycote 601-EF as a lubricant.

Testing of the fully retractable HDRM prototype

Initial tests of the FR-HDRM focused on confirming the proper distribution of pretensions on outer and inner form fits. Environmental tests consisting of vibrational loads under representative loads were performed, and the release test was performed while logging shocks.

Assembly and pre-tensioning

Environmental testing, release, and shock

Conclusion

A fully retractable HDRM was proposed, designed and tested by us that is capable of locking up to six DOFs and sustain high loads, while only relying on a linear motion for retraction. The FR-HDRM is based on two parallel cup cone form fits; calculation of the distribution of the pretensioning forces is non-trivial and should be experimentally verified. Polishing of the lower disk, the spring element for applying pretensions, allows adjusting the pretensioning ratio to some extend in order to perform fine tuning if required. Measurements of the SRS show, that the shocks during release are.....

Acknowledgements

We would like to thank the personal of the environmental testing facility for aiding us in setting up the environmental (shaker/ vibrational load tests) as well as advice on placement of the sensors for measuring release shock.

References

1. Davis, T. S., Hadden, S. L. & Jacobs, J. H. Launch lock for spacecraft payloads EP1480878B1 (2006).

2. Langer, M. *et al.* Results and lessons learned from the CubeSat mission first-MOVE. *Small Satellite Missions for Earth Observation, 10th International Symposium, IAA* (2015).

3. Young, K. & Hindle, T. Payload launch lock mechanism EP2450280B1 (2012).

4. Honnen, K. Launch locking device for the SEVERI scan assembly. *8th European Space Mechanisms and Tribology Symposium Bibcode: 1999ESASP.438..191H* **438**, 191 (1999).

5. Barber, T. D., Young, K. & Hindle, T. Launch lock assemblies with reduced preload and spacecraft isolation systems including the same US9475594B2 (2016).

6. Bursi, A. *et al.* MWI launch locking device (LLD), a not standard HDRM. *Proc. 18. European Space Mechanisms and Tribology Symposium 2019* (2019).

Appendix D

Optimization of temperature sensors

Thermal noise is one of the major noise contributors in LISA. Characterization of excess thermal noise (due to the dissipation of active components) is critical for the mission's success. For measurement bands extending to low frequencies beyond 10 mHz, the noise performance of resistive (temperature) measurements is limited by technological noise.

To allow measurement performance to be not limited by flicker noise, the choice in the package and the characterization of the components used plays a critical role. The paper discusses improvements to the thermal diagnostics of LISA or any resistive low-noise measurement relying on Wheatstone bridge-type transducer circuits.

Status: Under review by the co-authors, approaching submission-readiness.

Author contributions are as follows:

- Frederik Hasselmann conceived the ideas leading to the investigation, designed, built, and programmed the test setups, wrote the scripts for data evaluation, and recorded and evaluated portions of the data. He created the PCBs for component testing, performed thermal simulations, wrote the first draft, and iterated versions.

- Alexander Sell supervised the project, provided advice, performed an evaluation of the data, and wrote on the manuscript.

- Jonathan Klesse performed soldering of many components tested, refined scripts for data evaluation, and recorded data according to the test plan defined by Frederik Hasselmann and Alexander Sell.

Minimization of flicker noise in resistive (μK-level temperature) sensors

Nils Frederik Hasselmann[1,*], **Jonathan Klesse**[1], **and Alexander Sell**[1]

[1]Airbus Defence and Space GmbH, Advanced Projects Germany, Friedrichshafen, Germany
[*]nilsfrederik.hasselmann@gmail.com

ABSTRACT

We characterize and model the noise of electrical components in precision temperature sensing circuits. To this end, a simple shielding is required for obtaining ultra-stable thermal environments and the selection of components enabling temperature noise measurements with a noise floor better than $10\,\frac{\mu K}{Hz^{1/2}} \cdot \left(1+\left(\frac{2.8\,mHz}{f}\right)^4\right)^{\frac{1}{2}}$ at frequencies between $0.1\,\mathrm{mHz}$ and $1\,\mathrm{Hz}$ are discussed. Special attention is paid to the proper choice of package for reference resistors yielding minimal flicker noise and the characterization of NTC thermistor flicker noise.

Introduction

Metrology and other ultra-high precision applications demand environmental conditions that are stable enough to allow performing the desired task without adding noise via coupling of temperature fluctuations to the observed quantity. A prominent example is the Laser Interferometer Space Antenna (LISA), where temperature noise directly couples into apparent path length fluctuations via thermal expansion of the materials used in the instrument.[1] Thus, measurement of the temperature fluctuations is crucial for validating shielding concepts, measuring noise due to dissipation, or removing thermal noise contributions using a calibration.[2,3] However, thermistors, as well as resistors serving as a reference, often are not specified regarding the technical noise at all or merely a typical upper and lower bound for the respective type of technology is known. Therefore, the experimental characterization of this type of noise may be critical concerning system performance at low frequencies.[4,5] In addition, little attention has been paid to the role of the package size, respective to the scaling of flicker noise with the geometry of the resistive film, even though the scaling of current noise with resistor geometry has been known for decades.[4,6–8] Here, we highlight an improvement in flicker noise by more than one order of magnitude solely by choosing the package according to a simple analytical model.[9] Furthermore, we detail and systematically perform the characterization of NTC thermistor flicker noise for various current NTCs with lead wires with a special focus on the elimination of parasitic noise contributions such as that of the voltage references typically used in the excitation of the Wheatstone bridges and residual thermal noise.[10]

Thermal shielding

First, a simple procedure for designing thermal shielding for a testbed that can be used to validate the performance of the measurement electronics and the sensor components is introduced. In addition to using common mode suppression of temperature-induced fluctuations, a suitable thermal shielding concept is required to obtain a sufficiently stable thermal environment for testing the sensors' performance. An effective minimalist design is based on onion-like shielding with alternating layers of materials with poor conductivity and negligible thermal mass and layers with large thermal mass and ideal conductivity. In our scenario, only small gradients in temperature exist, and we can assume that heat transfer is governed solely by radiative and conductive-diffusive processes while convective processes are negligible. Heat transfer is thus described using grey body interaction and the Fourier law using finite

differences. The temperature evolution for the n-th reservoir and the $j+1$-th time step is then given by:

$$T_{n,j+1} = T_n + \frac{dt}{c_n \cdot m_n}\left[\sigma\left(-A_n\left(T_n^4 - T_{n+1}^4\right) + A_{n-1}\left(T_{n-1}^4 - T_n^4\right)\right) - \lambda_{n,n+1}\left(T_n - T_{n+1}\right) + \lambda_{n-1,n}\left(T_{n-1} - T_n\right)\right]$$

with areas A_n modified to $\tilde{A_n}$ for the case of two grey body surfaces facing each other forming an enclosure:

$$\tilde{A_n} = \left(\frac{1-\varepsilon_{n,i}}{A_n \cdot \varepsilon_{n,i}} + \frac{1-\varepsilon_{n+1,o}}{A_{n+1} \cdot \varepsilon_{n+1,o}} + \frac{A_{n+1}+A_n}{A_{n+1} \cdot A_n}\right)^{-1}$$

where c_n is the specific heat capacitance of the n-th layer, m_n the mass, T_n the temperature at time step j and σ the Stefan–Boltzmann constant. The conductivity between layer n and layer $n+1$ is $\lambda_{n,n+1}$, $\varepsilon_{n,i}$ is the emissivity of the inner surface and $\varepsilon_{n,o}$ the of the outer surface of the n-th layer and dt the time step. The boundary condition is the temperature of the environment, which can be modeled or measured. In case multi-layer insulation is used in experiments under vacuum conditions as a radiation barrier, the interaction between layers is described by the Lockheed-Martin equation.[11]

Experimental setup

The experimental setup consists of the measurement electronics that excite and read out a temperature sensor based on a Wheatstone bridge and the thermal shielding providing an ultra-stable environment.

Measurement electronics

An eight-channel measurement board that excites Wheatstone bridges with an AC voltage signal (amplitude 2.5 V) and reads out the differential voltage of the bridges using a 24-bit sigma-delta analog-digital converter (with a field programmable gate array for subsequent data processing) is employed for the noise measurements shown. AC excitation is derived from the reference voltage provided to the ADC. The bridge is read out using a two-wire measurement.

Thermal isolation

Expanded polystyrol (EPS), Neopor, and air were used for thermal insulation materials. As reservoirs, aluminum sheet metal was used due to its high specific heat capacitance, low weight, and low price. The setup consists of an EPS box lined inside with aluminum sheet metal; in the center of the box, an aluminum cylinder sits on a block of Neopor. The setup thus acts as a second-order lowpass. The lab is actively stabilized with an in-loop peak valley noise of 50 mK. For NTC characterization measurements, the previous setup was lined with aluminum plates and placed in a large Styrofoam box to obtain even further attenuation of ambient noise, and a block of increased thermal mass replaced the innermost heat reservoir (aluminum cylinder). Simulation parameters can be found in the appendix. It is critical that cables are well coupled to each thermal reservoir using thermal anchoring to avoid thermal bridges from the outside to the inner layer.

Selection of components for the sensor

Components are selected by placing a Wheatstone bridge with the components to be tested in the ultra-stable thermal environment and using common mode suppression of residual temperature-induced noise to evaluate the contributions of electrical noise to the measurement of temperature fluctuations. A sensor bridge is equipped with four reference resistors to quantify the combined behavior of reference resistors and front-end electronics. For regular measurement of temperature fluctuations, one of the reference resistors is replaced by a thermistor, and for evaluation of the technological noise of the thermistor, one voltage divider of the Wheatstone bridge is equipped with two thermistors. If the technological noise of the thermistor is similar to that of the reference resistors, the Wheatstone bridges are equipped with 4 thermistors. In all scenarios, the thermistors of one bridge are placed next to each other, in ridges machined in the aluminum block, representing the innermost layer of the thermal shielding covered in heat transfer compound paste.

Results

Thermal noise measurements

Fig.1a shows data from two regular sensors placed this way. The differential data confirms a common mode suppression of ≈ 200. A suppression greater than ≈ 1000 is obtained using a transducer with two NTCs. Amplitude noise spectra recorded with individual transducers (equipped with either TS-NTC-833 or B57861S0503F040 NTCs and TE RN73 105 kΩ or 60.4 kΩ reference resistors) placed outside the insulation as well as on the innermost layer (L2) quantitatively confirm the expected suppression of ambient noise, as shown in Fig.1b. The pink and bright green curves indicate the total technical noise. At frequencies above 0.5 mHz, the thermal stability of the environment, in conjunction with the common mode suppression of that residual thermal noise in differential measurements, allows the determination of the contributions of electrical noise. Technological noise of the reference resistors is a typical limitation: While contributions of the front-end electronic as well as the voltage reference and parasitic thermocouples can be avoided by using an AC excitation of the bridge as well as ratiometric measurement schemes and chopper stabilized zero-drift op amps, the technological noise of the reference resistors and NTC as well as the Johnson Nyquist noise of these components can not be removed in post-processing or avoided.

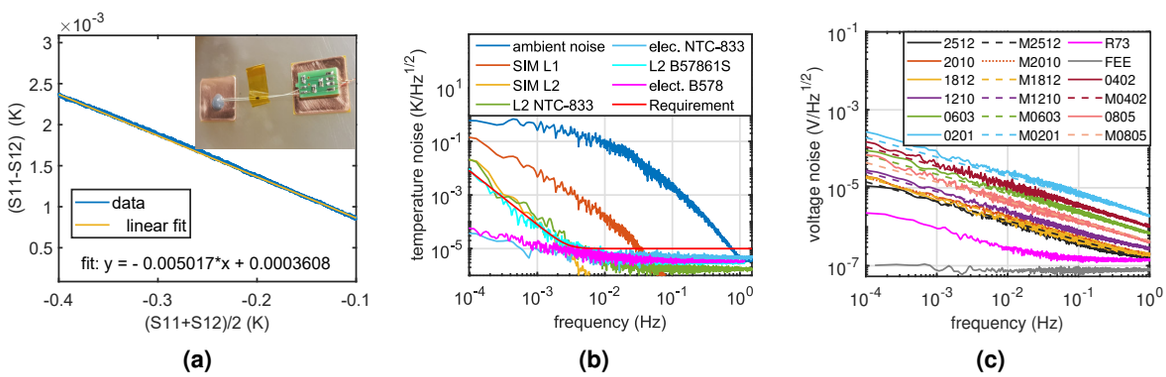

Figure 1. a) Common mode suppression of temperature changes when sensors are placed next to one another on an aluminum block - plotted is the differential change in temperature versus the average change in temperature; the insert shows a regular sensor. b) Thermal performance of the sensor testbed and sensors compared to simulations of the different thermal layers (L1: outer, L2: inner, SIM: simulation based on ambient measurement). c) Flicker noise for six packages of Panasonic ERJ thick-film resistors compared to the modeled scaling of noise with package (M indicates modeled curves), and RN73 thin film resistor as well as FEE performance.

Selection of components for the transducer circuit

While the characterization of technological noise of various resistor types and a few NTCs was performed for experiments at LIGO as well as for usage in radiometers, the impact of the package on technological or current noise was so far not given special attention.[4–6, 12] Thick film resistors exhibit a higher noise level than thin film or Z-foil resistors. They thus are an excellent choice to demonstrate this geometry-dependency within short measurement times in addition to featuring a relatively simple film geometry. In Figure 1c, the voltage noise amplitude spectral density measured is plotted versus the frequency for various packages for both experimental data and the model with the area of the resistive film derived from microscopy images (see appendix). As expected, larger packages produce lower levels of technological noise: The flicker noise scales roughly with the inverse of the square root of the package area.[9] The noise of instrument amplifiers and ADC (making up the FEE, grey) was shown to be white for highly balanced bridges in a separate measurement (by connecting both differential inputs of the instrument amplifiers to the center tap of voltage dividers making up the reference of the Wheatstone bridge), and noise contributions by the excitation of the bridges were ruled out by comparison of measurements using highly balanced (pink) and unbalanced (blue) bridges equipped with low noise reference resistors (RN73 TE, 0805 package, 4x

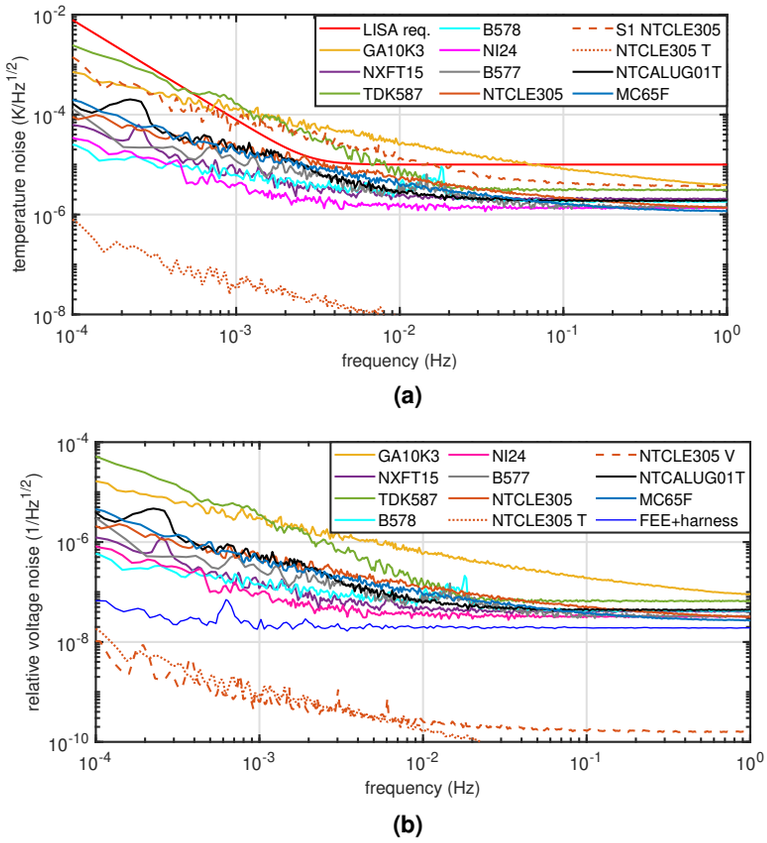

Figure 2. a) Flicker noise contribution of various NTCs to thermal noise measurements considering the different β-values. b) Same data as in a) in terms of relative voltage noise. Also shown are auxiliary measurements regarding contributions of the harness and FEE for the two-wire scheme (limiting measurement performance) and the noise of a regular sensor (S1) as well as residual contributions of thermal (T) and voltage reference noise (V).

59 kΩ, or 3x59 kΩ and 1x 66.5 kΩ).[3] Measurements of technological noise of NTC thermistors require verifying the attenuation of the ambient noise and the common mode suppression obtained. Attenuation of ambient noise can be validated as above using a regular sensor, and a linear correlation of the average of the signal of 7 sensors with that of the regular sensor yields the linear coupling factor obtained for the common mode suppression. Multiplication of that factor with the thermal noise gives the contribution of residual thermal noise to the noise measured. As the balance of the Wheatstone bridges equipped with four NTCs depends on the tolerances of the individual NTCs, the sign of the differential bridge voltage may be chosen arbitrarily. Ideally, one opts for a combination such that adding all time-averaged bridge voltages results in zero value. This eliminates fully correlated noise, such as excitation voltage noise, whereas technological noise is unaffected. Instead of merely modifying the signs and looking for a combination that on average gives the minimal bridge voltage, one could average over half of the sensors each and modify the prefactor to obtain a zero bridge voltage, but this would complicate the breakdown to bridge level and component level noise later on and yield only a slight improvement in suppression of correlated noise. The relationship between relative voltage noise and relative resistance noise in a measurement of a single bridge is given by $\delta V/V = \delta R/(2R)$.[12] Residual noise is present, as the ADC reference voltage is not identical to the excitation voltage of the bridge measured using a two-wire scheme, but only the reference voltage from which the AC excitation is derived. As technological noise is not correlated between components or different bridges, the noise of a single

resistive bridge is inferred by the multiplication of the square root of the number of bridges with the averaged bridge relative bridge voltage noise. Contributions of thermal noise, excitation voltage noise as well as harness and FEE noise are shown in Figure 2 in addition to technological noise measurements of various NTCs.

Conclusion

Component selection necessitates actual testing for ultra-low noise applications, such as high-precision temperature measurements: Typically, no technological noise is specified for NTC thermistors. The same is often true for the reference resistors in the transducer bridge circuit and preamplifier circuits. We demonstrated a procedure to measure the contribution of technological noise experimentally and characterized various NTC thermistors by systematically eliminating parasitic noise, such as reference voltage and residual thermal noise. Specific thin film resistors (RN73 by TE) and (Z-)foil resistors (Vishay-Dale and Susumu) have a current noise performance specified in their datasheet and feature excellent stability regarding temperature drifts. If one seeks the lowest current noise possible, one should use the largest package available and verify the NTC performance experimentally, using a suitable setup. Ultimately, the noise level using resistive temperature measurements at room temperature can be limited to Johnson-Nyquist noise, which, in turn, is decided by the trade-off between allowable noise introduced due to self-heating (heavily affected by coupling to the environment) and dissipation of the sensor.

Acknowledgements

The authors would like to acknowledge funding by the German BMWi via DLR grant 50OQ1302.

References

1. Armano, M. *et al.* Temperature stability in the sub-milliHertz band with LISA pathfinder. *Monthly Notices of the Royal Astronomical Society* 3368–3379 (2019). DOI 10.1093/mnras/stz1017.
2. Higuchi, S. *et al.* Design of a highly stable and uniform thermal test facility for MGRS development. *Journal of Physics: Conference Series* 012037 (2009). DOI 10.1088/1742-6596/154/1/012037.
3. Sanjuán, J. *et al.* Thermal diagnostics front-end electronics for LISA pathfinder. *Review of Scientific Instruments* 104904 (2007). DOI 10.1063/1.2800776.
4. Seifert, F. Ligo document t0900200-v1: Resistor current noise measurements (2009).
5. Roma-Dollase, D. *et al.* Resistive-based micro-kelvin temperature resolution for ultra-stable space experiments. *Sensors* 145 (2023). DOI 10.3390/s23010145.
6. Walter, D., Bülau, A. & Zimmermann, A. Review on excess noise measurements of resistors. *Sensors* 1107 (2023). DOI 10.3390/s23031107.
7. Vandamme, L. K. J. Criteria of low-noise thick-film resistors. *Active and Passive Electronic Components* **4**, 171–177 (1977). DOI 10.1155/APEC.4.171.
8. Hooge, F. N. $1/f$ noise is no surface effect. *Physics Letters A* **29**, 139–140 (1969). DOI 10.1016/0375-9601(69)90076-0.
9. Kuo, C. & Blank, H. The effects of resistor geometry on current noise in thick-film resistors. *1968 International Hybrid Microelectronics Symposium* (1968).
10. Gu, L. *et al.* Study on the voltage reference noise at sub-millihertz frequencies for developing an ultra-stable temperature measurement subsystem. *Sensors* (2023). DOI 10.3390/s23104611.
11. Keller, C. W., Cunnington, G. R. & Glassford, A. P. Thermal performance of multilayer insulations (1974).
12. Ryger, I. *et al.* Noise characteristics of thermistors: Measurement methods and results of selected devices. *Review of Scientific Instruments* 024707 (2017). DOI 10.1063/1.4976029.

Appendix

Thermal performance simulation parameters The table below specifies the parameters used in the simulations of ambient temperature noise suppression by the regular and upgraded shielding.

Parameter	Regular	Upgraded	Comment
$\lambda_{0,1}$	$0.68\,\mathrm{J\,K^{-1}}$	$0.576\,\mathrm{J\,K^{-1}}$	effective; from geometry and material
$\lambda_{1,2}$	$0.22\,\mathrm{J\,K^{-1}}$	$0.68\,\mathrm{J\,K^{-1}}$	see above
$\lambda_{2,3}$	-	$0.22\,\mathrm{J\,K^{-1}}$	see above
$c_1 \cdot m_2$	$6070\,\mathrm{J\,K^{-1}}$	$54\,000\,\mathrm{J\,K^{-1}}$	aluminium box
$c_2 \cdot m_2$	$3240\,\mathrm{J\,K^{-1}}$	$6070\,\mathrm{J\,K^{-1}}$	see above
$c_3 \cdot m_3$	-	$16\,572\,\mathrm{J\,K^{-1}}$	aluminium blocks
A_1	$0.8332\,\mathrm{m^2}$	$1.4780\,\mathrm{m^2}$	measured
A_2	$0.0675\,\mathrm{m^2}$	$0.8332\,\mathrm{m^2}$	see above
A_3	-	$0.1730\,\mathrm{m^2}$	see above
$\varepsilon_{1,i} = \varepsilon_{2,i}$	0.1	0.2	emissivity aluminum sheet box
$\varepsilon_{2,o} = \varepsilon_{3,o}$	0.1	0.2	degree of oxidization
dt	0.322 s	0.322 s	sampling rate of data

NTC thermistor information The full manufacturer NTC thermistor identification numbers are given below:

Sensor ID short	Sensor ID manufacturer	Comment
GA10K3	GA10K3MCD1	-
NXFT15	NXFT15XH103FA2B100	-
TDK587	B58703M1103A00	-
NI24	NI24NA0103	-
B578	B57863S0103	10 kΩ and 50 kΩ versions tested
NTCLE305	NTCLE305E4103SBA	-
NTCALUG01T	NTCALUG01T103G400	-
MC65F	MC65F103A	-
NTC833	0365 0078 (TS-NTC-833)	-

Resistor film area information The dimensions of the resistive film of ERJ-series thick-film 10 kΩ resistors, measured using an optical microscope, are listed below. The geometry of the L-cuts was measured but not taken into account for the calculation of the relative current noise (e.g., using a Schwarz-Christoffel transformation); the film thickness is about 7 µm and determined using microscope images of polished crosssections.

	Film (µm)		**L-cut** (µm)				
Package	**length**	**width**	**width**	**length**	**distance**	**area** ($\mathrm{mm^2}$)	**rel.** $1/f$ **noise**
0210	360	180	60	80	100	0.065	13.75
0402	600	290	85	90	185	0.17	8.39
0603	1000	500	200	175	300	0.50	4.95
0805	1180	950	390	240	400	1.12	3.30
1210	1940	2000	550	200	800	3.88	1.78
1812	3250	2300	670	630	990	7.48	1.28
2010	3600	2000	760	960	1000	7.20	1.30
2512	4900	2500	870	850	1000	12.25	1

Appendix E

Active thermal control for LISA

For the same reason ultra-low noise resistive temperature sensing is required in inter-satellite range applications such as LISA, active thermal control schemes were investigated within the scope of the cross-validation of the linear heaters used in Grace-FO for missions such as NGGM, Grace-3, and LISA. Investigations included the usage of TECs and conventional Kaptop heaters as actuators and various placement strategies for heaters. Using the breadboard discussed in the paper draft below, the predictions of the custom software used at Airbus Defence and Space were verified to allow for accurate predictions of active thermal control performance.
Author contributions to the work presented are as follows:

- Frederik Hasselmann conceived the experiments, designed and implemented the test setup, performed testing as well as data analysis, defined test plans, and discussed simulations with Erik Hailer. He evaluated the data and wrote the manuscript's main body (only shown here).

- Erik Hailer conceived the experiments, assisted in implementing portions of the test setup, and performed the simulations. He wrote parts of the section on the simulations in the main body and most of the appendix.

- Johannes Burkhardt provided expert input for thermal simulations and contributed input to the manuscript.

- Alexander Sell designed linear heater control electronics and assisted in the implementation of parts of the setup. He also provided expert advice.

Active thermal control for ultra-stable satellite instrument boxes

Nils Frederik Hasselmann[1], **Erik Hailer**[1,*], **Johannes Burkhardt**[1], **and Alexander Sell**[1]

[1]Airbus Defence and Space GmbH, Friedrichshafen, Germany
[*]erik.gottfried.hailer@airbus.com

ABSTRACT

We discuss the active thermal control of a satellite instrument unit box for obtaining ultra-stable thermal environments and the choice of electronics, components, and methods enabling suppression of temperature noise by up to two orders of magnitude in a frequency range between 0.1 mHz and 1 Hz.

Introduction

One reason for performing experiments in space is that high-precision measurements require environmental conditions that are stable enough to allow achieving the objective (such as the detection of gravitational wave) by avoiding excess noise due to coupling of temperature fluctuations, variations in gravity, seismic noise or other disturbances to the observed variable.[1–4] As a prominent example, the Laser Interferometer Space Antenna (LISA) may serve, where temperature fluctuations directly couple into apparent path length noise due to the thermal expansion of the telescope or also indirectly by degrading the frequency stability of the cavity the laser is stabilized (e.g., due to thermal expansion of the spacer separating the mirrors of the optical cavity).[5] Thus, achieving high levels of thermal stability is crucial so as not to compromise instrument performance.[6,7] However, active thermal control in satellite applications suffers from poorly located heaters of small areas (resulting in large gradients, excessive delays, and spatially varying suppression of noise), overly simple control schemes such as bang-bang-controllers as well as sensors featuring poor noise performance used in the controls' feedback.[8,9] Here, we use a combination of sensors developed within the frame of the LISA mission and improved electronics for driving flight models of the heaters used in Grace-FO to stabilize a dummy unit box that is disturbed by temperature fluctuations of the radiator to space, which is mimicked using a cold plate. In doing so, we cross-valid the Grace-FO heaters for LISA and NGGM, respectively, Grace-3.

Methods

This section discusses the experimental setups and components used and the numerical simulations performed.

Experimental setup

The experimental setup aims to mimic the following scenario: An unit box respective unit is stabilized, containing an instrument susceptible to temperature fluctuations while at the same time dissipating power and thus creating excess heat that needs to be removed to allow operation at a nominal temperature. A typical example could be a laser stabilized in an optical cavity. A radiator is mounted on the opposite side of the satellite interface panel the box is mounted on - to dispel the excess heat to space. Especially in the case of low planetary orbits, the radiators and instrument units may experience significant temporospatial fluctuations in temperature, for example, due to a combination of changes in the albedo of the planet's surface and the satellite's attitude. To re-enact this scenario, we use a temperature-controlled, water-cooled cold plate as a dummy for a radiator to space, on which a CFRP-Aluminium honeycomb satellite interface panel is placed, on which, in turn, an aluminum block is mounted. The unit box is represented in the breadboard by this block and is also referred to as the 'dummy unit.' It constitutes an aluminum plate with similar thermal mass and dimensions properties. For active control, a large Kapton foil

heater or a sandwich of TEC elements between thin aluminum sheets is added underneath the unit dummy, such that the temperature of the interface to the unit box may be kept stable, shielding the unit from temperature fluctuations of the radiator to space while at the same time allowing for a heat flux to space. The top of the dummy unit is covered in MLI to capture and spread heating from the compensation heaters and decouple the dummy box from the radiative environment. The setup is placed in a vacuum chamber with a plexiglas lid during tests. Details regarding the temperature measurement electronics, linear heaters (Kapton heater mats placed next to their MOSFET-based drivers to capture waste heat and obtain a linear response or TECs), and the thermo-electric control setup employed can be found in the appendix, as well as temperature sensor noise performance data, the geometry of the components, their making and material properties etc..

Simulations

The simulations shown in the following are based on a lumped parameter model (TMM LPM), where the view factors for radiative heat transfer were determined using the geometric mathematical model (GMM). The TMM LMP was linearized around a thermal steady state point and transformed into the frequency domain using the Laplace transformation. The dynamic behavior, including the heater control, is modeled directly in the frequency domain using complex transfer functions. The assumptions made and their validity are discussed in the appendix. Also given in the appendix is detailed information regarding the GMM (dimensions of the geometries, mesh,...). Included are all components described in the experimental setup section as well as the vacuum chamber with its plexiglas lid, which the setup is placed in during tests. Temperature profiles fed to the simulation are based on low-pass-filtered flight data such that the TEC control loop of the cold plate with its low bandwidth can imprint the profile with high fidelity.

Results

The following will discuss the outcome of the experiments and the corresponding simulations.

Experimental validation of the simulation

A classical Kapton heater mat matched in its area to that of the interface of CFRP-Alu-honeycomb panel and dummy unit is used as the primary thermal actuator, supplemented by a combination of 4 smaller Kapton mats and the driver circuit as a secondary linear heater (capturing waste heat by using the MOSFET-based circuit as part of the heater). As the share of power output of MOSFET and Kapton heaters is dependent on the total power output, choice of temperature set point and placement of the components both can be used as parameters in fine-tuning of the performance later on. At first, the simulation results, while close to the experimental data, did not display an asymmetry in terms of laterally different temperature fluctuations present in the experiment: While the performance of the out-of-loop sensor (OOL2), placed directly next to the -in-loop-sensor (IL) in the center of the instrument, is naturally better than to be expected for more distant sensors (OOL1/3) in case of local variations due to the boundary conditions (in a finite setup), the different response of OOL1 and OOL3 was at first not well understood. One OOL sensor featured residual perturbations in-phase with the disturbance imprinted on the radiator dummy, while the other OOL sensor displayed an overcompensation such that a small out-of-phase perturbation was introduced. Investigations revealed that the contact conductance between cold-plate and CFRP mediated by a silicone-free heat transfer compound was the root cause of the deviation between the experiment and simulation: In the simulation, the contact conductance was assumed to be uniform, while the heat transfer compound did not spread as intended and failed to yield a gap-filling layer providing a highly uniform conductance area density. After adopting a non-uniform contact conductance as observed in the experiment, the simulation results are in excellent agreement with the experiment. Possibly because of the ridge machined into the dummy unit for placing IL and OOL2, the compensation heater mounted on top had to be tuned to add a small portion of the amount injected at the interface level to prevent an overcompensation at the locations of OOL1/3. Simulation and experiment show an excellent agreement and proof that suppression of thermal noise by more than two orders of magnitude is possible for low frequencies within the control bandwidth. The following design rules can be derived from the lessons learned:

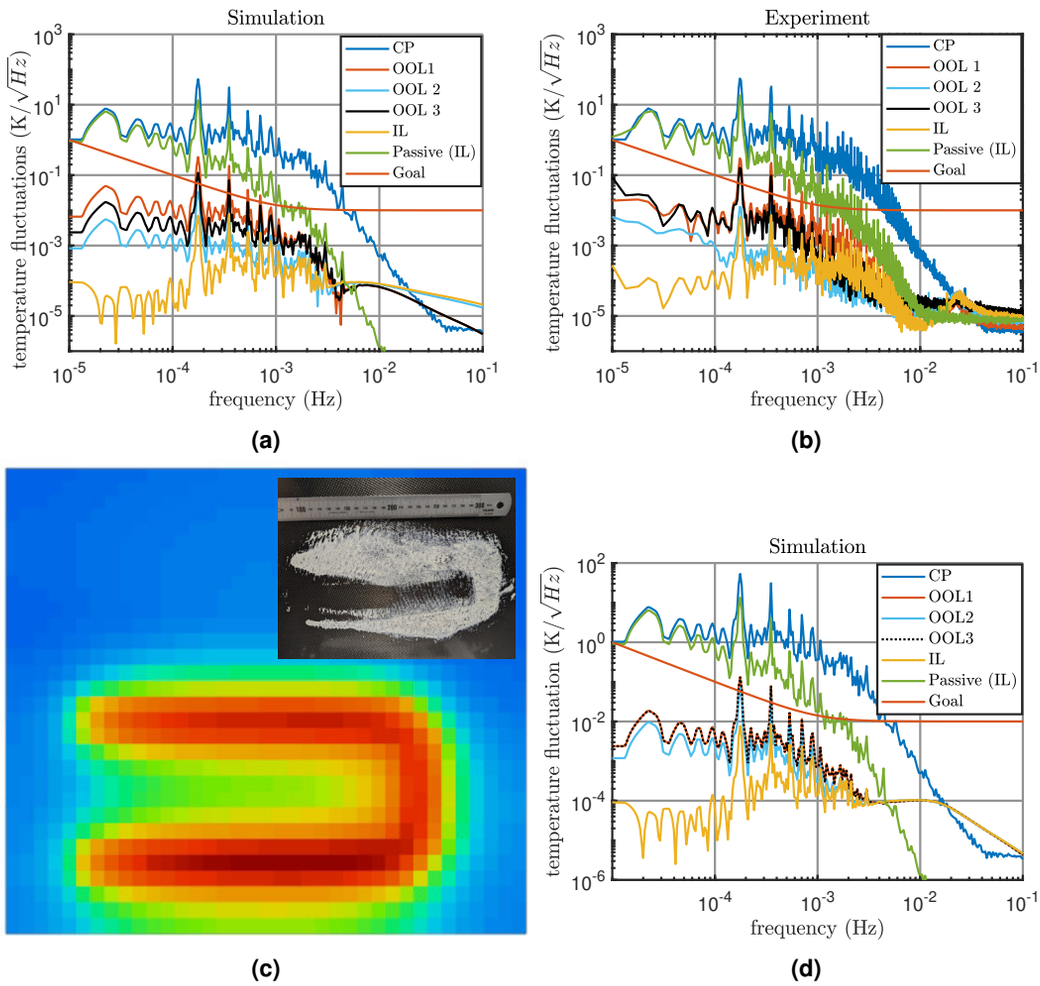

Figure 1. a) Simulation results predicting the temperature fluctuations for the inhomogeneous contact conductance as observed in the experiment: Comparing PI compensation to non-compensated baseline allows quantifying the impact of the active control on the system b) Experimental results allow for the same approach in the lab: Temperature fluctuation data can be used to compare the PI compensated option to the non-compensated baseline. c) Fluctuations injected considering a U-shaped contact conductance modeled according to heat transfer compound paste coverage (see inserted photo). d) Simulation results for homogeneous contact conductance do not show the different behavior of the out-of-loop sensors and are of limited use for tuning system parameters such as heater power share and positioning in the experiment.

- Minimize the number of fitted parameters in the simulation by using experimental or datasheet values as much as possible.
- When using correlations from experimental data, sensor calibration is critical: First, calibrate to the average value they give or a known standard (in an iterative fashion in terms of both slope and offset). Failure to do so will result in flawed values from the correlation.
- Make sure to use sensors with sufficient resolution and noise performance, and always place out-of-loop sensors when testing control loops at various locations.

- Avoid poorly defined contact conductances and boundary conditions by design. Poorly contacted sensors or line contacts are often not considered or can not be measured and will compromise the effectiveness of active control due to spatial variations (in actuator gain and even modulate noise onto the box with the opposite phase to the disturbance).
- When a disturbance is introduced to a sensitive unit via a surface, measure and control the temperature of this surface; ideally on the entire interface. Placing sensors and heaters away from the interface that needs to be controlled results in spatially inhomogeneous suppression and/or modulation of noise onto satellite sections.

Conclusion

Thermal stability requirements are often imposed on unit boxes sensitive to temperature fluctuations and performance improvements using active thermal control are critical to obtain high stabilities in case a large dissipation is expected, preventing usage of passive measures that would come at the expense of higher system mass. To ascertain what performance levels can be achieved without being limited by the performance of standard sensors and actuator placement as well as the lack of knowledge regarding contact conductances, detailed geometry, and boundary conditions, we tested active thermal control using a simple PI controller in conjunction with ultra-low noise temperature measurements as feed-back and custom control electronics driving linear heaters. The control strategy implemented here proves highly effective with suppression of noise by more than two orders of magnitude. Together with the successful cross-validation of the linear heaters, the validation of the modeling techniques will benefit the successful implementation of active thermal control schemes in the context of LISA and Grace-3/NGGM.

Acknowledgements

The authors would like to acknowledge funding by the German BMWi via DLR grant 50OQ1302.

References

1. Ryger, I. *et al.* Noise characteristics of thermistors: Measurement methods and results of selected devices **88**, 024707 (2017). DOI 10.1063/1.4976029.

2. Ferreiro-Vila, E. *et al.* Micro-kelvin resolution at room temperature using nanomechanical thermometry. *ACS Omega* **6**, 23052–23058 (2021). DOI 10.1021/acsomega.1c02045.

3. Peyrou-Lauga, R. & Bruno, G. CHEOPS (CHaracterising ExOPlanet satellite) thermal design and thermal analysis (2015).

4. Luo, J. *et al.* The first round result from the TianQin-1 satellite. *Classical and Quantum Gravity* **37**, 185013 (2020). DOI 10.1088/1361-6382/aba66a.

5. Armano, M. *et al.* Temperature stability in the sub-milliHertz band with LISA pathfinder. *Monthly Notices of the Royal Astronomical Society* **486**, 3368–3379 (2019). DOI 10.1093/mnras/stz1017.

6. Higuchi, S., Sun, K.-X., DeBra, D. B., Buchman, S. & Byer, R. L. Design of a highly stable and uniform thermal test facility for MGRS development. *Journal of Physics: Conference Series* **154**, 012037 (2009). DOI 10.1088/1742-6596/154/1/012037.

7. Sanjuán, J., Lobo, A., Nofrarias, M., Ramos-Castro, J. & Riu, P. J. Thermal diagnostics front-end electronics for LISA pathfinder. *Review of Scientific Instruments* **78**, 104904 (2007). DOI 10.1063/1.2800776.

8. Sundu, H. & Döner, N. Detailed thermal design and control of an observation satellite in low earth orbit. *European Mechanical Science* **4**, 171–178 (2020). DOI 10.26701/ems.730201.

9. Amann, M., Gross, M. & Thamm, H. The grace follow-on quiet electrical power system. *E3S Web of Conferences* **16**, 13011 (2017). DOI 10.1051/e3sconf/20171613011.

Appendix

Experiment setup details:

Aluminum honey comb - CFRP panel properties:

Parameter	Value
Honeycomb core	CRIII-3.1-3-16-001P-5056 h=28 mm
Glue (core-cover sheets)	Hysol EA 9323
Cover sheet fiber	5HS-YSH70A-140 g m^{-2}
Cover sheet resin	LY556/HY906/DY070
Layer stacking	0/90, ±45, ±45, 0/90, 0/90, ±45, ±45, 0/90
Outer dimensions (l·w·h)	470 x 420 x 30 mm^3

Optical properties:

Parameter	Value	Comment
$\varepsilon_{\text{vacuum chamber}}$	0.05	The emissivity of the internal surface of steel vacuum chamber
$\varepsilon_{\text{plexiglass lid}}$	0.9	The emissivity of the test setup facing plexiglass lid of vacuum chamber
$\varepsilon_{\text{coldplate}}$	0.2	The emissivity of the cold plate surface (aluminum)
$\varepsilon_{\text{CFRP facesheet}}$	0.8	The emissivity of the CFRP Honeycomb face sheet
$\varepsilon_{\text{unit dummy}}$	0.2	The emissivity of the aluminum dummy unit
$\varepsilon_{\text{VDA MLI}}$	0.05	The low emissive surface of VDA MLI

Geometric dimensions:

Parameter ($l \times w \times d$)	Value (m^3)	Comment
Vacuum chamber	$0.8 \times 0.8 \times 0.4$	Vacuum chamber (internal)
Cold plate	$0.4 \times 0.64 \times 0.004$	Temperature-controlled cold plate
Honeycomb	$0.42 \times 0.47 \times 0.03$	Interfacing cold plate and dummy unit heater
Interface kapton heater	$0.3 \times 0.47 \times 0.0002$	Interfacing dummy unit and honeycomb panel
dummy unit	$0.3 \times 0.47 \times 0.02$	dummy unit glued on top of the Kapton heater

TMM analysis parameters (contact conductances were obtained from correlation of model and experiment):

Parameter	Value	Comment
Honeycomb heat capacity	1015 J K^{-1}	Capacity of the Honeycomb Panel
Instrument heat capacity	7157 J K^{-1}	Capacity of the dummy unit
Honeycomb	$31 \times 37 \times 2$ ($n_l \times n_w \times n_d$)	Meshing granularity
Instrumen	$21 \times 37 \times 5$ ($n_l \times n_w \times n_d$)	Meshing granularity
Interface heater	$21 \times 37 \times 1$ ($n_l \times n_w \times n_d$)	Meshing granularity
$\lambda_{\text{dummy unit}}$	167 W m^{-1} K^{-1}	Thermal conductivity of Aluminum 6061
$\lambda_{\text{honeycomb panel xy}}$	8 W m^{-1} K^{-1}	Average in-plane thermal conductivity
$\lambda_{\text{honeycomb panel z}}$	2 W m^{-1} K^{-1}	Average out-of-plane thermal conductivity
$CC_{\text{CP HCP}}$	20.8 W m^{-2} K^{-1}	Between the cold plate, the CFRP panel
$CC_{\text{HCP IFH}}$	500 W m^{-2} K^{-1}	Between CFRP panel, interface heater
$CC_{\text{IFH ID}}$	500 W m^{-2} K^{-1}	Between the interface heater, dummy unit
MLI efficiency	GR=0.013, GL=0.019	Mix of a conductive, radiative coupling factor

Bibliography

[1] Danzmann, K. & L3 proposal team. Laser interferometer space antenna. *arXiv:1702.00786 [astro-ph]* (2017).

[2] Ju, L., Blair, D. G. & Zhao, C. Detection of gravitational waves. *Reports on Progress in Physics* (2000). DOI 10.1088/0034-4885/63/9/201.

[3] Koehlenbeck, S. M. *et al.* A study on motion reduction for suspended platforms used in gravitational wave detectors. *Scientific Reports* (2023). DOI 10.1038/s41598-023-29418-x.

[4] Danzmann, K. & LISA study team. Pre-Phase A Report (1998).

[5] Johann, U. & LISA study team. LISA FTR report no. LI-RP-DS-009.

[6] Johann, U. A., Gath, P. F., Holota, W., Schulte, H. R. & Weise, D. Novel payload architectures for LISA (2006). DOI 10.1063/1.2405060.

[7] Johann, U., Braxmaier, C., Holota, W. & Jörck, H. Novel payload architectures for LISA. *International Conference on Space Optics — ICSO 2006* (2006). DOI 10.1117/12.2308123.

[8] Johann, U., Sell, A., Weise, D. & Ergenzinger, K. LISA instrument architecture option "In-Field Siderostat Pointing".Unsolicited proposal for a novel opto-mechnical lisa instrument architecture. (2023). DOI 10.13140/RG.2.2.10948.50568/1.

[9] Brugger, C. *et al.* An experiment to test in-field pointing for elisa. *International Conference on Space Optics 2014* (2017). DOI 10.1117/12.2304152.

[10] Weise, D. R. *et al.* Alternative opto-mechanical architectures for the LISA instrument. *Journal of Physics: Conference Series* (2009). DOI 10.1088/1742-6596/154/1/012029.

[11] Livas, J. *et al.* eLISA telescope in-field pointing and scattered light study. *Journal of Physics: Conference Series* (2017). DOI 10.1088/1742-6596/840/1/012015.

[12] Sanz, I. E., Heske, A. & Livas, J. C. A telescope for LISA – the laser interferometer space antenna. *Advanced Optical Technologies* (2018). DOI 10.1515/aot-2018-0044.

[13] TEB. LISA-Optical Assembly Tracking Mechanism Developement. *ESA-SCI-F-ESTEC-SOW-2019-028* (2021).

[14] Hasselmann, N. F. *et al.* End-to-end measurement of tilt-to-pathlength coupling effects for LISA. *International Conference on Space Optics — ICSO 2022* (2023). DOI 10.1117/12.2691446.

[15] Hasselmann, N. F. *et al.* LISA optical metrology: tilt-to-pathlength coupling effects on the picometer scale. *Conference Name: International Conference on Space Optics — ICSO 2020* (2021). DOI 10.1117/12.2599636.

[16] Pijnenburg, J. a. C. M. & Rijnveld, N. Picometer stable scan mechanism for gravitational wave detection in space: LISA PAAM. *International Conference on Space Optics — ICSO 2010* (2017). DOI 10.1117/12.2309235.

[17] Pei, X., Yu, J., Zong, G., Bi, S. & Su, H. The modeling of cartwheel flexural hinges. *Mechanism and Machine Theory* (2009). DOI 10.1016/j.mechmachtheory.2009.04.006.

[18] Weise, D. LISA-ASD-TN-3018 'Piston at Active Mirrors'.

[19] Chwalla, M. *et al.* Design and construction of an optical test bed for LISA imaging systems and tilt-to-length coupling. *Classical and Quantum Gravity* (2016). DOI 10.1088/0264-9381/33/24/245015.

[20] Chwalla, M. *et al.* Optical suppression of tilt-to-length coupling in the LISA long-arm interferometer. *Physical Review Applied* (2020). DOI 10.1103/PhysRevApplied.14.014030.

[21] Frosch, R. A. & Korsch, D. G. Anastigmatic three-mirror telescope; us4101195a (1978).

[22] Strojnik, M., Bravo-Medina, B., Beltran-Gonzalez, A. & Wang, Y. Off-axis three-mirror optical system designs: From cooke's triplet to remote sensing and surveying instruments. *Applied Sciences* (2023). DOI 10.3390/app13158866.

[23] Korsch, D. Design and optimization technique for three-mirror telescopes. *Applied Optics* (1980). DOI 10.1364/AO.19.003640.

[24] Sell, A. GWT-TN02-ADS-0.3.

[25] Weaver, A. J., Mueller, G. & Fulda, P. J. Wavefront error based tilt-to-length noise analysis for the LISA transmitted beam. *Classical and Quantum Gravity* (2022). DOI 10.1088/1361-6382/ac8a88.

[26] Dennis, W. LOB-TN-007-05-ASD.

[27] Boyadjian, J. GWT-TN05-0.2.

[28] Scipioni, M. Masters thesis: Orbital dynamics simulator for LISA: design and assembly.

[29] Wanner, G., Schuster, S., Tröbs, M. & Heinzel, G. A brief comparison of optical pathlength difference and various definitions for the interferometric phase. *Journal of Physics: Conference Series* (2015). DOI 10.1088/1742-6596/610/1/012043.

[30] IFP-PR-001v1.0 progress report.

[31] IFP-PR-002v1.0 progress report.

[32] IFP-PR-003v1.0 progress report.

[33] IFP-PR-005v1.0 progress report.

[34] IFP-PR-004v1.0 progress report.

[35] IFP-PR-006v1.0 progress report.

[36] IFP-PR-007v1.0 progress report.

[37] IFP-PR-016v1.0 progress report.

[38] IFP-PR-014v1.0 progress report.

[39] IFP-PR-013v1.0 progress report.

[40] IFP-PR-012v1.0 progress report.

[41] IFP-PR-010v1.0 progress report.

[42] IFP-PR-011v1.0 progress report.

[43] IFP-PR-009v1.0 progress report.

[44] IFP-PR-015v1.0 progress report.

[45] IFP-PR-008v1.0 progress report.

[46] IFP-PR-017v1.0 progress report.

[47] IFP-PR-018v1.0 final report.

[48] Wu, C.-m., Lawall, J. & Deslattes, R. D. Heterodyne interferometer with subatomic periodic nonlinearity. *Applied Optics* (1999). DOI 10.1364/AO.38.004089.

[49] Schultze, A., Weise, D., Sell, A. & Braxmaier, C. Optical pilot-tone correction of phase errors in photo-detection chains (2023). DOI arXiv:2306.15738.

[50] Veggel, A.-M. A. v. & Killow, C. J. Hydroxide catalysis bonding for astronomical instruments. *Advanced Optical Technologies* **3** (2014). DOI 10.1515/aot-2014-0022.

[51] Geradi, D. & Sell, A. GWT-TN01-ADS-0.3.

[52] Sell, A. GWT-TN04-ADS-0.2.

[53] Brugger, C. PhD thesis: Hochgenaue optische Strahlkontolle für den weltraum-gestuetzten Einsatz in Gravitationswellen Detektoren.

[54] Sasso, C. P., Mana, G. & Mottini, S. Telescope jitters and phase noise in the LISA interferometer. *Optics Express* (2019). DOI 10.1364/OE.27.016855.

[55] Zhou, Z., Yi, Y., Wu, S. & Luo, J. Low-frequency seismic spectrum measured by a laser interferometer combined with a low-frequency folded pendulum. *Meas. Sci. Technol* (2004).

[56] Hechenblaikner, G. Common mode noise rejection properties of amplitude and phase noise in a heterodyne interferometer. *JOSA A* (2013). DOI 10.1364/JOSAA.30.000941.

[57] Wissel, L. *et al.* Relative-intensity-noise coupling in heterodyne interferometers. *Physical Review Applied* (2022). DOI 10.1103/PhysRevApplied.17.024025.

[58] Schuldt, T. *et al.* A high-performance iodine-based frequency reference for space applications (2017).

[59] Sanjuan, J. *et al.* Simultaneous laser frequency stabilization to an optical cavity and an iodine frequency reference. *Optics Letters* (2021). DOI 10.1364/OL.413419.

[60] Hasselmann, N. F., Nicloux, M. & Sell, A. Elimination of periodic nonlinearities of actuators with internal periodic processes. *arxiv* (2022). DOI 10.48550/arXiv.2211.04137.

[61] Mohith, S., Upadhya, A. R., Navin, K. P., Kulkarni, S. M. & Rao, M. Recent trends in piezoelectric actuators for precision motion and their applications: a review. *Smart Materials and Structures* **30**, 013002 (2020). DOI 10.1088/1361-665X/abc6b9.

[62] den Heijer, M., Fokkema, V., Saedi, A., Schakel, P. & Rost, M. J. Improving the accuracy of walking piezo motors. *Review of Scientific Instruments* **85**, 055007 (2014). DOI 10.1063/1.4878624.

[63] Silvestri, M., Confalonieri, M. & Ferrario, A. Piezoelectric actuators for micro positioning stages in automated machines: experimental characterization of open loop implementations. *FME Transaction* **45**, 331–338 (2017). DOI 10.5937/fmet1703331S.

[64] Uzunovic, T., Golubovic, E. & Sabanovic, A. Piezo LEGS driving principle based on coordinate transformation. *IEEE/ASME Transactions on Mechatronics* **20**, 1395–1405 (2015). DOI 10.1109/TMECH.2014.2351272.

[65] Merry, R., van de Molengraft, R. & Steinbuch, M. Modeling of a walking piezo actuator. *Sensors and Actuators A: Physical* **162**, 51–60 (2010). DOI 10.1016/j.sna.2010.05.033.

[66] Merry, R. J. E., de Kleijn, N. C. T., van de Molengraft, M. J. G. & Steinbuch, M. Using a walking piezo actuator to drive and control a high-precision stage. *IEEE/ASME Transactions on Mechatronics* **14**, 21–31 (2009). DOI 10.1109/TMECH.2008.2006756.

[67] Szufnarowski, F. & Schneider, A. Two-dimensional dynamics of a quasi-static legged piezoelectric actuator. *Smart Materials and Structures* **21**, 055007 (2012). DOI 10.1088/0964-1726/21/5/055007.

[68] Witvoet, G. & Human, J. Realization and performance validation of the in-field pointing mechanism for the evolved laser interferometer space antenna. *ESA SP., 737.10* (2015).

[69] Li, P.-Z., Wang, X.-D., Zhao, L., Zhang, D.-F. & Guo, K. Dynamic linear modeling, identification and precise control of a walking piezo-actuated stage. *Mechanical Systems and Signal Processing* **128**, 141–152 (2019). DOI 10.1016/j.ymssp.2019.03.037.

[70] Merry, R. J. E., Maassen, M. G. J. M., van de Molengraft, M. J. G., van de Wouw, N. & Steinbuch, M. Modeling and waveform optimization of a nano-motion piezo stage. *IEEE/ASME Transactions on Mechatronics* **16**, 615–626 (2011). DOI 10.1109/TMECH.2010.2050209.

[71] Johansson, S., Bexell, M. & Jansson, A. Fine control of electromechanical motors; us6798117b2 (2004).

[72] Schuldt, T. *et al.* Development of a compact optical absolute frequency reference for space with 10-15 instability. *Applied Optics* (2017). DOI 10.1364/AO.56.001101.

[73] Witvoet, G. Realization and performance validation of the in-field pointing mechanism for the evolved laser interferometer space antenna. *16th European Space Mechanisms and Tribology Symposium 2015* (2015).

[74] Donnet, C. *et al.* Diamond-like, carbon coatings for vacuum and space tribology. *European Space Agency, (Special Publication) ESA SP* (1997).

[75] Vanhulsel, A. *et al.* Development of highly hydrogenated DLC coatings for solid lubricant applications in space. *Conference Name: 11th European Space Mechanisms and Tribology Symposium, ESMATS* (2005).

[76] Lugo, D. C. *et al.* Characterization and tribologic study in high vacuum of hydrogenated DLC films deposited using pulsed DC PECVD system for space applications. *Surface and Coatings Technology* (2017). DOI 10.1016/j.surfcoat.2017.07.084.

[77] Wu, J., Cai, S., Cui, J. & Tan, J. A generalized analytical compliance model for cartwheel flexure hinges. *Review of Scientific Instruments* (2015). DOI 10.1063/1.4934199.

[78] Kang, D. & Gweon, D. Analysis and design of a cartwheel-type flexure hinge. *Precision Engineering* (2013). DOI 10.1016/j.precisioneng.2012.06.005.

[79] Karmiris-Obratański, P., Papazoglou, E. L., Leszczyńska-Madej, B., Zagórski, K. & Markopoulos, A. P. A comprehensive study on processing ti–6al–4v ELI with high power EDM. *Materials* (2021). DOI 10.3390/ma14020303.

[80] Papazoglou, E. L., Karmiris-Obratański, P., Leszczyńska-Madej, B. & Markopoulos, A. P. A study on electrical discharge machining of titanium grade2 with experimental and theoretical analysis. *Scientific Reports* (2021). DOI 10.1038/s41598-021-88534-8.

[81] Gerberding, O., Isleif, K.-S., Mehmet, M., Danzmann, K. & Heinzel, G. Laser-frequency stabilization via a quasimonolithic mach-zehnder interferometer with arms of unequal length and balanced dc readout. *Physical Review Applied* (2017). DOI 10.1103/PhysRevApplied.7.024027.

[82] Fleddermann, R. *et al.* Sub-pm per square root hertz non-reciprocal noise in the LISA backlink fiber. *Classical and Quantum Gravity* **35** (2018). DOI 10.1088/1361-6382/aaa276.

[83] Wand, V. *et al.* Noise sources in the LTP heterodyne interferometer. *Classical and Quantum Gravity* (2006). DOI 10.1088/0264-9381/23/8/S21.

CV and list of publications

N. F. Hasselmann

Physicist,
Specialized in photonics

Apostelholzweg 3, 82205 Gilching, Germany

nilsfrederik.hasselmann@gmail.com

+49 1512 9069504

Dec 27, 1993

Nationality

German

Languages

- German ●●●●●
- English ●●●●○
- French ●○○○○

Hard Skills

- Optical engineering
- Data analysis
- MATLAB, Comsol, LabView, Optometrica
- Photonics, particle physics

Soft Skills

- Integrity ●●●●●
  - Responsibility
  - Honesty
- Endurance ●●●●●
- Patience ●●●●○
- Highly motivated ●●●●●
  - Dedicated
- Communicative ●●●●○
  - Open and encouraging
  - Teamwork

Working Experience

2023-today **Optical engineer / Systems engineer** OHB SE
Working on several pre-developments within the AE-2 context, on the validation of the LISA BAM and on COMPACT

2019-2023 **Ph.D. student in Physics** AIRBUS DS/AEI
Validation of the In-Field Pointing (IFP) scheme for the LISA mission, co-design and experimental validation of the Siderostat Pointing Mechanism (SPM), co-invention and design of a fully retractable launch lock prototype for LISA, active thermal control down to single $\mu K/\sqrt{Hz}$ and much more.

2018-2019 **Cells in Motion Cluster of Excellence Pilot Project 18/8** ICDI/WWU
Analysis of cell stress in laser-based biofabricated hydrogel microenvironments.

2017 **Student Assistant** NLOL/WWU Münster
Investigation of the feasibility of the in-situ patterning of hydrogels for cell-based sensing schemes and development of novel fabrication techniques for microbiorobotics.

Education

2019 – today **Ph.D. student in Physics at Max Planck (AEI, Leibniz Universität Hannover) and Airbus** AEI/Airbus
see above, section Working experience; Scientific supervision by Prof. Heinzel (AEI) and Dr. Sell (Airbus); position funded in part by the DLR (50 percent)

2016 – 2019 **M.Sc. Physics (final grade** 1.1**)** WWU Münster
Spezializations: Photonics and particle physics. The focus of the thesis: Patterning of light-guiding protogel structures for in-situ guidance of light to the biological specimen and investigating a novel imaging modality for investigating cell polarity.

Master's thesis (1.1**)** Institute of Applied Physics
Two-photon fabrication of protein-based waveguides
Supervision: Prof. Dr. Cornelia Denz, Dr. Jörg Imbrock

2013 – 2016 **B.Sc. Physics (**2.0**)** WWU Münster
Focus of thesis: Nanofabrication of structures serving as waveguides by two-photon patterning of a synthetic hydrogel.

Bachelor's thesis (1.3**)** Institute of Applied Physics
Fabrication of hydrogel waveguides by means of two-photon polymerization.
Supervision: Dr. Wolfgang Horn, Dr. Jörg Imbrock

Publications

2025 **Minimization of flicker noise in resistive temperature measurements at low frequencies** (Hasselmann et al.)

In preparation

2025 **In-Field-Pointing: Validation of an advanced pointing concept beyond LISA** (Hasselmann et al.)

In preparation

2025 **A retractable launch lock performing a linear motion only** (Hasselmann et al.)

In preparation

2025 **Active thermal control for ultra-stable satellite instrument boxes** (Hailer et al.)

In preparation

2025 **Active compensation of linear TTL in precision interferometry for LISA** (Hasselmann et al.)

In preparation

2024 **Siderostat-Pointing: Validation of an advanced pointing concept beyond LISA** (Hasselmann et al.)

In preparation

2024 **Elimination of periodic nonlinearities of actuators with internal periodic processes** (Hasselmann et al.)

Under review

2023 **Patent application for a retractable launch lock that performs a linear motion only** (A. Sell, F. Hasselmann, T. Ziegler)

Patent pending, P900 238-EP-EPA

2022 **End-to-end measurement of tilt-to-pathlength coupling effects for LISA** (Hasselmann et al.)

Proc. ICSO2022 https://doi.org/10.1117/12.2691446

2020 **LISA optical metrology: Tilt-to-pathlength coupling effects on the picometer scale** (Hasselmann et al.)

Proc. SPIE11852

2018 **Attachment of microstructures to single bacteria by two-photon patterning of a protein-based hydrogel** (Hasselmann and Horn)

Biomedical Physics & Engineering Express

2017 **Two-photon fabrication of hydrogel microstructures for excitation and immobilization of cells** (Hasselmann et al.)

Biomedical Microdevices